ABSTRACT

Title of Document: MODIFICATION OF MIXED PROTON-ELECTRON CONDUCTORS FOR HYDROGEN TRANSPORT MEMBRANES AND INVESTIGATION OF AMMONIA ION TRANSFER MEMBRANES

Xuan Liang, Master of Science, 2015

Directed By: Professor, Dr.Eric Wachsman
Director of UMERC, the Wachsman Group and
William L. Crentz Centennial Chair in Energy
Research

$SrCe_{0.9}Eu_{0.1}O_{3-\delta}$ has low electron conductivity that limiting the hydrogen permeation. Effects of different dopants in $SrCeO_3$ were studied in order to find new materials that have higher electron conductivity. Total conductivities of these materials and transference number of each species were used for calculating the electron and proton conductivities in the mixed ionic electronic conductors. $SrCe_{0.9}Pr_{0.1}O_{3-\delta}$ was claimed to have higher electron conductivity than $SrCe_{0.9}Eu_{0.1}O_{3-\delta}$. The hydrogen permeability of $SrCe_{1-x}Pr_xO_{3-\delta}$ was studied as a function of temperature, hydrogen partial pressure gradient and water vapor pressure gradient. Modified Nafion® membranes can be used for electrochemical ammonia compression.

MODIFICATION OF MIXED PROTON-ELECTRON CONDUCTORS FOR HYDROGEN TRANSPORT MEMBRANES AND INVESTIGATION OF AMMONIA ION TRANSFER MEMBRANES

By

Xuan Liang

Thesis submitted to the Faculty of the Graduate School of the
University of Maryland, College Park, in partial fulfillment
of the requirements for the degree of
Master of Science
2015

Advisory Committee:
Professor Eric Wachsman, Chair
Professor Chunsheng Wang
Professor Dongxia Liu

Dedication

This work is dedicated to my parents, Mann Sakbodin and Keji Pan, who have supported and encouraged me during my graduate study. Without them I cannot finish this Master's degree. This work is also dedicated to professor Chunsheng Wang, for introducing me into electrochemistry research.

Acknowledgements

I want to give my thanks to my advisor, Professor Eric Wachsman, for his guidance and instructions during my graduate study and research in his group. He helped me with my research project and writing this thesis. I also thank him for taking me as a PhD student, which gave me the chance to pursue a higher education. I also want to thank my former advisor Dr. Chunsheng Wang, for his wise advice and encouragement.

Thank you Dr. Eric Wachsman, Dr. Chunsheng Wang, and Dr. Dongxia Liu for agreeing to serve on my committee.

Office of Naval Research (ONR) financially supported this work.

Table of Contents

Dedication ii

Acknowledgements iii

Table of Contents iv

List of Tables vi

List of Figures vii

Chapter 1: Introduction 1

1.1 Mixed Ionic Electronic Conductor 1

1.2 Rationale of Proton Transfer Membrane 2

1.3 Hydrogen permeability 4

1.4 Membrane reactor 5

1.5 Existing Challenge in Proton Transfer Membrane Reactors 6

Chapter 2: New Materials Exploration 8

2.1 Introduction 8

2.2 Experiment 9

2.3 Results and Analysis 10

Chapter 3: Total Conductivity of the new materials 17

3.1 Introduction 17

3.2 EIS measurement 19

3.3 Results and Analysis 20

Chapter 4: Proton and Electron Conductivity of $SrCe_{1-x}Pr_xO_{3-\delta}$ (x=0.1, 0.15, 0.2) 42

4.1 OCV measurement 42

4.2 Results and Analysis 44

Chapter 5: Hydrogen Permeability of $SrCe_{1-x}Pr_xO_{3-\delta}$ (x=0.1, 0.2) 52

5.1 Hydrogen Permeation test 52

5.2 Results and Analysis 52

Chapter 6: Application of $SrCe_{0.9}Pr_{0.1}O_{3-\delta}$ in Tubular Membrane Reactors 60

6.1 Introduction 60

6.2 Fabrication of Membrane reactor 61

6.3 Results and Analysis 64

Chapter 7: Modified Nafion® Membrane used in Electrochemical Ammonia Compression and Separation 78

7.1 Introductions and Background 78

7.2 Experiment 81

7.3 Results and Data Analysis 83

4.4 Conclusion 88

Chapter 8: Conclusions and Future Work 90

8.1 Conclusions 90

References 92

List of Tables

Table 4-1 OCV and electron transference number under different chemical potential gradient and temperature
Table 5-1 Calculated hydrogen permeation flux under [100% H_2, Pt/membrane/Pt, 5%H_2] between 600°C and 800°C (L=1.2mm thick).
Table 6-1 Hydrogen permeation of the ESC membrane reactor
Table 6-2 Calculated hydrogen permeation flux under [100% H_2, Pt/membrane/Pt, 5%H_2] between 600°C and 800°C (L=30μm thick).

List of Figures

Figure 1-1. Two point defects in ceramic materials (a) Frenkel disorder and (b) Schottky disorder
Figure 1-2. Hydrogen flux as a function of applied hydrogen chemical potential gradients under various conditions of P_{H2O} at 850°C
Figure 2-1 XRD pattern of SCY power calcined at 1150°C
Figure 2-2 XRD pattern analyzed of $SrCe_{0.8}Y_{0.1}Nb_{0.1}O_{3-\delta}$ power
Figure 2-3 XRD pattern analyzed of $SrCe_{0.85}Y_{0.1}Nb_{0.05}O_{3-\delta}$ powder
Figure 2-4 XRD pattern analyzed of $SrCe_{0.8}Ti_{0.1}Y_{0.1}O_{3-\delta}$ powder
Figure 2-5 XRD pattern analyzed of $SrCeO_3$ doped with 5%, 8% and 10% Ti
Figure 2-6 XRD pattern analyzed of $SrCeO_3$ doped with 20% and 30% Ti
Figure 2-7 XRD pattern analyzed of $SrCeO_3$ doped with 5%, 8% and 10% Cr
Figure 2-8 Peak shift and split of different doping amount
Figure 2-9 XRD pattern analyzed of $SrCeO_3$ doped with 5%, 8% and 10% Pr
Figure 2-10 Peak shift and intensity change of different doping amount
Figure 3-1 Total conductivity of different Eu-doped $SrCe_{1-x}Eu_xO_{3-\delta}$ between 600 °C and 900 °C under dry hydrogen atmosphere
Figure 3-2 Schematic of the apparatus for conductivity measurement.
Figure 3-3 Nyquist plot of $SrCeO_3$ measured in 90sccm N_2; 10sccm H_2; 3% H_2O
Figure 3-4 Nyquist plot of $SrCe_{0.9}Y_{0.1}O_{3-\delta}$ measured in 90sccm N_2; 10sccm H_2; 3% H_2O
Figure 3-5 Nyquist plot of $SrCe_{0.85}Y_{0.1}Nb_{0.05}O_{3-\delta}$ measured in 90sccm N_2; 10sccm H_2 ; 3% H_2O
Figure 3-6 Nyquist plot of $SrCe_{0.92}Ti_{0.08}O_{3-\delta}$ measured in dry air
Figure 3-7 Nyquist plot of $SrCe_{0.92}Ti_{0.08}O_{3-\delta}$ measured in air (with 3%H_2O)
Figure 3-8 Nyquist plot of $SrCe_{0.92}Ti_{0.08}O_{3-\delta}$ measured in dry N_2
Figure 3-9 Nyquist plot of $SrCe_{0.92}Ti_{0.08}O_{3-\delta}$ measured in N_2 (with 3%H_2O)
Figure 3-10 Nyquist plot of $SrCe_{0.92}Ti_{0.08}O_{3-\delta}$ measured in 90sccm N_2; 10sccm H_2
Figure 3-11 Nyquist plot of $SrCe_{0.92}Ti_{0.08}O_{3-\delta}$ measured in 90sccm N_2; 10sccm H_2; 3%H_2O
Figure 3-12 Nyquist plot of $SrCe_{0.95}Ti_{0.05}O_{3-\delta}$ measured in 90sccm N_2; 10sccm H_2; 3%H_2O
Figure 3-13 Nyquist plot of $SrCe_{0.9}Ti_{0.1}O_{3-\delta}$ measured in 90sccm N_2; 10sccm H_2; 3%H_2O
Figure 3-14 Nyquist plot of $SrCe_{0.95}Cr_{0.05}O_{3-\delta}$ measured in 90sccm N_2; 10sccm H_2; 3%H_2O
Figure 3-15 Nyquist plot of $SrCe_{0.9}Cr_{0.1}O_{3-\delta}$ measured in 90sccm N_2; 10sccm H_2; 3%H_2O
Figure 3-16 Nyquist plot of $SrCe_{0.92}Cr_{0.08}O_{3-\delta}$ measured in dry air
Figure 3-17 Nyquist plot of $SrCe_{0.92}Cr_{0.08}O_{3-\delta}$ measured in air (with 3%H_2O)
Figure 3-18 Nyquist plot of $SrCe_{0.92}Cr_{0.08}O_{3-\delta}$ measured in dry N_2
Figure 3-19 Nyquist plot of $SrCe_{0.92}Cr_{0.08}O_{3-\delta}$ measured in N_2 (with 3%H_2O)
Figure 3-20 Nyquist plot of $SrCe_{0.92}Cr_{0.08}O_{3-\delta}$ measured in 90sccm N_2; 10sccm H_2

Figure 3-21 Nyquist plot of $SrCe_{0.92}Cr_{0.08}O_{3-\delta}$ measured in 90sccm N_2; 10sccm H_2; 3%H_2O
Figure 3-22 Nyquist plot of $SrCe_{0.92}Pr_{0.08}O_{3-\delta}$ measured in dry air
Figure 3-23 Nyquist plot of $SrCe_{0.92}Pr_{0.08}O_{3-\delta}$ measured in air (with 3%H_2O)
Figure 3-24 Nyquist plot of $SrCe_{0.92}Pr_{0.08}O_{3-\delta}$ measured in dry N_2
Figure 3-25 Nyquist plot of $SrCe_{0.92}Pr_{0.08}O_{3-\delta}$ measured in N_2 (with 3%H_2O)
Figure 3-26 Nyquist plot of $SrCe_{0.92}Pr_{0.08}O_{3-\delta}$ measured in 90sccm N_2; 10sccm H_2
Figure 3-27 Nyquist plot of $SrCe_{0.92}Pr_{0.08}O_{3-\delta}$ measured in 90sccm N_2; 10sccm H_2; 3%H_2O
Figure 3-28 Nyquist plot of $SrCe_{0.9}Pr_{0.1}O_{3-\delta}$ measured in 90sccm N_2; 10sccm H_2; 3%H_2O
Figure 3-29 Nyquist plot of $SrCe_{0.85}Pr_{0.15}O_{3-\delta}$ measured in 90sccm N_2; 10sccm H_2; 3%H_2O
Figure 3-30 Nyquist plot of $SrCe_{0.8}Pr_{0.2}O_{3-\delta}$ measured in 90sccm N_2; 10sccm H_2; 3%H_2O
Figure 3-31 Total conductivities of $SrCeO_3$, $SrCe_{0.9}Y_{0.1}O_{3-\delta}$ and $SrCe_{0.85}Y_{0.1}Nb_{0.05}O_{3-\delta}$ dependent of temperature
Figure 3-32 Total conductivity of $SrCe_{1-x}Ti_xO_{3-\delta}$ (x=0.05;0.08;0.1.) depend on Temperature tested in 90 sccm N_2 ; 10sccm H_2 with 3% H_2O
Figure 3-33 Total conductivity of $SrCe_{1-x}Ti_xO_{3-\delta}$ (x=0.05;0.08;0.1.) depend on doping amount tested in 90 sccm N_2 ; 10sccm H_2 with 3% H_2O
Figure 3-34 Total conductivity of $SrCe_{0.92}Ti_{0.08}O_{3-\delta}$ depend on Temperature tested in various gas environment (Test condition: 90 sccm N_2 ; 10 sccm H_2 ; 3% H_2O)
Figure 3-35 Total conductivity of $SrCe_{0.92}Ti_{0.08}O_{3-\delta}$ depend on Temperature tested in dry air and air with 3% H_2O
Figure 3-36 Total conductivity of $SrCe_{1-x}Cr_xO_{3-\delta}$ (x=0.05;0.08;0.1.) depend on Temperature tested in 90 sccm N_2 ; 10sccm H_2 with 3% H_2O
Figure 3-37 Total conductivity of $SrCe_{0.92}Cr_{0.08}O_{3-\delta}$ depend on Temperature tested in various gas environment
Figure 3-38 Total conductivity of $SrCe_{1-x}Pr_xO_{3-\delta}$ (x=0.08; 0.1; 0.2) depend on Temperature tested in 90 sccm N_2; 10sccm H_2 with 3% H_2O
Figure 3-39 Total conductivity of $SrCe_{1-x}Pr_xO_{3-\delta}$ (x=0.08; 0.1; 0.2) depend on different doping amount
Figure 3-40 Total conductivity of $SrCe_{0.92}Pr_{0.08}O_{3-\delta}$ depend on Temperature tested in various gas environment
Figure 3-41 Total conductivity of $SrCe_{0.8}Pr_{0.2}O_{3-\delta}$ depend on Temperature tested in various gas environment
Figure 3-42 Total conductivity of different dopant tested in 90 sccm N_2 ; 10sccm H_2 with 3% H_2O
Figure 3-43 Conductivity comparison of all the materials synthesized tested in 90 sccm N_2 ; 10sccm H_2 with 3% H_2O
Figure 4-1 The schematic illustration of experimental setup for transference number measurement and permeation test
Figure 4-2 Transfer number of each species in 10 mol%, 15 mol % and 20 mol% Pr doped material tested under 100% H_2 to 5% H_2 with 95% balance air

Figure 4-3 Electron transfer number of 10 mol%, 15 mol % and 20 mol% Pr doped material depend on hydrogen concentration gradient
Figure 4-4 Proton and Electron conductivity of 10 mol%, 15 mol% and 20 mol% Pr doped material
Figure 4-5 Comparison of Proton conductivity behaviors of $SrCe_{1-x}Pr_xO_{3-\delta}$ (x=0.1, 0.15, 0.2) [solid line] and $SrCe_{1-x}Eu_xO_{3-\delta}$ (x=0.1, 0.15, 0.2) [dash line] for different temperature under hydrogen/water vapor (3% H_2O) atmosphere
Figure 4-6 Proton conductivity of different Pr-doped material between 600°C and 800°C under hydrogen atmosphere
Figure 4-7 Electron conductivity of different Pr-doped material between 600°C and 800°C under hydrogen atmosphere
Figure 4-8 Ambipolar conductivity of 10 mol%, 15 mol% and 20 mol% Pr doped material
Figure 5-1 Hydrogen flux as a function of temperature for 10 mol% Pr-doped $SrCeO_{3-\delta}$: closed symbols=100% H_2; dry and open symbols: P_{H2}=0.97atm, P_{H2O}=0.03atm.
Figure 5-2 Hydrogen Flux as a function of applied hydrogen chemical potential gradients at 850 °C
Figure 5-3 Hydrogen Flux of $SrCe_{0.9}Pr_{0.1}O_{3-\delta}$ as a function of temperature under dry condition
Figure 5-4 Hydrogen Flux of $SrCe_{0.9}Pr_{0.1}O_{3-\delta}$ as a function of temperature under P_{H2O}=0.03 atm
Figure 5-5 Hydrogen flux as a function of temperature for 20 mol% Pr-doped $SrCeO_{3-\delta}$: closed symbols=100% H_2; dry and open symbols: P_{H2}=0.97atm, P_{H2O}=0.03atm
Figure 5-6 Hydrogen Flux as a function of applied hydrogen chemical potential gradients at 850 °C
Figure 5-7 Comparison of $SrCe_{0.9}Pr_{0.1}O_{3-\delta}$ and $SrCe_{0.8}Pr_{0.2}O_{3-\delta}$ hydrogen permeation
Figure 5-8 Permeated hydrogen flux of $SrCe_{0.9}Pr_{0.1}O_{3-\delta}$ and $SrCe_{0.8}Pr_{0.2}O_{3-\delta}$ membrane (1.2mm) based on calculation using Wagner equation (dash line) and experiment under pure hydrogen atmosphere on the feed side (solid line)
Figure 6-1 The schematic of the advanced membrane reactor used in effluent gas separation
Figure 6-2 XRD results of solid-state synthesized $SrCeO_3$ and sol-gel method synthesized $SrCe_{0.9}Eu_{0.1}O_{3-\delta}$
Figure 6-3 $SrCe_{0.9}Eu_{0.1}O_{3-\delta}$ Synthesized through different steps
Figure 6-4 The SEM result of the cross-section that showing the membrane thickness
Figure 6-5 The cross-section of the tube sintered at 1350 °C 4hrs with 5-times colloidal coating
Figure 6-6 The surface image of the tube sintered at 1350 °C 4hrs with 5-times colloidal coating
Figure 6-7 Dense membrane and thickness of the tube sintered at 1350 °C for 4hrs with 10-times colloidal coating

Figure 6-8 Surface image of dense membrane sintered at 1350 °C for 4hrs with 10-times colloidal coating
Figure 6-9 Hydrogen Permeation test of tube sintered at 1350 °C 4hrs with 5-times colloidal coating
Figure 6-10 Hydrogen Permeation test of tube sintered at 1350 °C 4hrs with 10-times colloidal coating
Figure 6-11 Hydrogen flux permeated at various hydrogen concentration from 700°C to 900°C
Figure 6-12 XRD pattern of $SrCe_{0.9}Pr_{0.1}O_{3-\delta}$ after Calcination 1100 °C 4hrs
Figure 6-13 Dense membrane and thickness of the tube sintered at 1450 °C for 4hrs with 3-times colloidal coating
Figure 6-14 Surface image of the membrane sintered at 1450 °C for 4hrs with 3-times colloidal coating
Figure 6-15 Hydrogen Permeation test of tube sintered at 1400 °C 4hrs with 10-times colloidal coating
Figure 6-16 Hydrogen Permeation test of tube sintered at 1350 °C 4hrs with 10-times colloidal coating
Figure 6-17 Theoretical Permeated Hydrogen Flux through 30μm membrane at case 1 calculated by Wagner Equation
Figure 7-1. Principle of the electrochemical hydrogen compressor
Figure 7-2. Scheme of Membrane Electrolyte Assembly (MEA) [14] and the Commercial Nafion® Membrane Structure
Figure 7-3. The schematic of the testing system.
Figure 7-4. The conductivity of modified membrane under different temperature.
Figure 7-5. Polarization curve of the compressor (25 °C, flow rate ratio NH_3:H_2 4:3, 0.05 mg/cm^2 Pt loading of Anode, 0.1 mg/cm^2 Pt loading of Cathode, Modified Nafion® 115).
Figure 7-6. The Concentration of ammonia under different potential (25 °C, flow rate ratio NH_3:H_2 4:3, 0.05 mg/cm^2 Pt loading of Anode, 0.1 mg/cm^2 Pt loading of Cathode, Modified Nafion® 115).
Figure 7-7. The polarization curve of the compressor under pure H_2 (3psi Flow rate 0.21L/min, GDE: Fuel Cells Etc® PtC 40% 0.3 mg/cm^2, 2.5cmx2.5cm Modified Nafion® 115, 28°C)
Figure 7-8. The polarization curve at NH_3: H_2 = 1:1 (3psi Flow rate 0.21L/min, 28 °C, GDE: Fuel Cells Etc® PtC 40% 0.3 mg/cm^2, 2.5cmx2.5cm Modified Nafion® 115, 28°C)
Figure 7-9. The Concentration change with Voltage (The arrow shows the direction of the cycle, H_2: NH_3=1:1.)
Figure 7-10. The polarization curve of the compressor with wet H_2 (3% H_2O, 3psi Flow rate 0.21L/min, NH_3: H_2 = 1:1,GDE: Fuel Cells Etc® PtC 40% 0.3 mg/cm^2, 2.5cmx2.5cm Modified Nafion® 115, 28°C)
Figure 7-11. The concentration of ammonia at cathode when supplying wet H_2 (3% H_2O, 3psi Flow rate 0.21L/min, NH_3: H_2 = 1:1,GDE: Fuel Cells Etc® PtC 40% 0.3 mg/cm^2, 2.5cmx2.5cm Modified Nafion® 115, 28°C)

Chapter 1: Introduction

Mixed proton-electron conductors were used as hydrogen transport membranes in the tubular membrane reactors. The membrane reactors can be used for separating the hydrogen from gas mixtures. The permeated hydrogen fluxes through the membrane material were limited by the low electron conductivity. In order to improve the transfer efficiency, new materials that may have both high proton and electron conductivities were explored.

1.1 Mixed Ionic Electronic Conductor

The mixed ionic and electronic conductors (MIEC) have attracted the attention for the reason that it is can be applied as hydrogen and humidity sensors, hydrogen separation in petrochemical processes and electrodes in SOFC [1-6]. MIEC can be used as cathode and anode material in SOFC. Shao and Haile[7,8] claimed that Perovskite oxide $Ba_{0.5}Sr_{0.5}Co_{0.8}Fe_{0.2}O_{3-\delta}$ (BSCF) can be used as cathode material. MIEC can also be used for hydrogen sensors, in petrochemical processes and as separation membranes. Iwahara [5] used proton-conducting ceramics for galvanic cell type hydrogen sensors. Schutter [6] applied strontium cerates to detecting hydrogen in coal gasification process.

$SrCeO_3$ and $BaCeO_3$ ceramics are typical perovskite-structure MIEC materials used for proton exchange membranes. They have the ability of conducting proton at high temperature with the water vapor existing [9-11]. The stability of these perovskite materials can be reflected by the tolerance factor. Goldschmit [12] stated that tolerance

factor (t) as shown in Equation 1-1. Tolerance factor ranges from 0.8 to 1. Orthoromic and cubic structure can be theoretically calculated.

$$t = \frac{R_A + R_O}{\sqrt{2}(R_B + R_O)} \quad (1\text{-}1)$$

Where R_A is the average radius of A cation, and R_B is the average radius of B cation, R_O is the average of anion (usually oxygen).

This research was based on $SrCeO_3$ doping different elements because $SrCeO_3$ has lower oxide-ion conductivity especially at high temperature. Meanwhile, strontium-cerate based perovskite oxides exhibit high proton conductivity [13,14].

1.2 Rationale of Proton Transfer Membrane

Defect is inevitable in ceramic materials. The imperfection can cause entropy increase and meanwhile reduce Gibbs free energy.

$$\Delta G = \Delta H - T\Delta S \quad (1\text{-}2)$$

Defects can be classified into electronic defects and structural defects. There are three kinds of structural defects depend on the defect location and area: point defects, line defects and plane defects. Point defects caused by ions moving from its original location to interstitial atoms are defined as Frenkel disorder. Schottky disorder is point defects caused by cation and anion missing at equal amount (Figure 1-1).

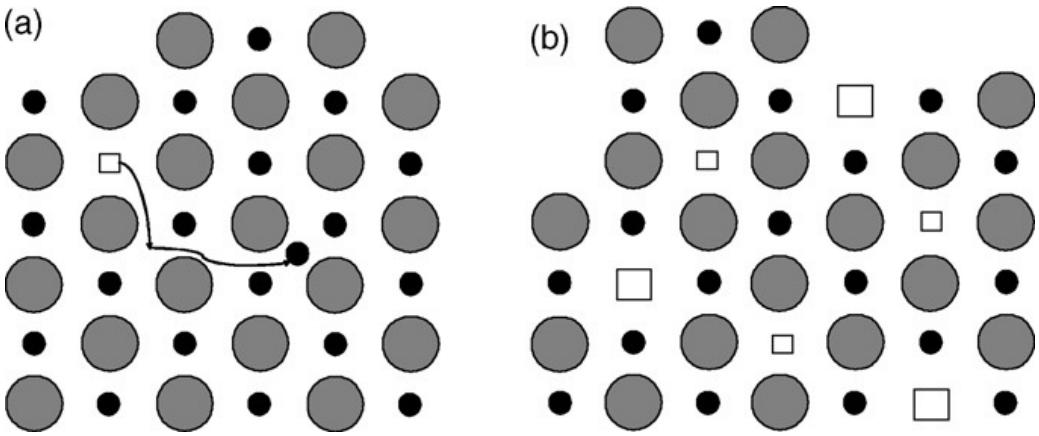

Figure 1-1. Two point defects in ceramic materials (a) Frenkel disorder and (b) Schottky disorder [15].

Oxygen vacancies in $SrCeO_3$ are Schottky disorder. Hydroxyl groups can fit in the oxygen vacancies when water vapor exists. The reaction can be written in Kroger-Vink notation:

$$H_2O + O_O^{\times} + V_O^{\cdot\cdot} \rightarrow 2OH_O^{\cdot} \qquad (1\text{-}3)$$

The hopping of the hydroxyl groups causes the proton conduction. Ce^{3+} introduces more oxygen vacancies after reduced at hydrogen atmosphere. It was reported [16] that Eu-doped materials increased hydrogen and electron conductivities because it introduced more oxygen vacancies and could release movable electrons ($Eu^{2+} \rightarrow Eu^{3+} + e^-$). Therefore, $SrCe_{1-x}Eu_xO_{3-\delta}$ is widely used material [17,18] for separation membranes in membrane reactors. However, the electron conductivity was much lower than proton conductivity for this material. The hydrogen permeation fluxes were limited by low electron conductivity [19]. Therefore, new materials that have higher electron conductivity were investigated for the hydrogen separation membrane reactors

1.3 Hydrogen permeability

Previous research [20,21] about Eu and Sm doped $SrCeO_3$ showed that these mixed protonic and electronic conducting materials can selectively permeate hydrogen. The hydrogen permeability is bulk limiting and determined by ambipolar conductivity. Permeation of hydrogen flux crossing bulk diffusion controlled materials can be calculated by Wagner equation [22]:

$$J_{OH_O^{\cdot}} = -\frac{1}{L}\left[\frac{RT}{4F^2}\int_{P'_{O2}}^{P''_{O2}} \sigma_t t_{OH_O^{\cdot}} t_{V_O^{\cdot\cdot}} dlnP_{O_2} + \frac{RT}{2F^2}\int_{P'_{H2}}^{P''_{H2}} \sigma_t t_{OH_O^{\cdot}} \times (t_{V_O^{\cdot\cdot}} + t_{e'}) dlnP_{H_2}\right] \quad (1\text{-}4)$$

Where σ_t is total conductivity, t_i is the transfer number of specific item i, F is Faraday constant and the partial pressure of gas is different of the two sides.

It was demonstrated that hydrogen permeation through 1.72 mm thickness membrane increase with temperature for both $SrCe_{0.95}Eu_{0.05}O_{3-\delta}$ and $SrCe_{0.95}Sm_{0.05}O_{3-\delta}$ materials. $SrCe_{1-x}Eu_xO_{3-\delta}$ has highest permeation at 850 °C under 100% hydrogen. The permeation will decrease when hydrogen going through bubbler. $SrCe_{0.95}Sm_{0.05}O_{3-\delta}$ has lower permeation compared to $SrCe_{0.95}Eu_{0.05}O_{3-\delta}$. The permeation of hydrogen highly depends on applied hydrogen chemical potential gradients under various conditions of partial pressure of vapor at 850°C (Figure 1-2).

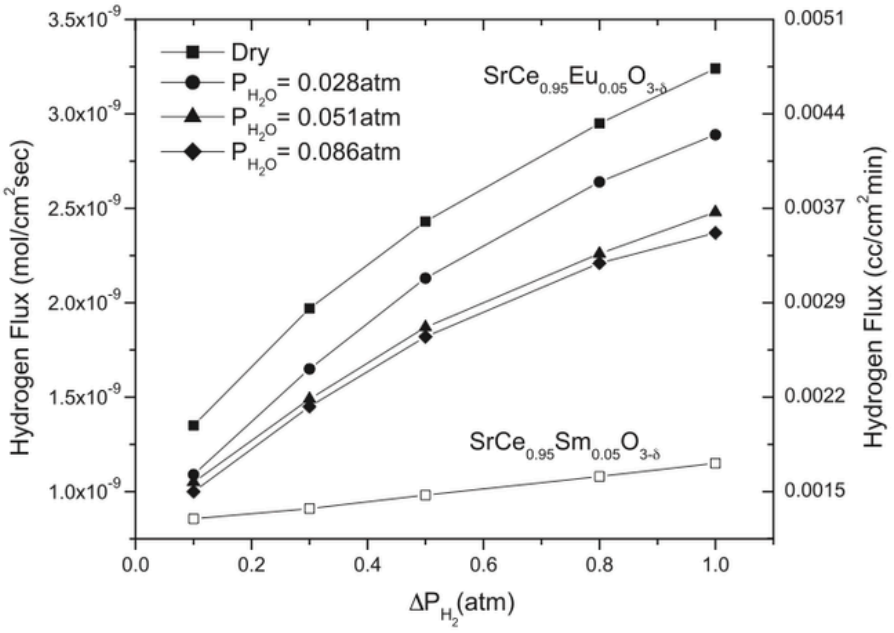

Figure 1-2 Hydrogen flux as a function of applied hydrogen chemical potential gradients under various conditions of P_{H2O} at 850°C [20]

1.4 Membrane reactor

Membrane reactors are functional permeation material supported by a porous material. Membrane reactors have larger permeation area than flat disk [23]. The thin-film membrane reactors can be used in steam reforming of methane [24], for hydrogenation and dehydrogenation of organic compounds [22]. Hamakawa [25,26] synthesize C_2 hydrocarbons by methane dimerization using $SrCe_{0.95}Yb_{0.05}O_{3-\alpha}$ ceramic membrane reactors.

$SrCe_{0.7}Zr_{0.2}Eu_{0.1}O_{3-\alpha}$ proton conducting membrane reactor was developed by Li [27] and used for carbon dioxide reforming of methane. $SrCe_{0.7}Zr_{0.2}Eu_{0.1}O_{3-\alpha}$ thin film dense membrane was coated on NiO- $SrCe_{0.8}Zr_{0.2}O_{3-\alpha}$ tubular support. This

membrane reactor can subtract hydrogen out of the products and shift the steam reforming of methane reaction and the carbon dioxide reforming of methane to the syngas side. It is approved that this membrane reactor can shift the equilibrium of the reaction yielding more hydrogen.

Hydrogen can be produced through Steam reforming of methane:

$$H_2O + CH_4 \leftrightarrow CO + 3H_2 \qquad \Delta H^0 = 206\ kJ/mol \tag{1-5}$$

Carbon dioxide reforming of methane can convert carbon dioxide to fuel that has great potential of recycling the waste gas to fuel.

$$CH_4 + CO_2 \leftrightarrow 2CO + 2H_2 \ \ \Delta H^0 = 247\ kJ/mol \tag{1-6}$$

Fischer-Tropsch (F-T) process (Equation 1-4) can further synthesize the syngas in to liquid fuels providing transportation fuels.

$$(2n+1)H_2 + nCO \rightarrow C_nH_{(2n+2)} + nH_2O \tag{1-7}$$

Fuel is generated from carbon dioxide that is harmful waste to environment. The recycle of carbon dioxide is an obvious great invention in energy development history. Membrane reactor can be used for these reactions with catalysts loading in the reactor. It is demonstrated that the selectivity of the reaction enhanced and the efficiency of the reaction is increased by using thin film membrane and large effective surface in the tubular membrane reactors.

1.5 Existing Challenge in Proton Transfer Membrane Reactors

Dense $SrCe_{0.9}Eu_{0.1}O_{3-\delta}$ thin film reactors have been investigated for its conductivity and hydrogen permeation flux under different temperature and gas environment. It was demonstrated by Open Circuit Voltage (OCV) measurement that the electron

conductivity is much more smaller than proton conductivity. The low electron conductivity highly limits the hydrogen permeation flux.

Chapter 2: New Materials Exploration

In order to enhance the electron conductivity, new materials of the membrane was investigated in this project. Based on radii, coordination number, ionization potential and their concentration in $Sr_{1-x'-x''}A'_{x'}A''_{x''}Ce_{1-y'-y''}B'_{y'}B''_{y''}O_{3-\delta}$, the role of dopants that increase hydrogen flux were explored. New materials with various doping element were synthesized through conventional ceramic process. Composition structure and phase purity were be determined by XRD.

2.1 Introduction

Strontium-cerate based perovskite oxides exhibit proton conductivity [28,29]. It was claimed that doping Yttrium could increase proton conductivity because the binding energy of Y^{3+} and hydroxyl group is the lowest and the distance between them are largest [30]. However, Yttrium-doped $SrCeO_3$ has relatively low electron conductivity. Titanium and Niobium were doped in $SrCe_{0.9}Y_{0.1}O_{3-\delta}$ in order to increase electron conductivity.

As double dopant at B site is relatively complicated, single dopants and their concentration in the material were studied. Several doping elements attract the attention as they have the great potential of increasing electron conductivity. Titanium is believed to have high electronic conductivity at high temperature [31]. Primdahl [32] reported that Cr doping could enhance electronic conductivity by reducing Cr^{4+} to Cr^{3+}. Pr is also promising in improving electronic conductivity. Magraso [33] increase the conductivity by doping Pr and Gd at the same time. $BaZr_{0.9-x}Pr_xGd_{0.1}O_{3-\delta}$ was concluded to have larger conductivity with larger Pr content.

Therefore, $SrCeO_3$ based materials such as $SrCe_{1-x}Ti_xO_{3-\delta}$, $SrCe_{1-x}Cr_xO_{3-\delta}$ and $SrCe_{1-x}Pr_xO_{3-\delta}$ were investigated for their great potential to increase electron conductivity.

2.2 Experiment

Perovskite oxides $SrCeO_3$ were prepared through conventional solid-state reaction as base for comparison to other doped materials. $SrCO_3$ (99.99%, Sigma Aldrich) and CeO_2 (99.99%, Alfa Aesar) were mixed by ball-mill with same weight of alcohol in the specific stoichiometric ratio for at least 24 hrs. A stainless steel pan was used for drying the mixed powder. The powder mixture was ground in a mortar and transferred to an alumina crucible. Then $SrCeO_3$ was calcined for 6 hours at 1150 °C in air. The purity of the phase was examined by X-ray diffraction (XRD) with CuKα radiation. Ball-mill the powder after calcination for 24 hours in ethanol. The calcined oxides were pressed into 1cm-diameter pellets (0.8g $SrCeO_3$ powder per pellet). The pellets were sintered at 1450 °C for 4hours.

Similar to the solid-state reaction above, $SrCe_{0.9}Y_{0.1}O_{3-\delta}$ was synthesized with $SrCO_3$, CeO_2 and Y_2O_3 (99.99%, Sigma Aldrich). $SrCe_{0.8}Y_{0.1}Ti_{0.1}O_{3-\delta}$ was calcined with $SrCO_3$, CeO_2, Y_2O_3 and TiO_2 (99%, Sigma Aldrich). $SrCe_{0.9-x}Y_{0.1}Nb_xO_{3-\delta}$ (x=0.05 and 0.1) was synthesized through $SrCO_3$, CeO_2, Y_2O_3 and Nb_2O_5 (99.99%, Sigma Aldrich). Polycrystalline $SrCe_{1-x}Ti_xO_{3-\delta}$ (x=0.05, 0.08, 0.1,0.2, 0.3) samples were synthesized with $SrCO_3$, CeO_2 and TiO_2. $SrCe_{1-x}Cr_xO_{3-\delta}$ (x=0.05, 0.08, 0.1) samples were prepared with $SrCO_3$, CeO_2 and Cr_2O_3 (99.9%, Sigma Aldrich). $SrCe_{1-x}Pr_xO_{3-\delta}$ (x=0.05, 0.08, 0.1, 0.15, 0.2, 0.3) series were synthesized with $SrCO_3$, CeO_2 and Pr_6O_{11} (99.9%, Sigma Aldrich). They were calcined at 1150°C for 6 hours in the

furnace with the ramp rate of 5°C/min. XRD was used for determining the phase structures of the synthesized materials.

2.3 Results and Analysis

Polycrystalline $SrCe_{0.9}Y_{0.1}O_{3-\delta}$ material was synthesized as a reference of double-doping B sites materials. It has been demonstrated that conductivity of $SrCe_{0.9}Y_{0.1}O_{3-\delta}$ is significantly higher than $SrCeO_3$. XRD result shows that $SrCe_{0.9}Y_{0.1}O_{3-\delta}$ is pure crystalline after calcination at 1150°C for 6 hours (Figure 2-1). Doping B sites with Yttrium is believed to highly improve proton conductivity as more oxygen vacancies are generated because of the disordered structure. In order to enhance electron conductivity of $SrCe_{0.9}Y_{0.1}O_{3-\delta}$, double doping was recommended and investigated.

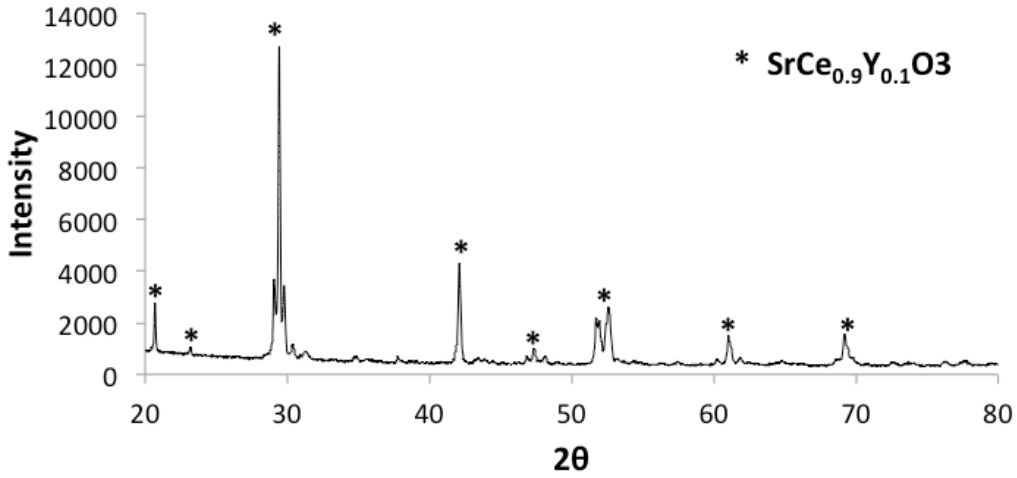

Figure 2-1 XRD pattern of SCY power calcined at 1150°C

Niobium is a promising dopant of improving electron conductivity due to its multi stable valence. Yttrium is stable at +3 and Niobium is stable at +5. These two dopants may form a perfect pair with Y improving proton conductivity by forming more

vacancies. Additionally, Nb can increase electron conductivity by changing its valence and forming electron holes. However, the size of the atoms may not match the structure and could diminish the conductivity. $SrCe_{0.8}Y_{0.1}Nb_{0.1}O_{3-\delta}$ and $SrCe_{0.85}Y_{0.1}Nb_{0.05}O_{3-\delta}$ samples were synthesized and investigated. The tolerance number of 10% Niobium doping material was calculated to be 0.89266 while the 5% Niobium doping material was 0.90554. 5% Niobium-doping material is theoretically closer to perovskite structure based on the tolerance number. Figure 2-2 and 2-3 show the XRD patterns of these materials. Both materials were not single phase according to the XRD analysis. However, 5% Nb doping seems to have Niobium integrated into the perovskite structure. There are small amount of cerium oxide precipitate in both materials. $SrCe_{0.8}Y_{0.1}Nb_{0.1}O_{3-\delta}$ is analyzed to have three phases in the complex. Nb is possible to form a new material without doping into the structure.

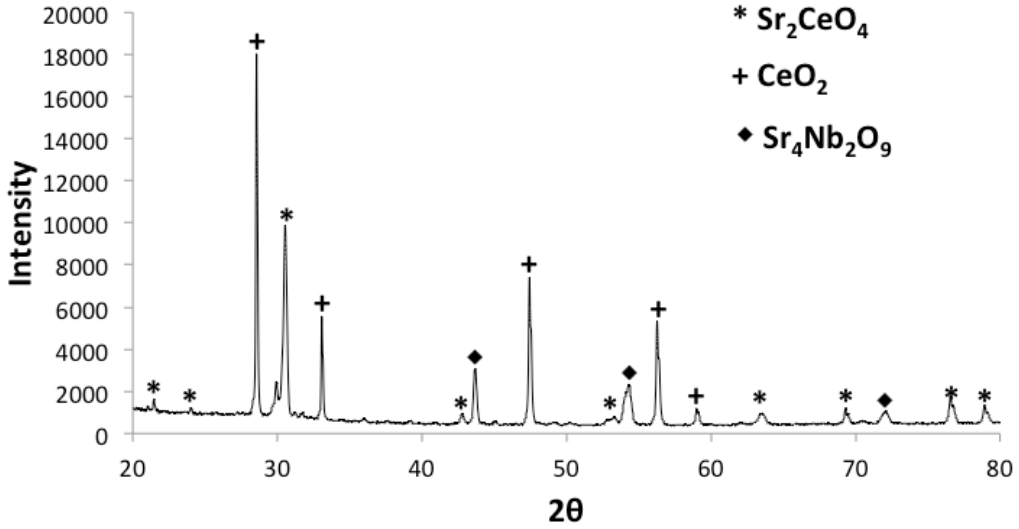

Figure 2-2 XRD pattern analyzed of $SrCe_{0.8}Y_{0.1}Nb_{0.1}O_{3-\delta}$ power

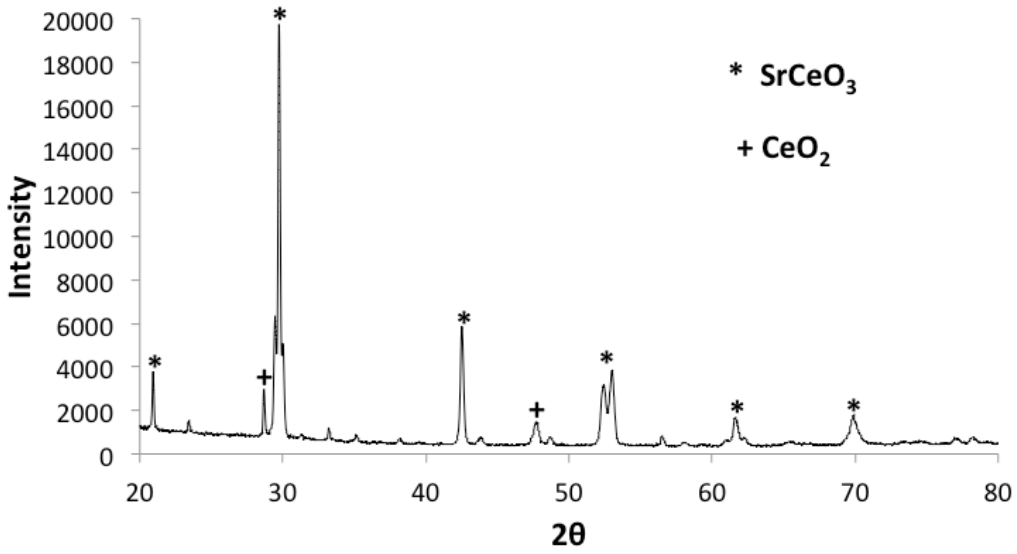

Figure 2-3 XRD pattern analyzed of $SrCe_{0.85}Y_{0.1}Nb_{0.05}O_{3-\delta}$ powder

Titanium Yttrium double doping was also investigated. XRD results of $SrCe_{0.8}Ti_{0.1}Y_{0.1}O_{3-\delta}$ (Figure 2-4) also showed that a secondary phase exists in the material after calcination. The tolerance number of $SrCe_{0.8}Ti_{0.1}Y_{0.1}O_{3-\delta}$ is 0.894 which indicates that it may not be a stable perovskite structure.

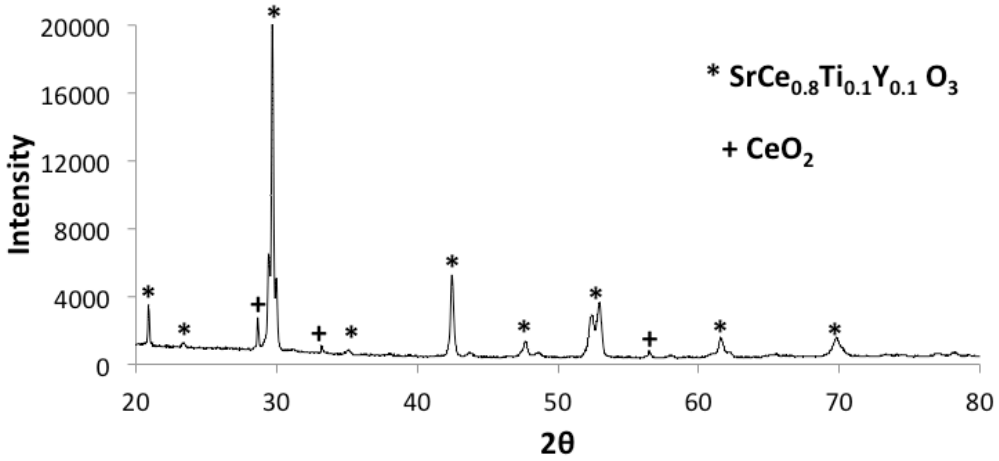

Figure 2-4 XRD pattern analyzed of $SrCe_{0.8}Ti_{0.1}Y_{0.1}O_{3-\delta}$ powder

Titanium is believed to have electron conductivity. Ti doped $SrCeO_3$ was explored to determine the effect of this dopant on conductivity. The theoretical tolerance numbers

of $SrCe_{0.9}Ti_{0.1}O_{3-\delta}$, $SrCe_{0.8}Ti_{0.2}O_{3-\delta}$ and $SrCe_{0.7}Ti_{0.3}O_{3-\delta}$ are 0.8952, 0.906 and 0.9169. The larger doping amount of Ti at B sites the closer the tolerance number to one. All of these materials are orthorhomic structure. The XRD patterns indicate that the 5%, 8% and 10% doped materials are pure phase (Figure 2-5). On the contrary, 20% and 30% Titanium doped have secondary phases (Figure 2-6). It is proposed that 10% doping amount is the limitation amount of having single phase.

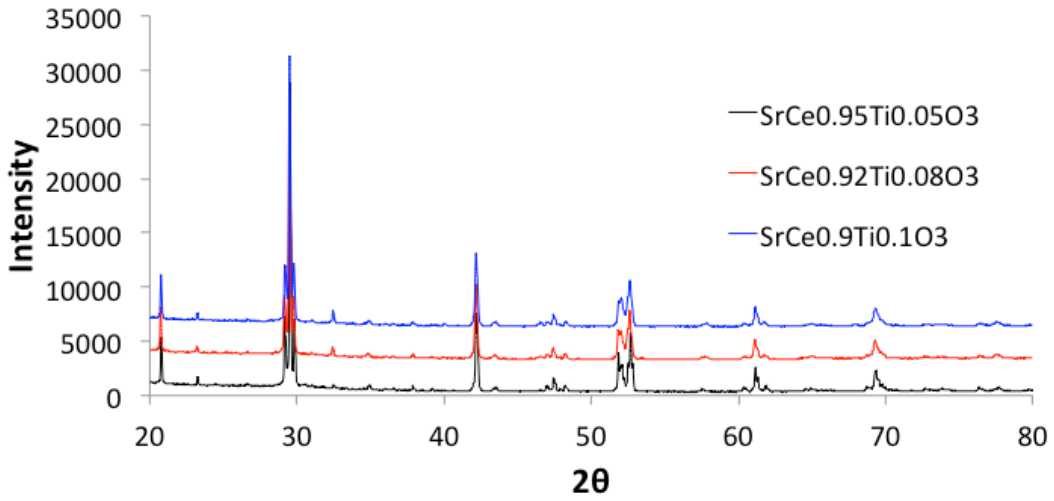

Figure 2-5 XRD pattern analyzed of $SrCeO_3$ doped with 5%, 8% and 10% Ti

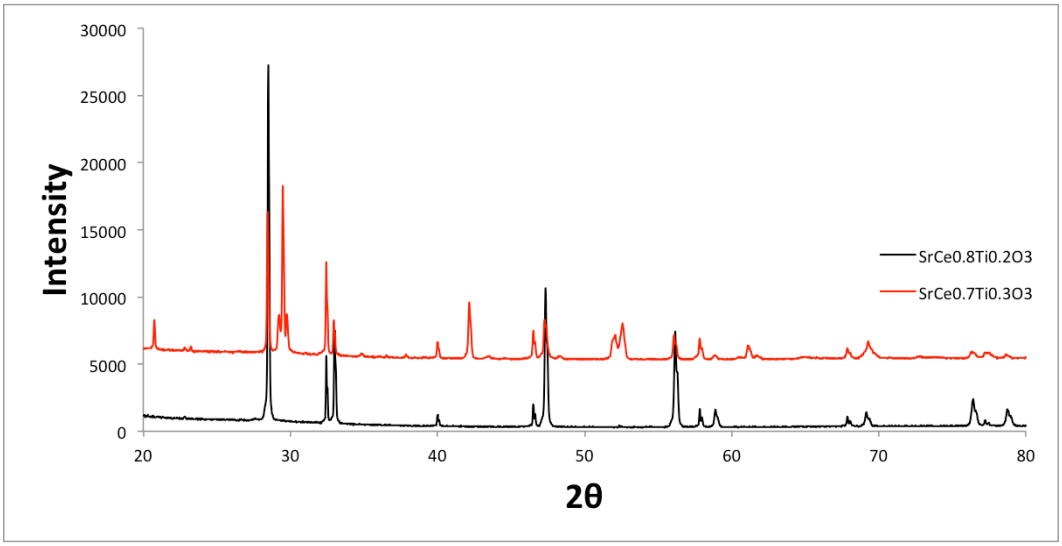

Figure 2-6 XRD pattern analyzed of $SrCeO_3$ doped with 20% and 30% Ti

It is widely reported that chromium has great potential of enhancing electron conductivity for the reason that Cr can change from Cr^{3+} to Cr^{4+} and release an electron. The potential energy needed of the valence change determines the electron conductivity properties. XRD patterns in Figure 2-7 show that 5%, 8% and 10% doping of Chromium at B sites formed a single pure phase. Although the identical peaks are almost at the exactly same position, there are small split and shift of the peaks, which can be clearly defined in Figure 2-8. 5% doped material shows no obvious split. But 8% and larger doping amount exist splits. The intensity of the peak for 10% Cr doped material is higher than other materials.

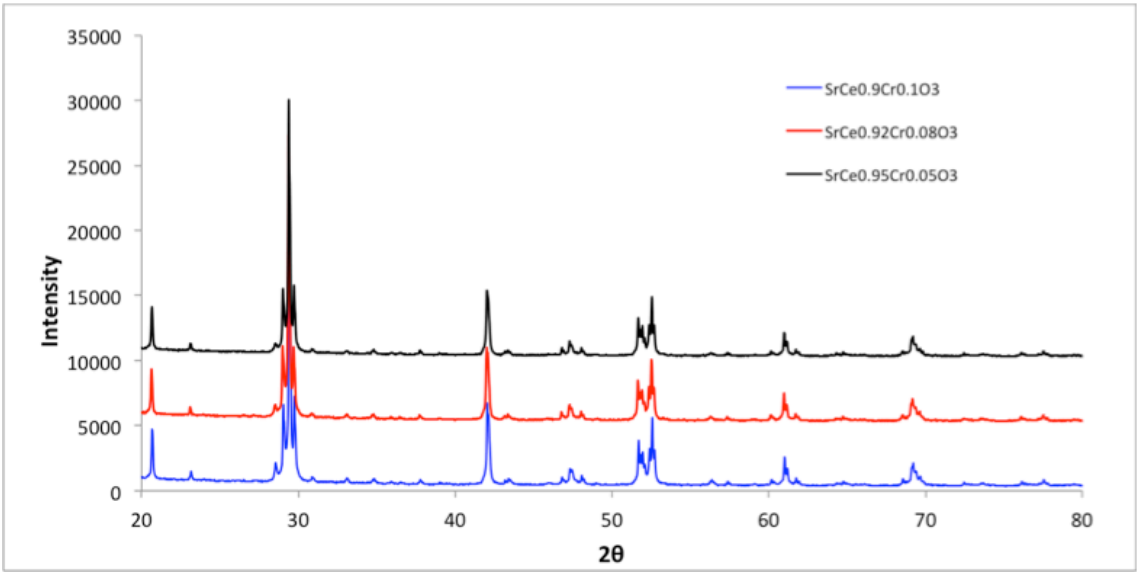

Figure 2-7 XRD pattern analyzed of $SrCeO_3$ doped with 5%, 8% and 10% Cr

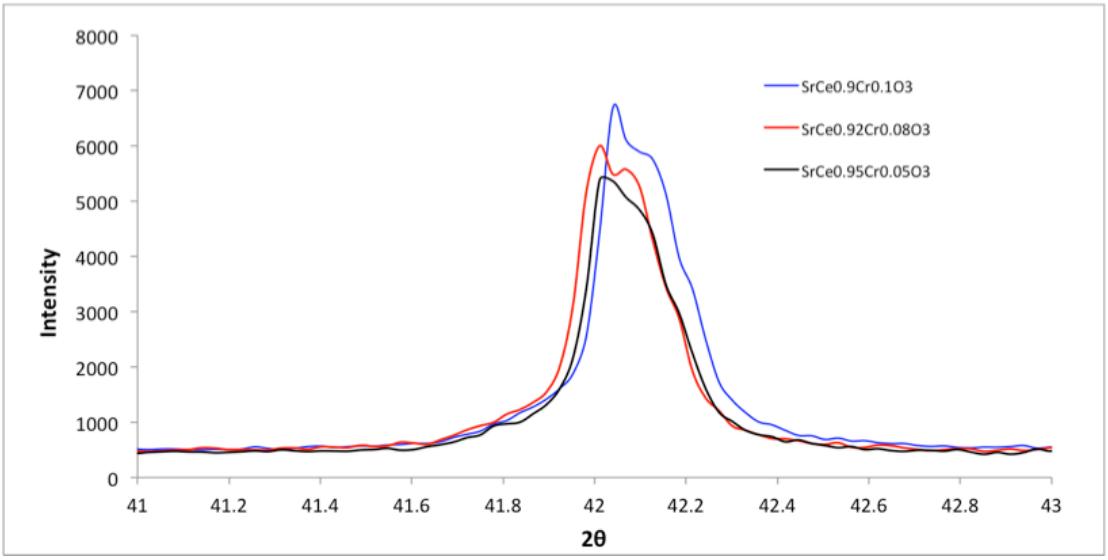

Figure 2-8 Peak shift and split of different doping amount

Although XRD patterns shown in Figure 2-9 demonstrated that different doping amount of Praseodymium materials have been synthesized in its desired ratio. There are small distinguishable changes of different materials (Figure 2-10). An identical property of $SrCe_{0.95}Pr_{0.05}O_{3-\delta}$ is observed different of other materials. 5% Pr-doped strontium cerate is sandy like powder that cannot be dense at 1450 °C. The pellets will crack form inside and remain sandy like status after calcination. This property is unique for this new material that never reported before. However, $SrCe_{0.95}Pr_{0.05}O_{3-\delta}$ is definitely not promising material for the dense membrane in the membrane reactors.

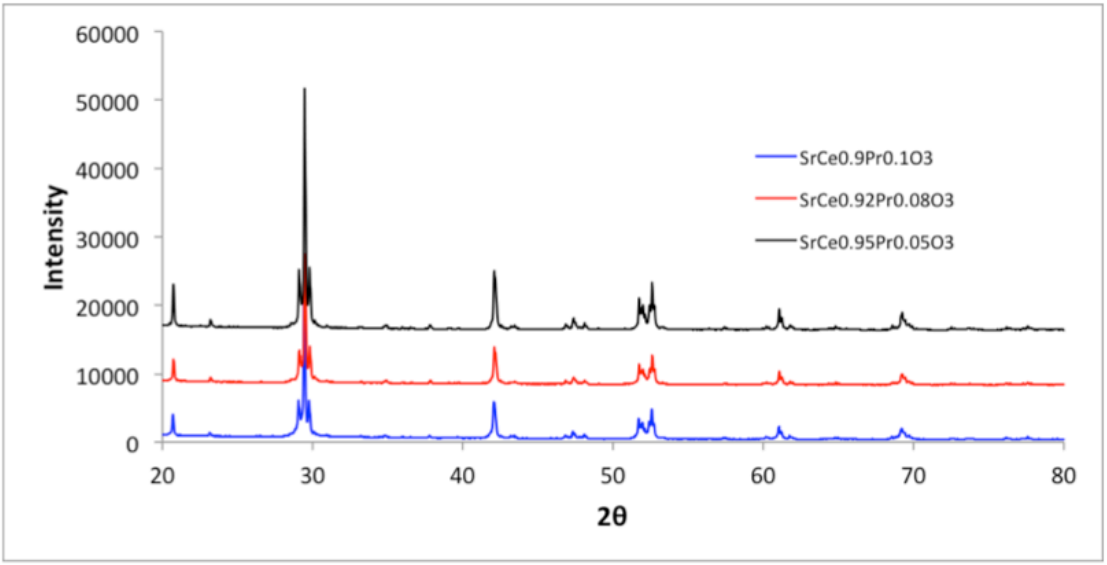

Figure 2-9 XRD pattern analyzed of $SrCeO_3$ doped with 5%, 8% and 10% Pr

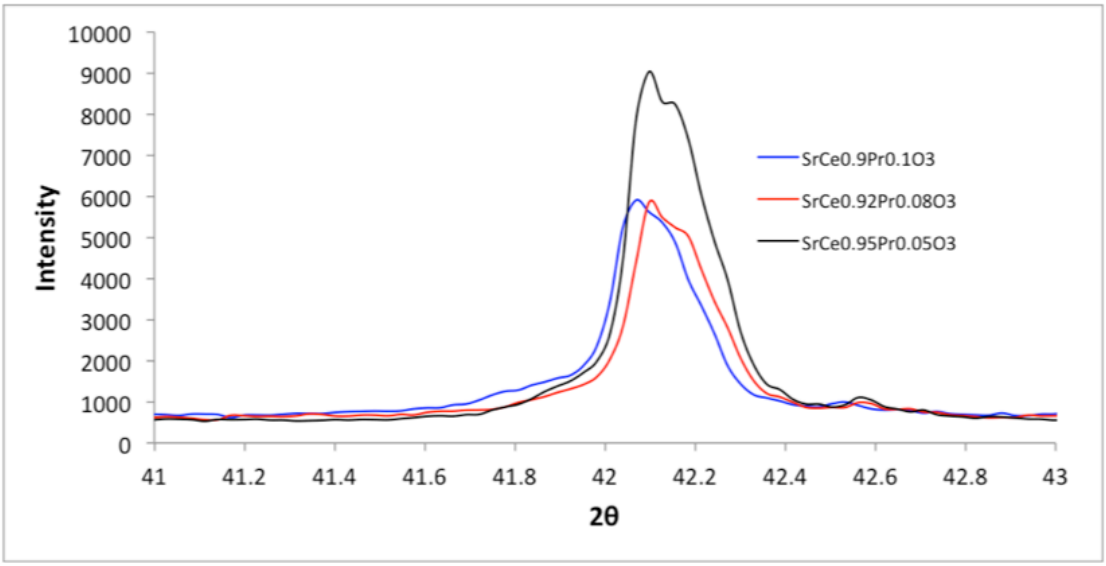

Figure 2-10 Peak shift and intensity change of different doping amount

The Titanium-doped, Chromium-doped and Praseodymium-doped Strontium Cerate Oxides have pure phase and the sintered pellets were used for EIS measurements in Chapter 3. Although $SrCe_{0.8}Y_{0.1}Ti_{0.1}O_{3-\delta}$ and $SrCe_{0.9-x}Y_{0.1}Nb_xO_{3-\delta}$ (x=0.05 and 0.1) have secondary phase, the conductivities of these material were also measured in next chapter.

Chapter 3: Total Conductivity of the new materials

3.1 Introduction

The total conductivities of the new materials synthesized in Chapter 2 reflect the sum of the ion conductivity and electron conductivity of the MIEC material. The oxygen ion transfer can be neglected under hydrogen condition. Therefore, the proton conductivity and electron conductivity is considered to be the total conductivity. Electrochemical impedance spectroscopy [34] is a well-known electrochemistry method that can be used to obtain the resistant of the cell and total conductivity can be calculated.

The total conductivities of $SrCe_{1-x}Eu_xO_{3-\delta}$ under dry hydrogen were investigated in previous work [35]. Pt electrodes were applied on the 10mm diameter x 2mm thickness dense pellets. Conductivity measurements were performed with a Solartron 1260 Impedance Analyzer. The conductivity (Figure 3-1 a) shows an increase with temperature and the highest total conductivity was observed for 10 mol% Eu-doped material. The activation energies were 0.49-0.59 eV for 10 mol% and 15 mol% Eu-doped material (Figure 3-1 b). 20 mol% Eu-doped material had the highest activation energy (0.89 eV).

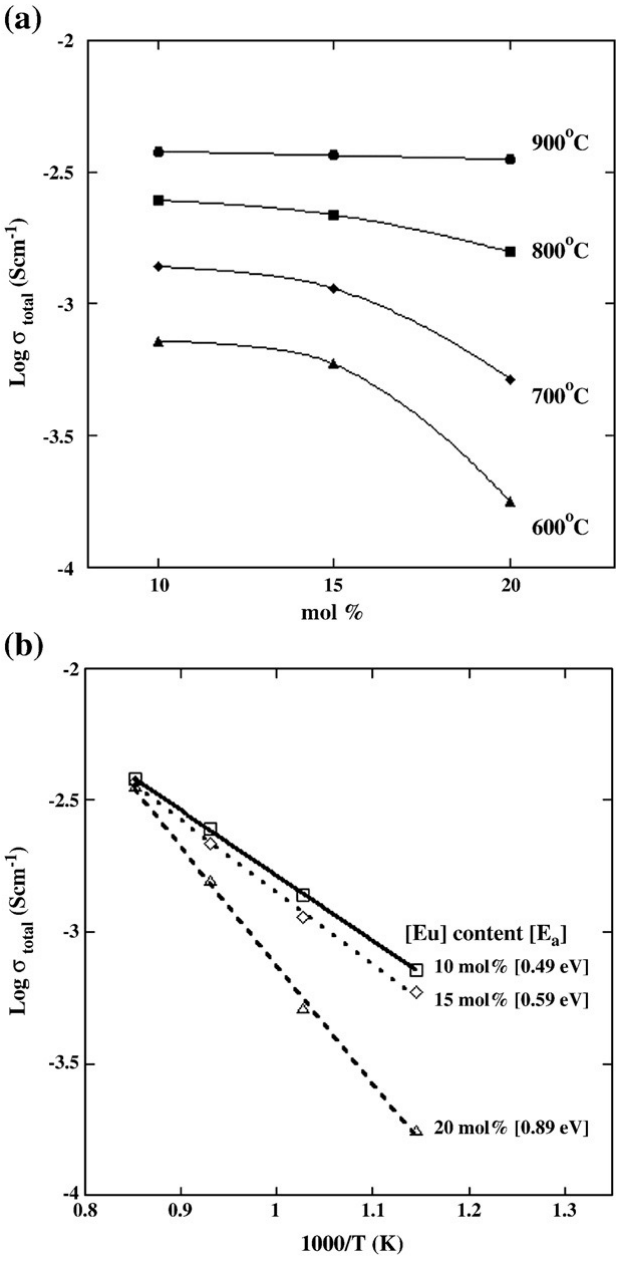

Figure 3-1 Total conductivity of different Eu-doped $SrCe_{1-x}Eu_xO_{3-\delta}$ between 600 °C and 900 °C under dry hydrogen atmosphere [35].

3.2 EIS measurement

For comparing the total conductivities of the new materials, all the pellets sintered in chapter 2 were performed with Pt electrodes. All of the pellets were connected four electrodes at the two sides of the sample with Platinum pastes (Fuel Cell materials) and platinum wires (A-M system, 0.005 inches). The total conductivities of were measured through Electrochemical Impedance Spectroscopy (EIS) method. A quartz reactor (Figure 3-2) in a tubular furnace was used for measuring EIS under 10% Hydrogen in Nitrogen condition and 10% hydrogen in nitrogen (with 3% water vapor) condition.

The total conductivities of $SrCeO_3$, $SrCe_{0.9}Y_{0.1}O_{3-\delta}$, $SrCe_{0.85}Y_{0.1}Nb_{0.05}O_{3-\delta}$, $SrCe_{1-x}Ti_xO_{3-\delta}$ (x=0.05; 0.08; 0.1), $SrCe_{1-x}Cr_xO_{3-\delta}$ (x=0.05; 0.08; 0.1) and $SrCe_{1-x}Pr_xO_{3-\delta}$ (x=0.08, 0.1, 0.15, 0.2) were measured in different gas environments. The total conductivity were measured at 600-800 °C. The gas environments supplied into the reactor are in the order: Air; Air (with 3% water vapor); Nitrogen; Nitrogen (with 3% water vapor); 10% Hydrogen in Nitrogen; and 10% hydrogen in nitrogen (with 3% water vapor). Flow meter controller was used to set the total gas flow rate at 100 sccm. EIS was measured by solartron SI 1260 (Impedance/gain-phase analyzer) from frequencies of 0.1Hz to 10^7 Hz.

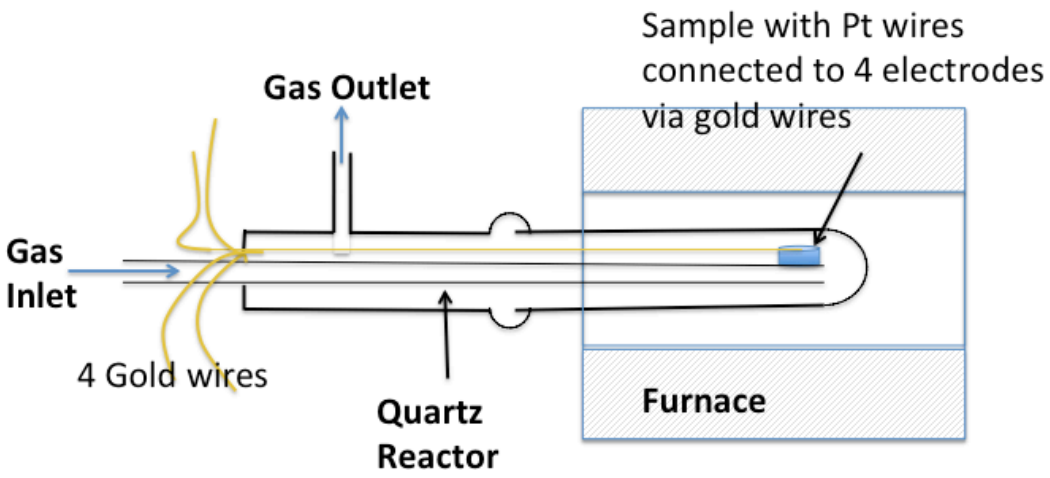

Figure 3-2 Schematic of the apparatus for conductivity measurement.

3.3 Results and Analysis

EIS was measured for Pr-doped $SrCe_{1-x}Pr_xO_{3-\delta}$ (x=0.08, 0.1, 0.15, 0.2) materials in 0.83cm diameter pellets. The real and imaginary components of the impedance are plotted in the complex plane as parametric functions of frequency. Typically, there are three arcs observed in the plot. The arc present at high frequencies normally attributed to bulk material behavior, that present at intermediate frequencies attributed to grain boundary behavior, and that present at low frequencies attributed to electrode behavior. The electrodes information can be obtained from the low frequency section in the Nyquist plot. The higher the temperature leads to a smaller radius of the arc that reflecting the resistance value. The resistance decreases largely with the increasing temperature. The electrodes are platinum paste connected with platinum wires that has active catalytically properties in hydrogen environment.

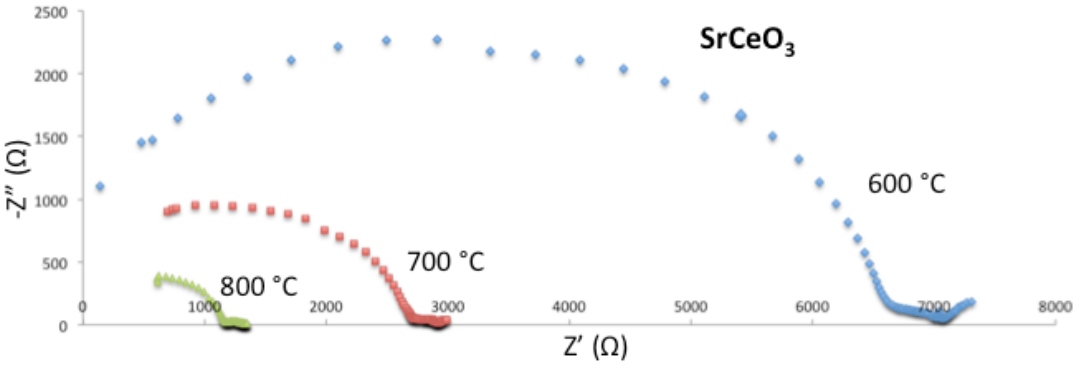

Figure 3-3 Nyquist plot of $SrCeO_3$ measured in 90sccm N_2; 10sccm H_2; 3% H_2O

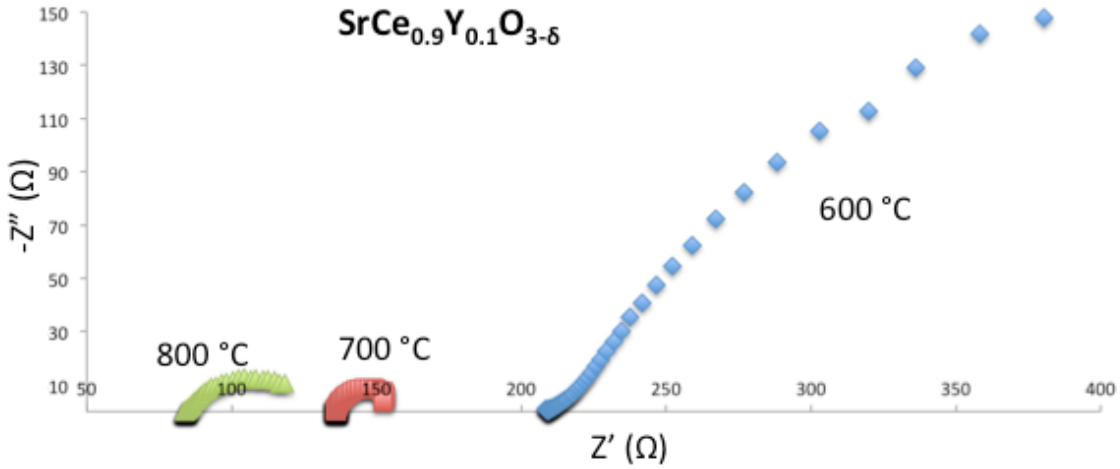

Figure 3-4 Nyquist plot of $SrCe_{0.9}Y_{0.1}O_{3-\delta}$ measured in 90sccm N_2; 10sccm H_2; 3% H_2O

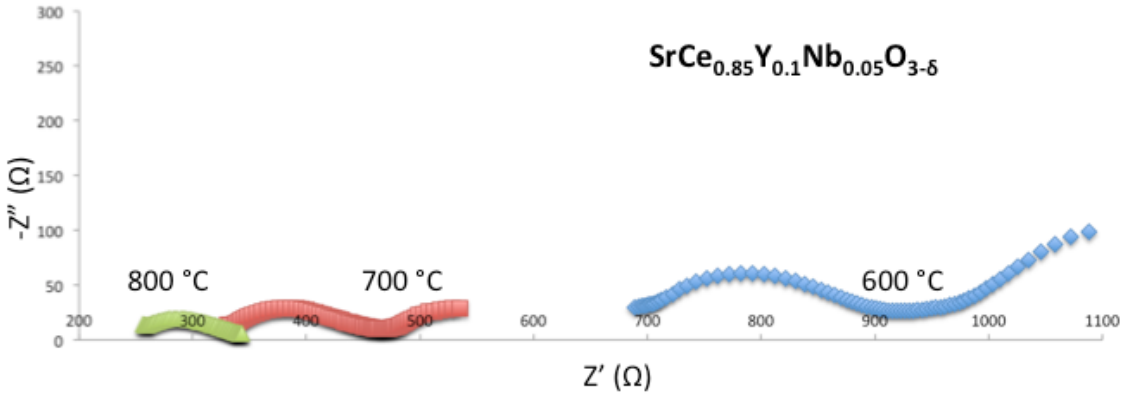

Figure 3-5 Nyquist plot of $SrCe_{0.85}Y_{0.1}Nb_{0.05}O_{3-\delta}$ measured in 90sccm N_2; 10sccm H_2; 3% H_2O

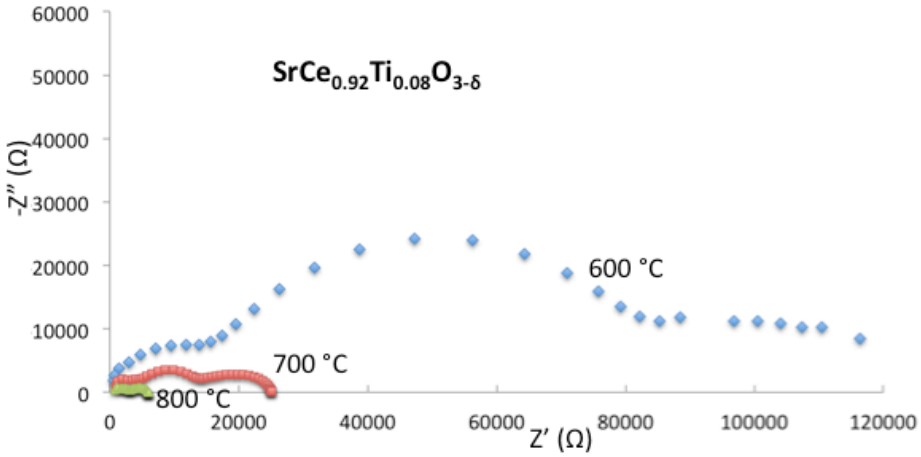

Figure 3-6 Nyquist plot of $SrCe_{0.92}Ti_{0.08}O_{3-\delta}$ measured in dry air

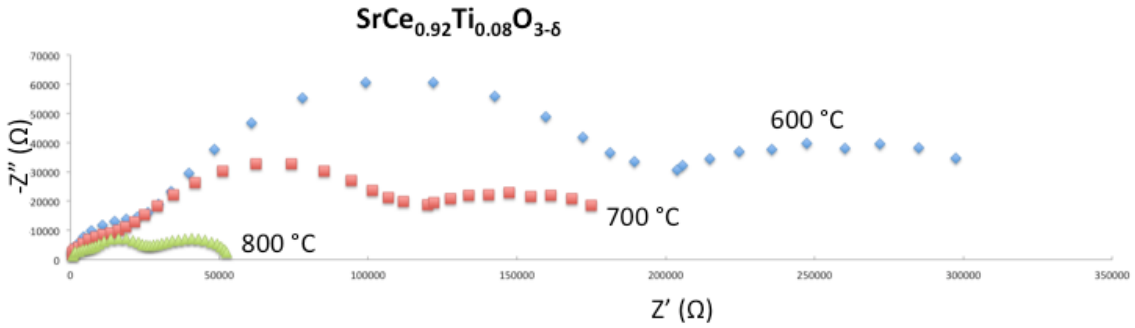

Figure 3-7 Nyquist plot of $SrCe_{0.92}Ti_{0.08}O_{3-\delta}$ measured in air (with 3%H_2O)

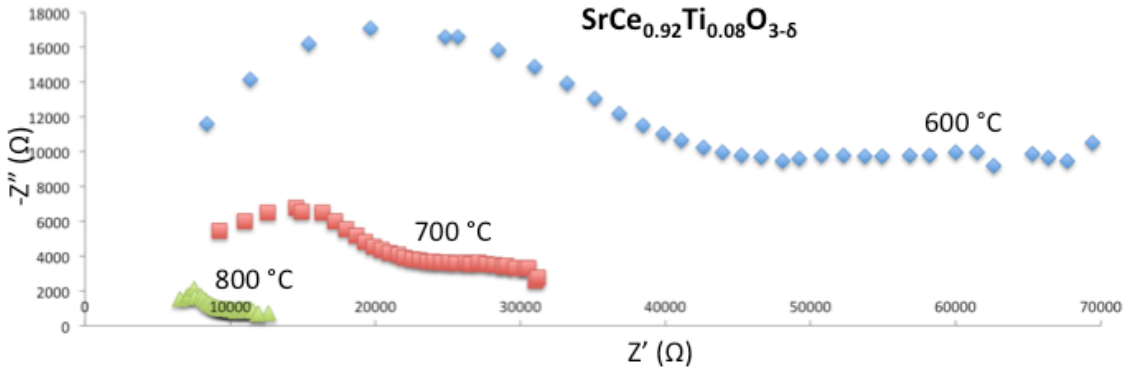

Figure 3-8 Nyquist plot of $SrCe_{0.92}Ti_{0.08}O_{3-\delta}$ measured in dry N_2

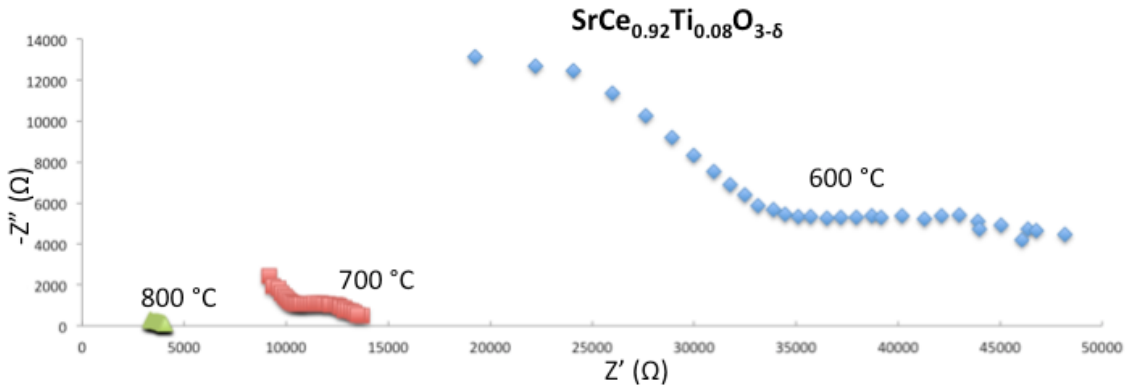

Figure 3-9 Nyquist plot of $SrCe_{0.92}Ti_{0.08}O_{3-\delta}$ measured in N_2 (with 3%H_2O)

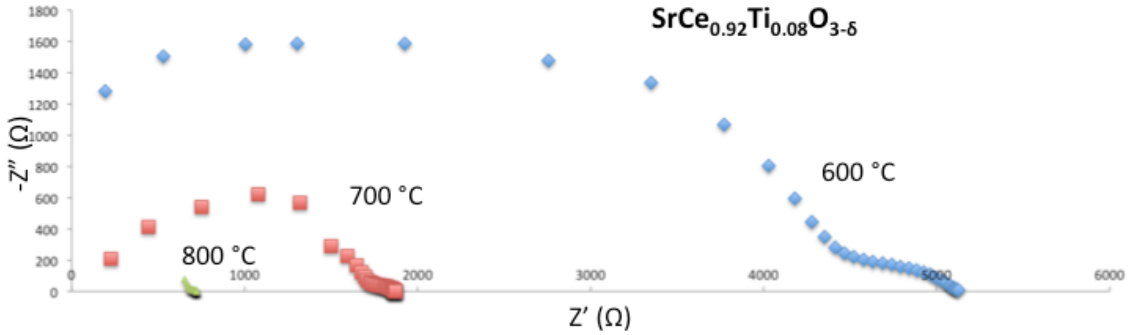

Figure 3-10 Nyquist plot of $SrCe_{0.92}Ti_{0.08}O_{3-\delta}$ measured in 90sccm N_2; 10sccm H_2

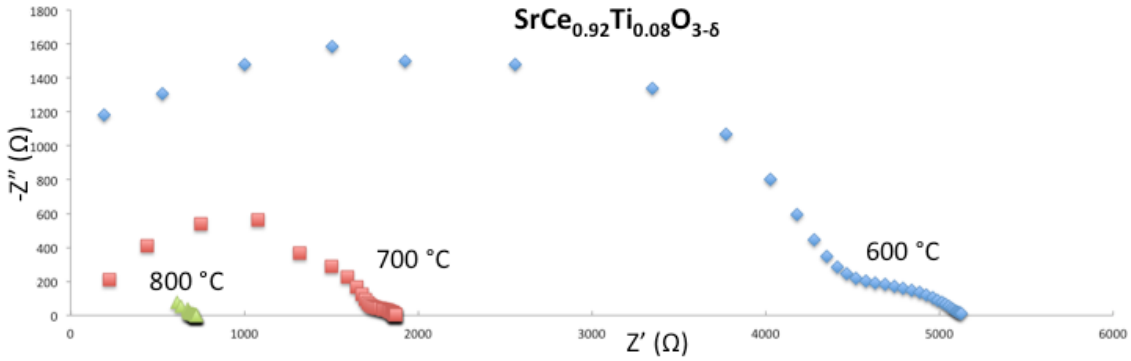

Figure 3-11 Nyquist plot of $SrCe_{0.92}Ti_{0.08}O_{3-\delta}$ measured in 90sccm N_2; 10sccm H_2; 3%H_2O

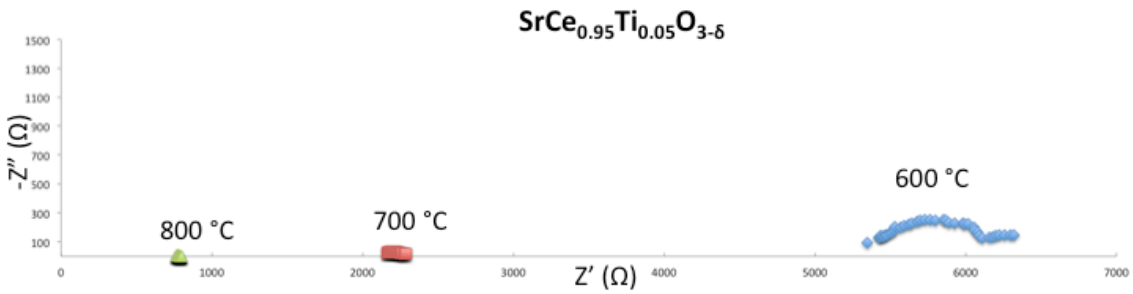

Figure 3-12 Nyquist plot of $SrCe_{0.95}Ti_{0.05}O_{3-\delta}$ measured in 90sccm N_2; 10sccm H_2; 3%H_2O

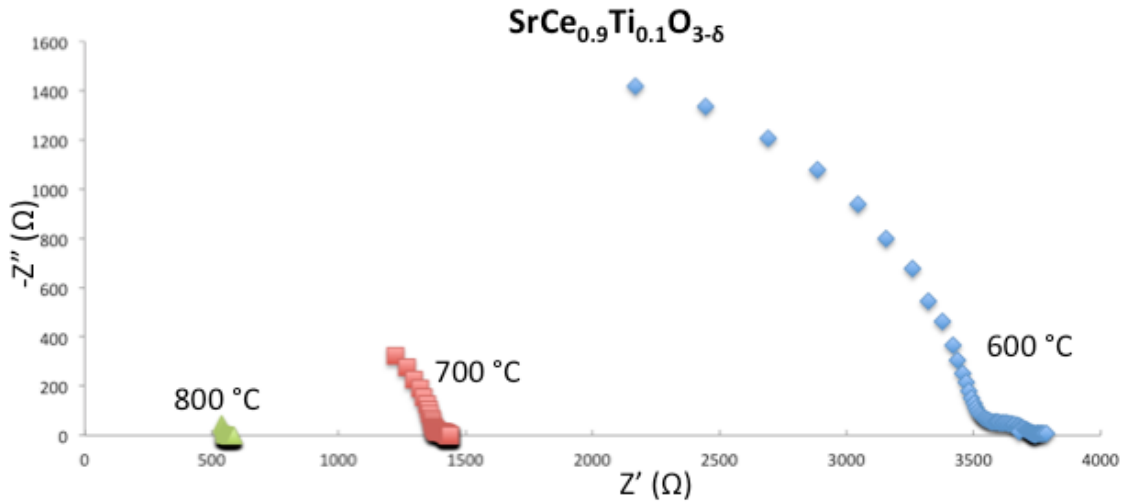

Figure 3-13 Nyquist plot of $SrCe_{0.9}Ti_{0.1}O_{3-\delta}$ measured in 90sccm N_2; 10sccm H_2; 3%H_2O

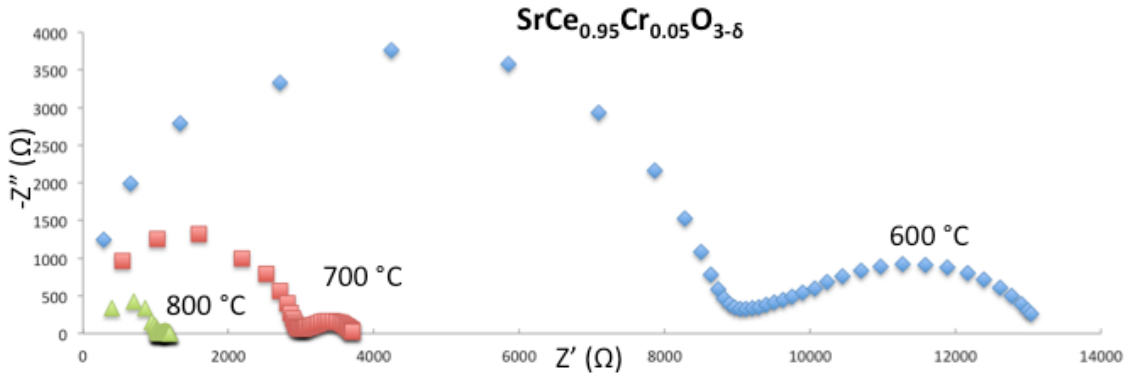

Figure 3-14 Nyquist plot of $SrCe_{0.95}Cr_{0.05}O_{3-\delta}$ measured in 90sccm N_2; 10sccm H_2; 3%H_2O

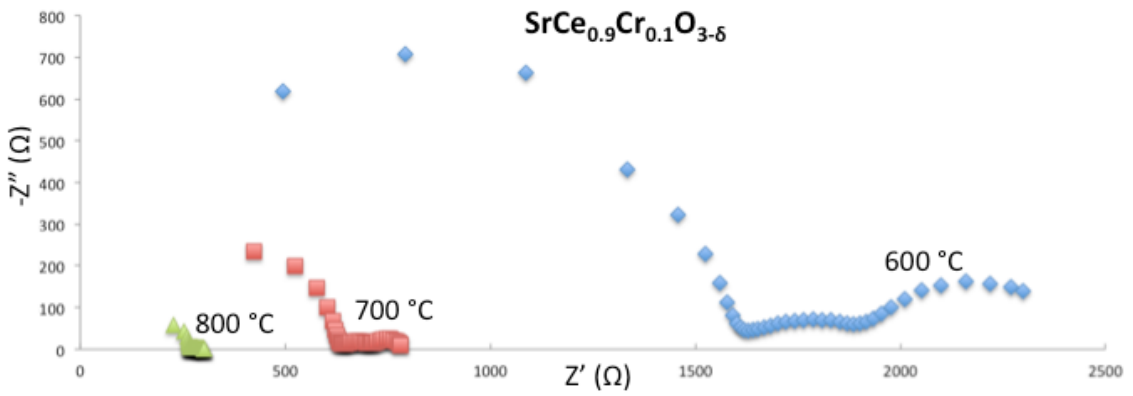

Figure 3-15 Nyquist plot of $SrCe_{0.9}Cr_{0.1}O_{3-\delta}$ measured in 90sccm N_2; 10sccm H_2; 3%H_2O

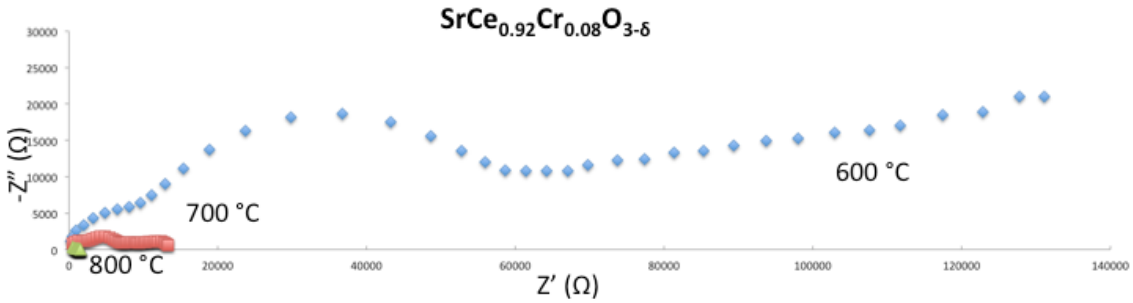

Figure 3-16 Nyquist plot of $SrCe_{0.92}Cr_{0.08}O_{3-\delta}$ measured in dry air

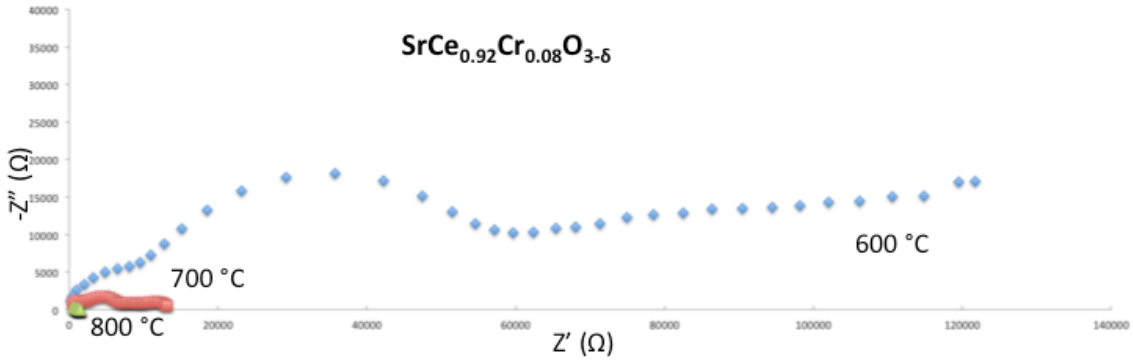

Figure 3-17 Nyquist plot of $SrCe_{0.92}Cr_{0.08}O_{3-\delta}$ measured in air (with 3%H_2O)

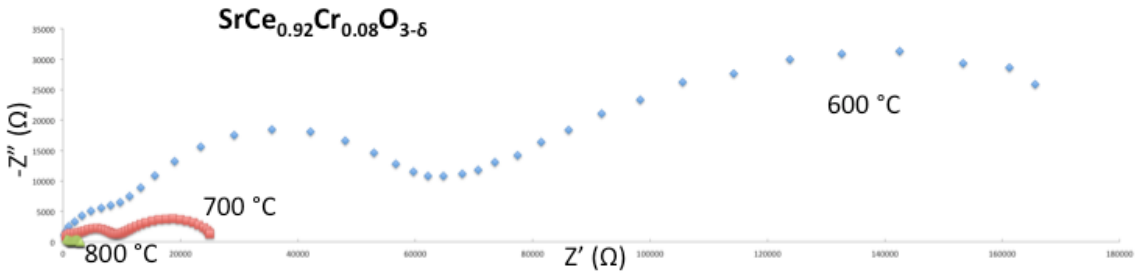

Figure 3-18 Nyquist plot of $SrCe_{0.92}Cr_{0.08}O_{3-\delta}$ measured in dry N_2

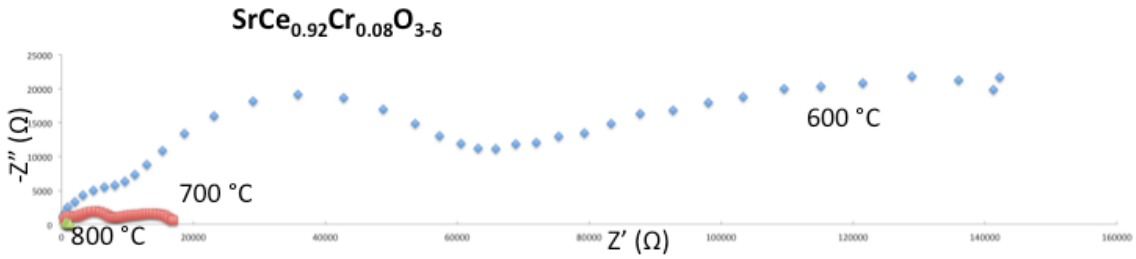

Figure 3-19 Nyquist plot of $SrCe_{0.92}Cr_{0.08}O_{3-\delta}$ measured in N_2 (with 3%H_2O)

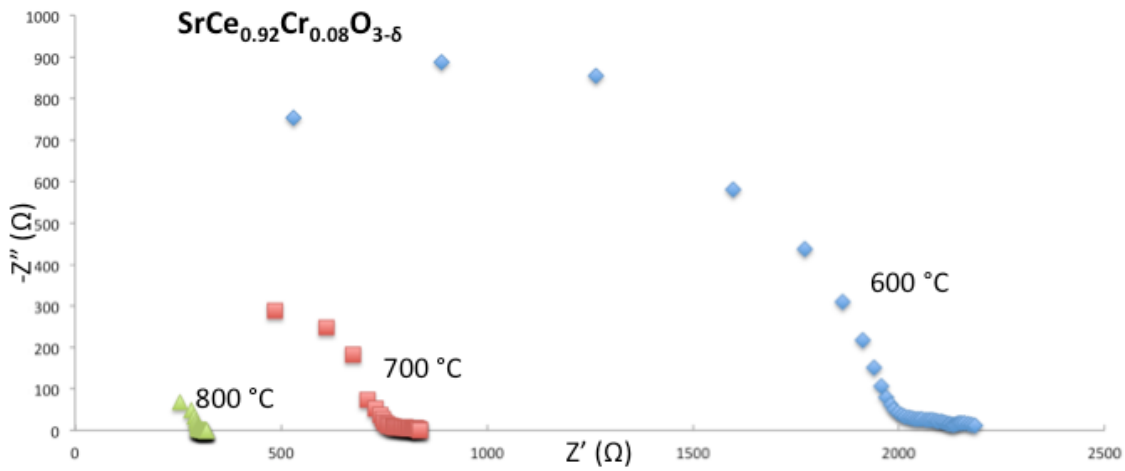

Figure 3-20 Nyquist plot of $SrCe_{0.92}Cr_{0.08}O_{3-\delta}$ measured in 90sccm N_2; 10sccm H_2

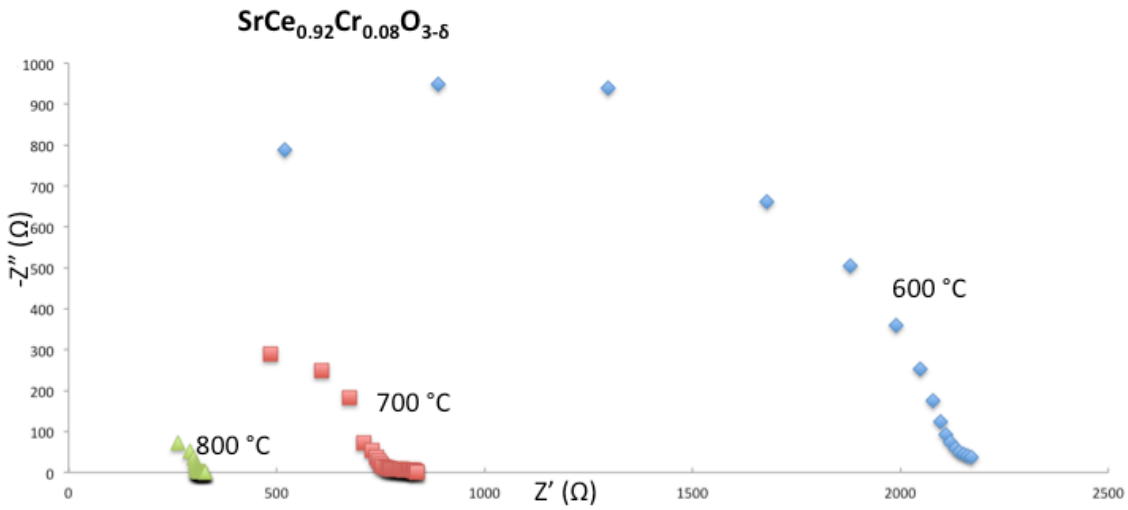

Figure 3-21 Nyquist plot of $SrCe_{0.92}Cr_{0.08}O_{3-\delta}$ measured in 90sccm N_2; 10sccm H_2; 3%H_2O

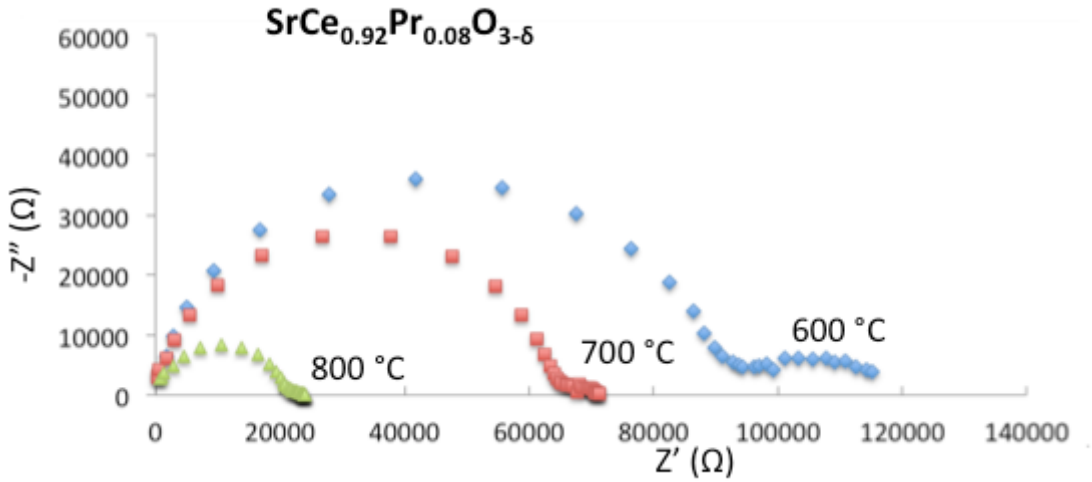

Figure 3-22 Nyquist plot of $SrCe_{0.92}Pr_{0.08}O_{3-\delta}$ measured in dry air

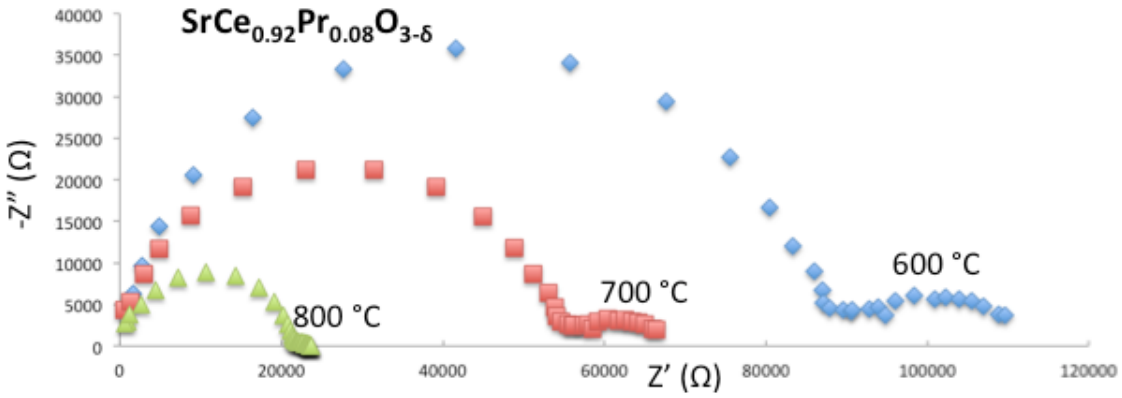

Figure 3-23 Nyquist plot of $SrCe_{0.92}Pr_{0.08}O_{3-\delta}$ measured in air (with 3%H_2O)

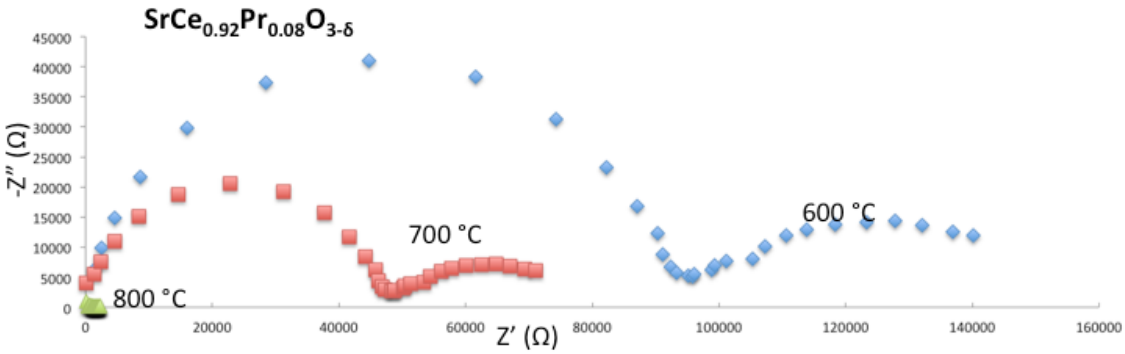

Figure 3-24 Nyquist plot of $SrCe_{0.92}Pr_{0.08}O_{3-\delta}$ measured in dry N_2

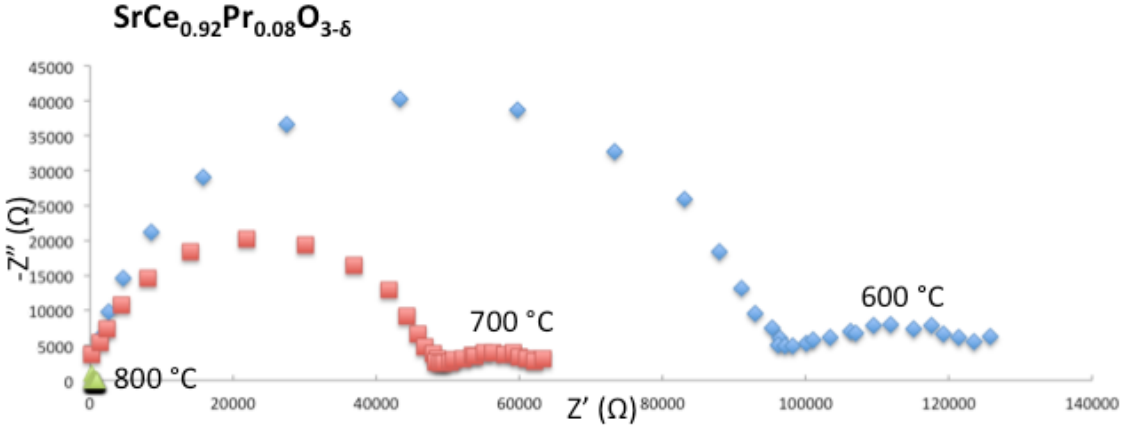

Figure 3-25 Nyquist plot of $SrCe_{0.92}Pr_{0.08}O_{3-\delta}$ measured in N_2 (with 3%H_2O)

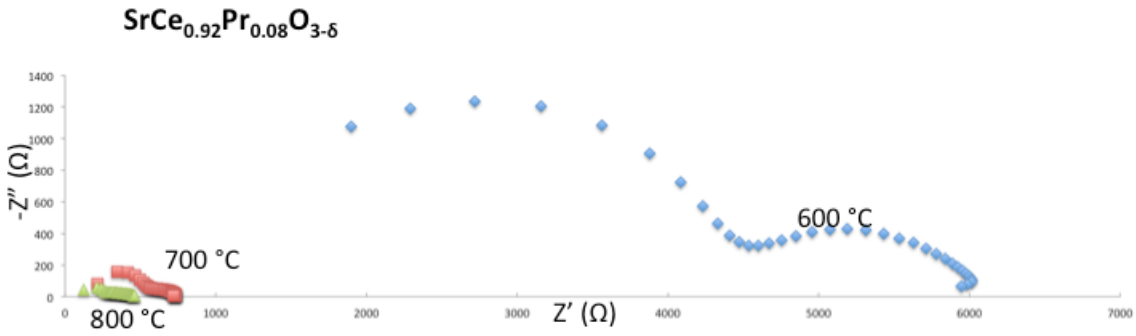

Figure 3-26 Nyquist plot of $SrCe_{0.92}Pr_{0.08}O_{3-\delta}$ measured in 90sccm N_2; 10sccm H_2

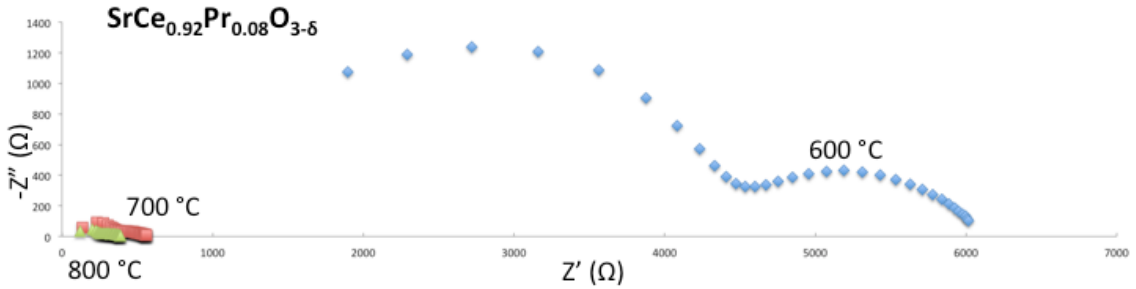

Figure 3-27 Nyquist plot of $SrCe_{0.92}Pr_{0.08}O_{3-\delta}$ measured in 90sccm N_2; 10sccm H_2; 3%H_2O

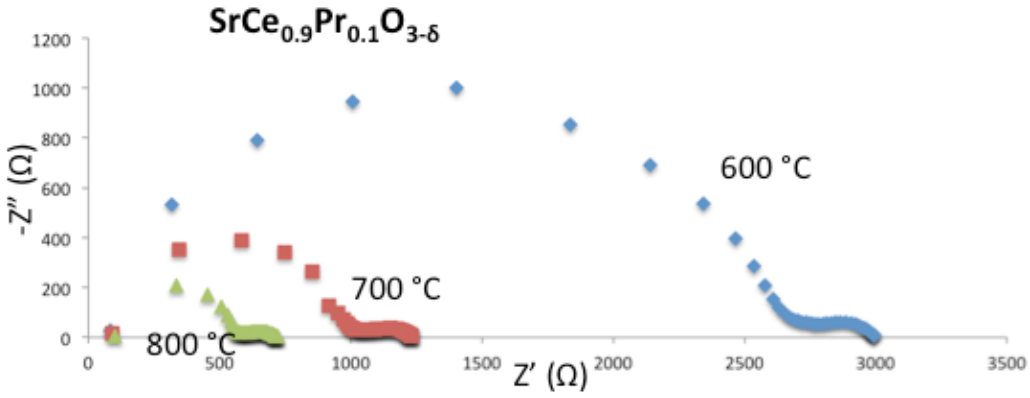

Figure 3-28 Nyquist plot of $SrCe_{0.9}Pr_{0.1}O_{3-\delta}$ measured in 90sccm N_2; 10sccm H_2; 3%H_2O

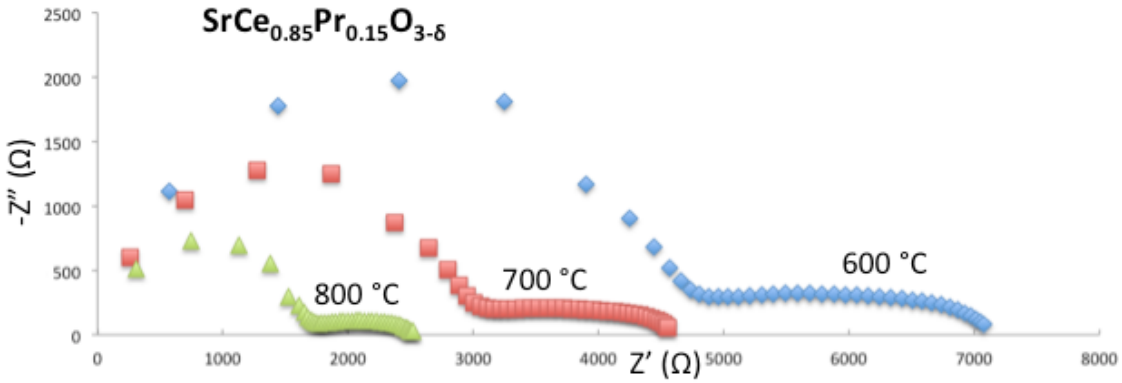

Figure 3-29 Nyquist plot of $SrCe_{0.85}Pr_{0.15}O_{3-\delta}$ measured in 90sccm N_2; 10sccm H_2; 3%H_2O

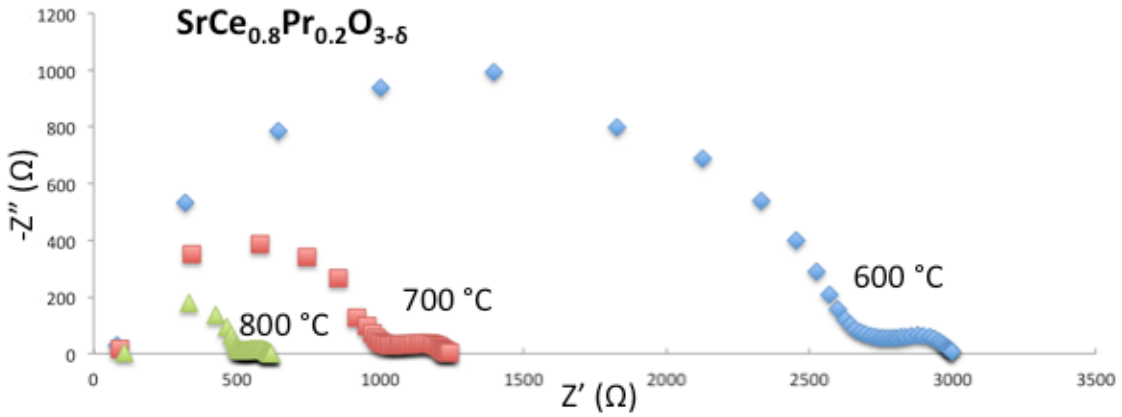

Figure 3-30 Nyquist plot of $SrCe_{0.8}Pr_{0.2}O_{3-\delta}$ measured in 90sccm N_2; 10sccm H_2; 3%H_2O

The Nyquist plots (Figure 3-3 to Figure 3-30) can be obtained for all the materias synthesized in Chapter 2. The total conductivities can be calculated from these plots. The total conductivity of $SrCe_{0.85}Y_{0.1}Nb_{0.05}O_{3-\delta}$ is compared to total conductivity of $SrCe_{0.9}Y_{0.1}O_{3-\delta}$ and $SrCeO_3$ under different temperatures in10% wet hydrogen gas environment (Figure 3-31). It is shown in the figure that the total conductivity increase with increasing temperature. All of the materials fit Arrhenius equation. $SrCe_{0.8}Y_{0.1}Nb_{0.1}O_{3-\delta}$ and $SrCe_{0.9}Y_{0.1}O_{3-\delta}$ are significantly higher than $SrCeO_3$.

$SrCe_{0.9}Y_{0.1}O_{3-\delta}$ has higher conductivity than double-doping materials. It is not what supposed to be according to the pair theory above. The reason is that Niobium dopant creates extra phase, which may decrease the total conductivity. Another possibility is that the electron conductivity is enhanced but the proton conductivity is highly decreased. Therefore, the total conductivity is obviously decreased.

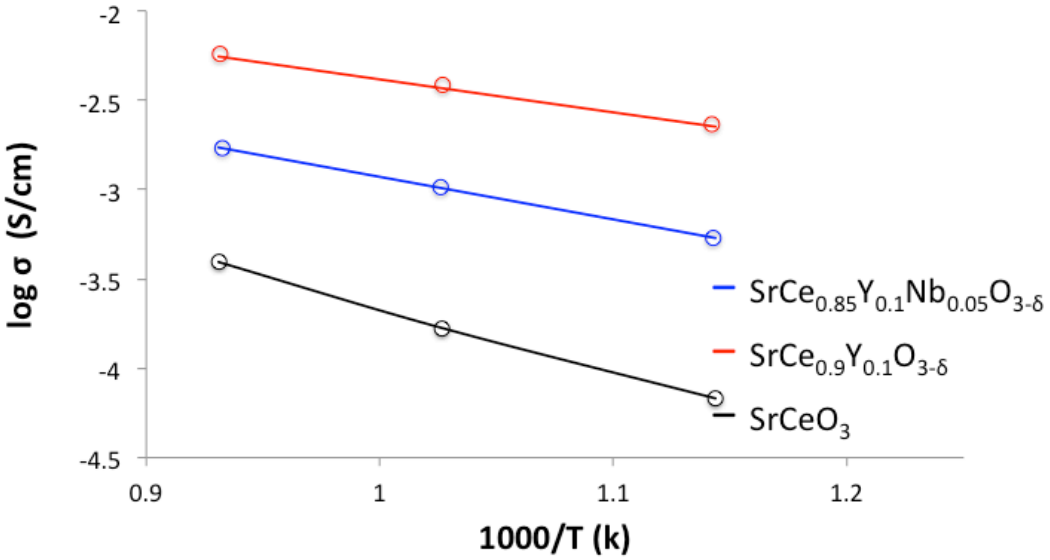

Figure 3-31 Total conductivities of $SrCeO_3$, $SrCe_{0.9}Y_{0.1}O_{3-\delta}$ and $SrCe_{0.85}Y_{0.1}Nb_{0.05}O_{3-\delta}$ dependent of temperature

Total conductivities of the Titanium doping materials are shown in Figure 3-32. The conductivity is creasing with increasing temperature for both of the new materials. Also in Figure 3-33, it is obvious that at certain temperature, the conductivity increases with increasing Titanium doping amount.

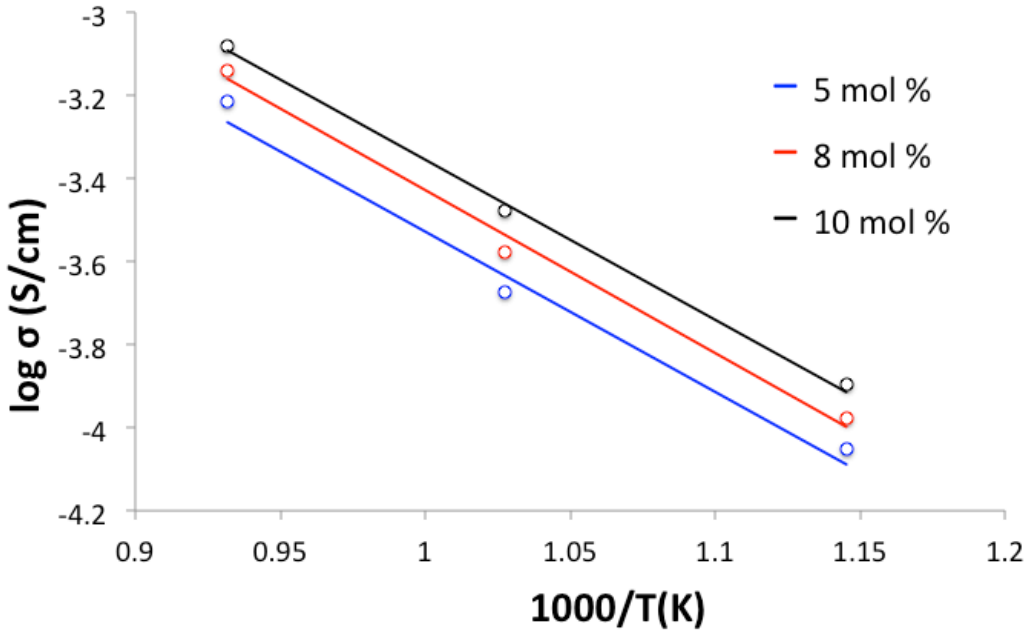

Figure 3-32 Total conductivity of $SrCe_{1-x}Ti_xO_{3-\delta}$ (x=0.05;0.08;0.1.) depend on Temperature tested in 90 sccm N_2 ; 10sccm H_2 with 3% H_2O.

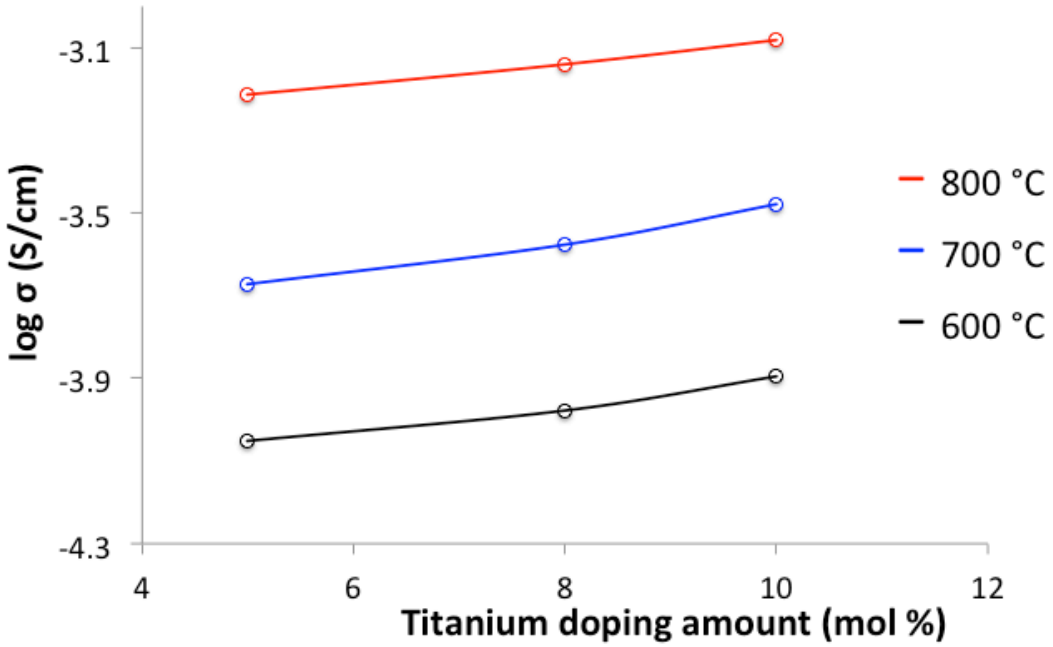

Figure 3-33 Total conductivity of $SrCe_{1-x}Ti_xO_{3-\delta}$ (x=0.05;0.08;0.1.) depend on doping amount tested in 90 sccm N_2 ; 10sccm H_2 with 3% H_2O.

Total conductivities of $SrCe_{0.92}Ti_{0.08}O_{3-\delta}$ were measured under various atmospheres (Figure 3-34). The conductivity tested in wet nitrogen is much larger than in dry nitrogen. The difference reflects high proton transfer. 10% hydrogen is supplied in the system and the conductivity is further increased. The effect of hydrogen is more significant compared to water vapor. The promising properties of proton transfer can be concluded from this figure. In this case, dry 10% hydrogen and 90% nitrogen mixture gas atmosphere and wet mixture gas environment are comparable to each other. In the oxidation gas environment, water vapor makes a significant difference. As it is shown in Figure 3-35, the existence of water vapor decreases the conductivity.

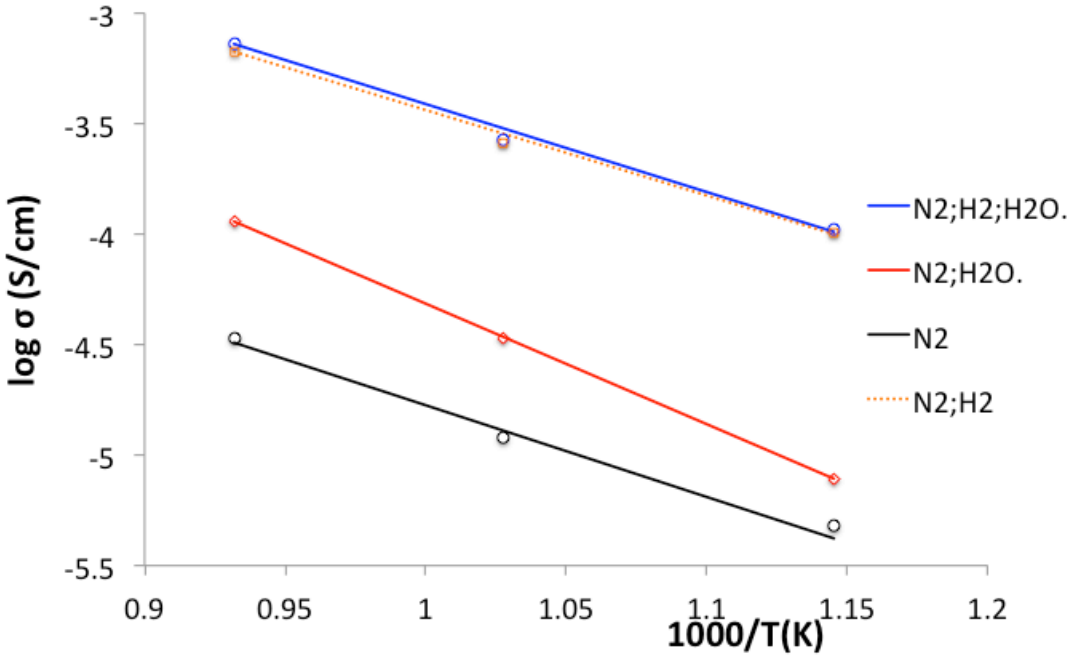

Figure 3-34 Total conductivity of $SrCe_{0.92}Ti_{0.08}O_{3-\delta}$ depend on Temperature tested in various gas environment (Test condition: 90 sccm N_2 ; 10 sccm H_2 ; 3% H_2O)

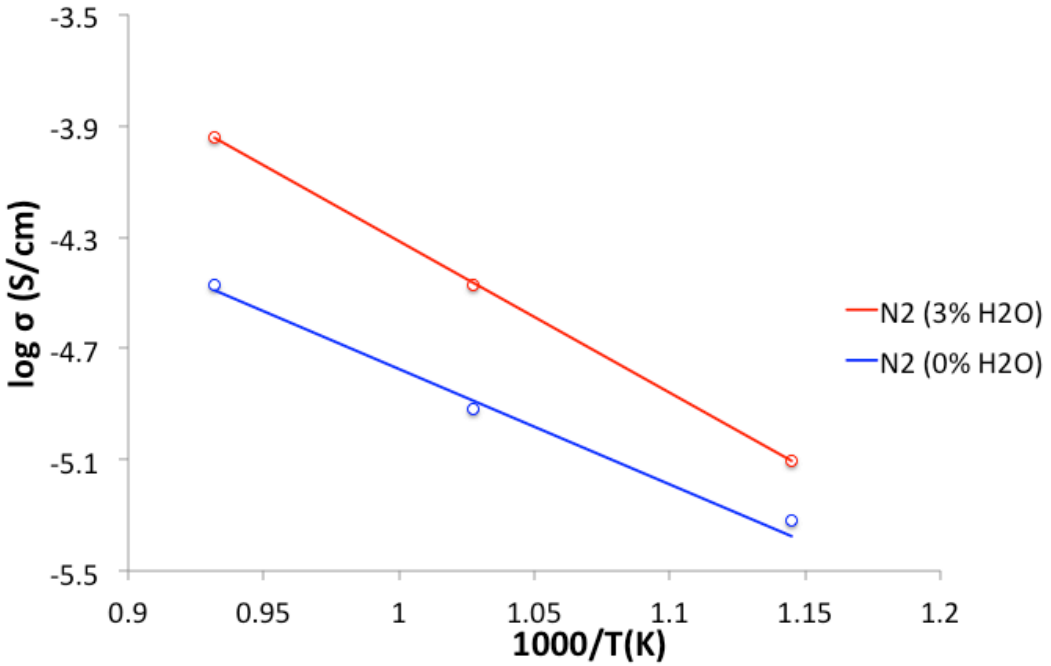

Figure 3-35 Total conductivity of $SrCe_{0.92}Ti_{0.08}O_{3-\delta}$ depend on Temperature tested in dry air and air with 3% H_2O.

Total conductivities of the chromium-doped materials are stated in Figure 3-36. The 8% dopant concentration has the maximum conductivity. 5% chromium-doped strontium cerate has the lowest conductivity. Both of the Cr-doped materials obey Arrhenius equation as a straight line is obviously observed.

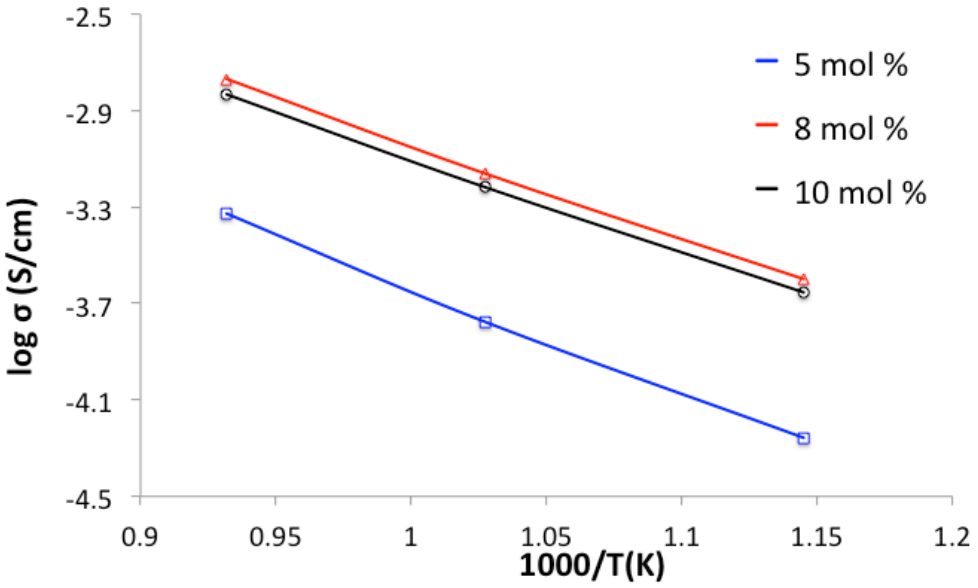

Figure 3-36 Total conductivity of $SrCe_{1-x}Cr_xO_{3-\delta}$ (x=0.05;0.08;0.1.) depend on Temperature tested in 90 sccm N_2 ; 10sccm H_2 with 3% H_2O.

The conductivity of 8% Cr-doped material is tested under various atmospheres (Figure 3-37). The conductivities under dry air and air with 3% water vapor are nearly the same. The total conductivity of the sample in nitrogen through a bubbler is much more higher than in the dry nitrogen. The proton conductivity is demonstrated by this phenomenon. Hydrogen can significantly increase the total conductivity. In air atmosphere, Cr^{3+} is oxidized to Cr^{4+} and give out an electron. The proton conductivity can be neglected. Electron conductivity dominates the total conductivity. Temperature is always an effective way to increase the total conductivity for kinetics reason. The conductivity of protons and electrons in the material is bulk-diffusion limiting as it is proofed. The maximum conductivity obtained in this new material is $10^{-2.8}$ S/cm.

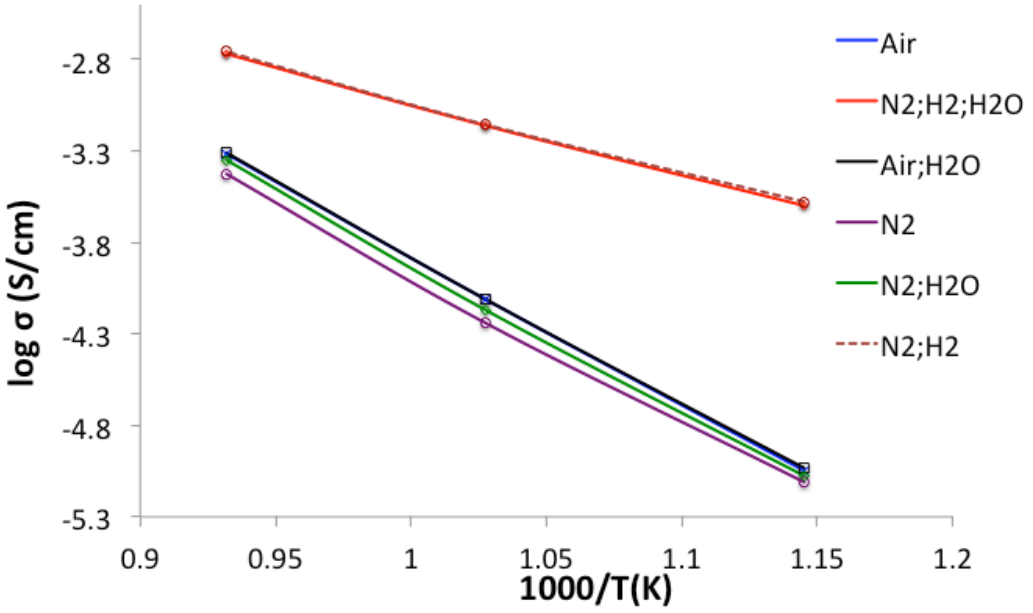

Figure 3-37 Total conductivity of $SrCe_{0.92}Cr_{0.08}O_{3-\delta}$ depend on Temperature tested in various gas environment

As $SrCe_{0.95}Pr_{0.05}O_{3-\delta}$ material has the sand-like property and hard to be sintered, the conductivity of 8%, 10% and 20% Pr-doped $SrCeO_3$ are compared in Figure 3-38 and Figure 3-39. 10% Praseodymium doped material has the highest conductivity. Large doping amount may lead the vacancies vanish by negative charge doped element. The differences between 8% doped material and 10% doped material are larger at low temperature and decrease at 800°C. Total conductivity increase with increasing temperature.

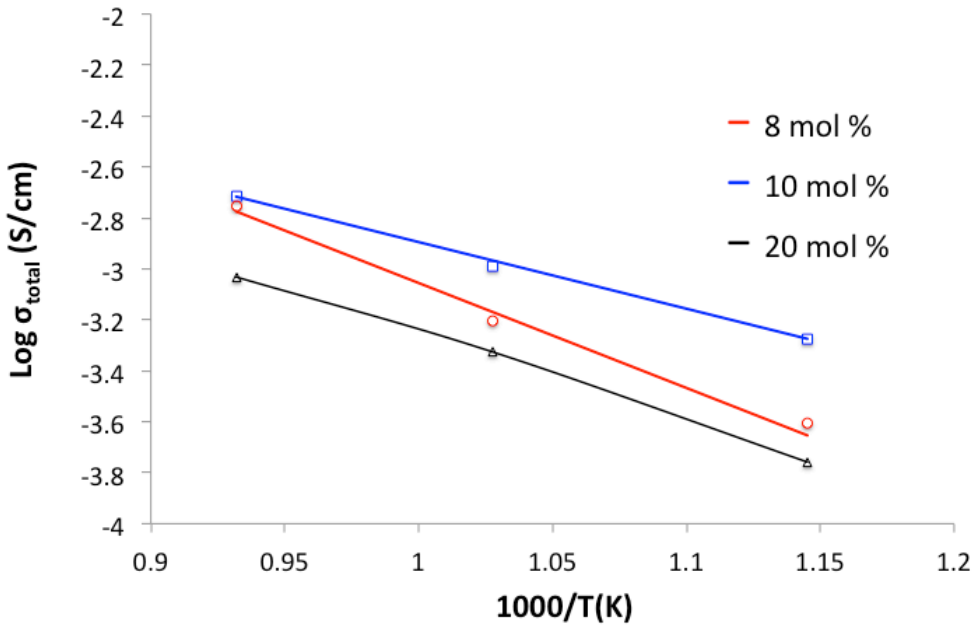

Figure 3-38 Total conductivity of $SrCe_{1-x}Pr_xO_{3-\delta}$ (x=0.08; 0.1; 0.2) depend on Temperature tested in 90 sccm N_2; 10sccm H_2 with 3% H_2O.

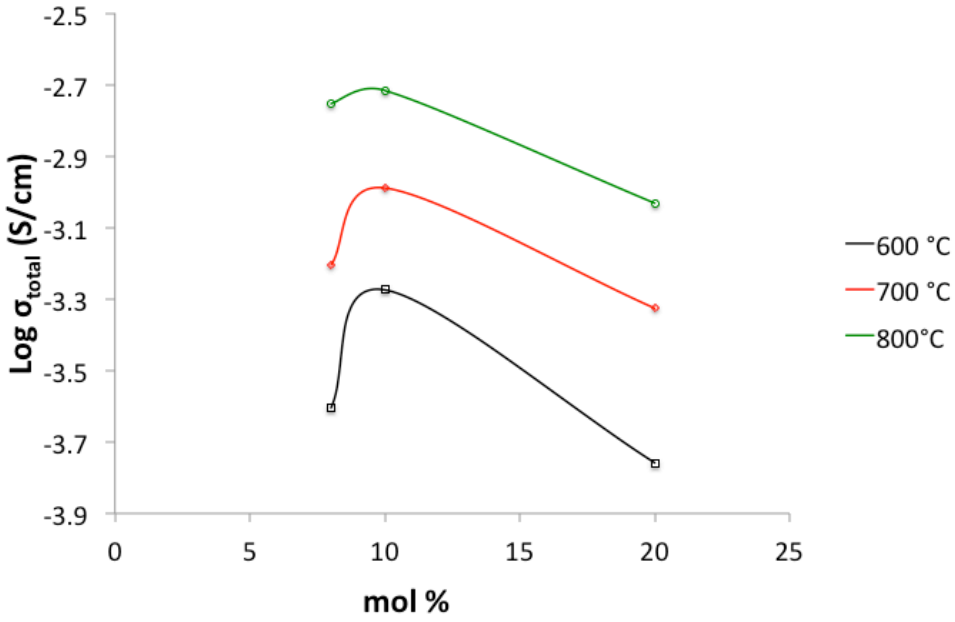

Figure 3-39 Total conductivity of $SrCe_{1-x}Pr_xO_{3-\delta}$ (x=0.08; 0.1; 0.2) depend on different doping amount

The total conductivities of $SrCe_{0.92}Pr_{0.08}O_{3-\delta}$ were measured under different gas environments (Figure 3-40). The total conductivity tested under dry air atmosphere is lower than tested in nitrogen. It is shown that the total conductivity of the material decreases with increasing partial pressure of oxygen. Therefore, the Pr doped materials are n-type conductors. Although the water vapor has unobvious effect under air atmosphere, the existence of water vapor influences the total conductivity in nitrogen. The reaction in equation (1-6) explained the increased conductivity. It is confirmed that proton conductivity is dominating in this n-type conductor. However, the proton conductivity is obviously decreased for 20% Pr doped material shown in Figure 3-41.

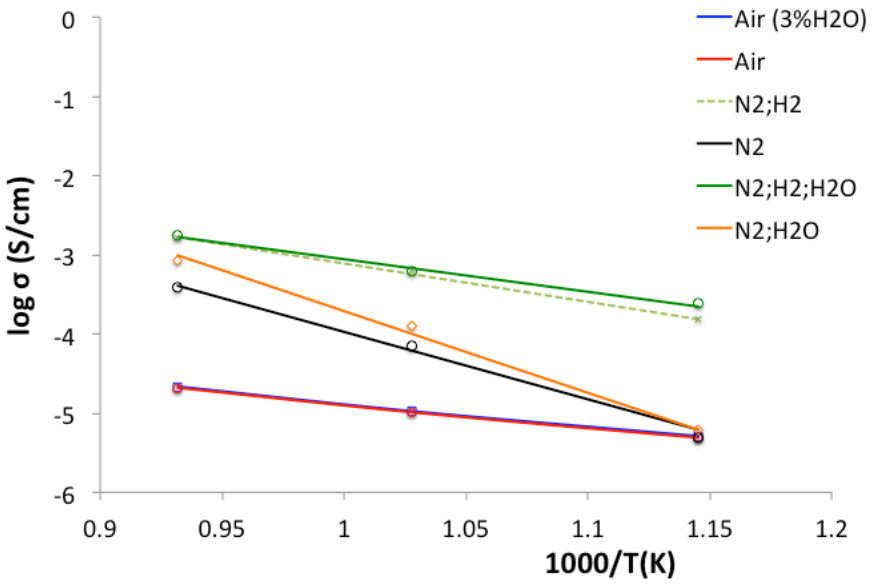

Figure 3-40 Total conductivity of $SrCe_{0.92}Pr_{0.08}O_{3-\delta}$ depend on Temperature tested in various gas environment

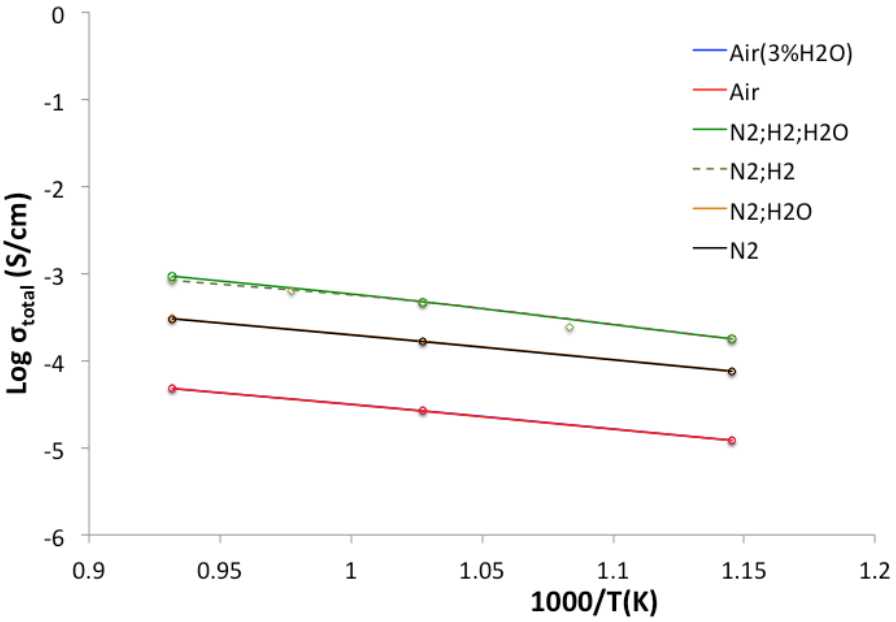

Figure 3-41 Total conductivity of $SrCe_{0.8}Pr_{0.2}O_{3-\delta}$ depend on Temperature tested in various gas environment

Total conductivity of different dopant tested in 90 sccm N_2 ; 10sccm H_2 with 3% H_2O is compared in the figure 3-42. The total conductivity of Pr-doped material is comparable to Eu-doped material. Titanium doped material has the minimum total conductivity. Cr-doped material is moderately higher than Ti-doped.

For all the new materials explored in this chapter, only Pr-doped materials have a promising potential of remaining the high proton conductivity and enhancing the electron conductivity. This Pr-doped material has been further investigated in the OCV measurement and permeation test of MIEC membrane reactor.

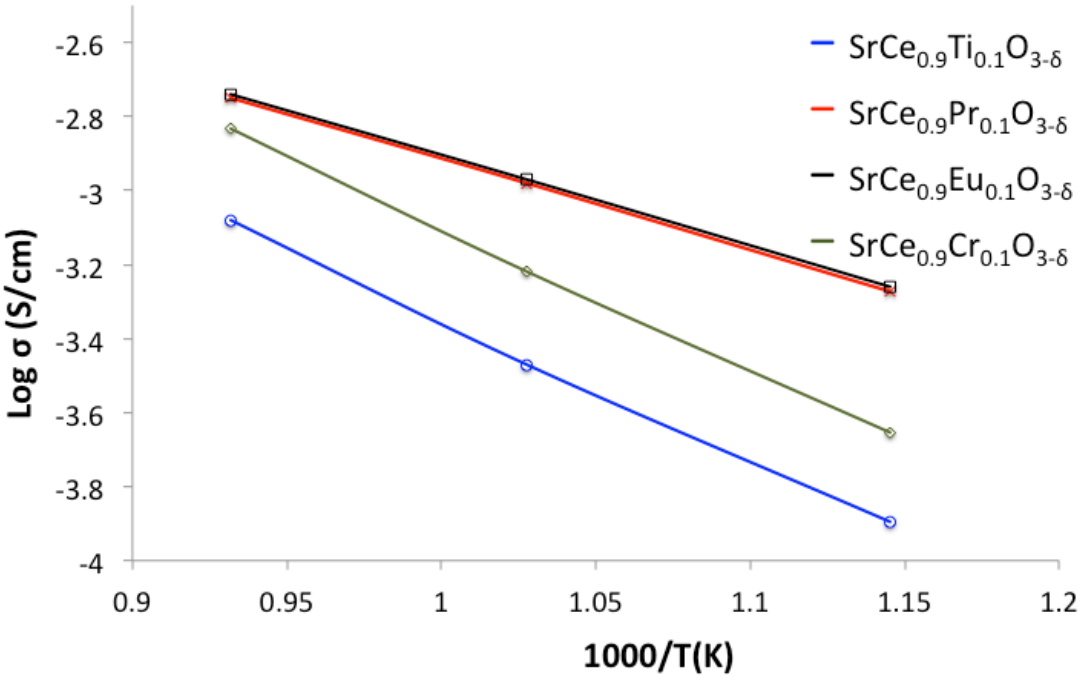

Figure 3-42 Total conductivity of different dopant tested in 90 sccm N_2 ; 10sccm H_2 with 3% H_2O

The conductivities of all the materials investigated above are summarized in Figure 3-43. Total conductivity of $SrCeO_3$ is obviously increased with various doping elements.

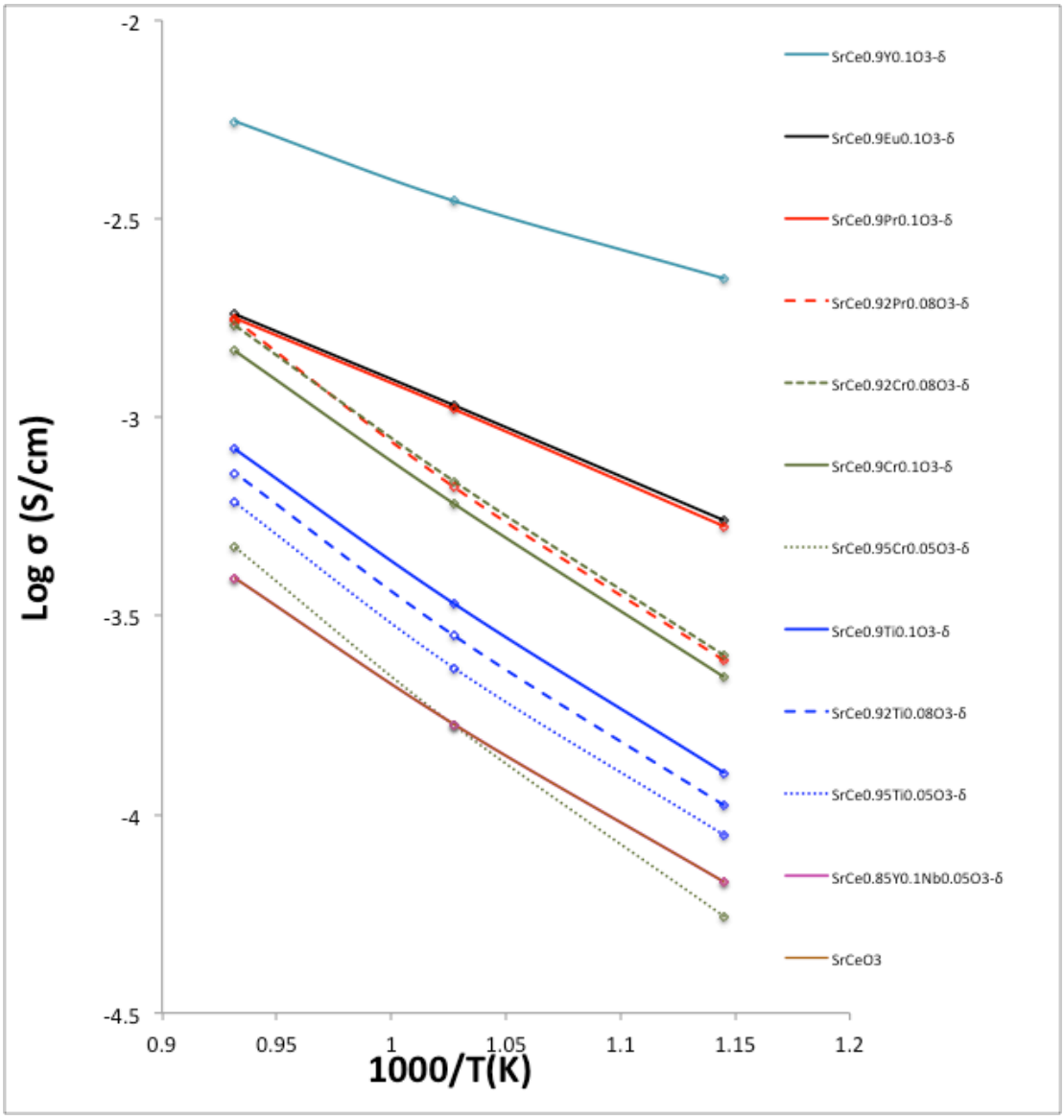

Figure 3-43 Conductivity comparison of all the materials synthesized tested in 90 sccm N_2 ; 10sccm H_2 with 3% H_2O

Chapter 4: Proton and Electron Conductivity of $SrCe_{1-x}Pr_xO_{3-\delta}$ (x=0.1, 0.15, 0.2)

For all the new materials explored in this chapter, only Pr-doped materials have comparable high conductivity to Eu-doped materials. Therefore, the electron conductivities and proton conductivities of $SrCe_{1-x}Pr_xO_{3-\delta}$ (x=0.1, 0.15, 0.2) were calculated through transference number of each species obtained from OCV measurement [36] and total conductivities measured in chapter 3. The bulk-limiting permeation flux is determined by ambipolar conductivity. Therefore, the electron conductivities and proton conductivities of $SrCe_{1-x}Pr_xO_{3-\delta}$ (x=0.1, 0.15, 0.2) were used for calculating amipolar conductivities.

4.1 OCV measurement

In order to calculate proton and electron conductivities separately, the OCV measurement was performed using the apparatus shown in Figure 4-1. $SrCe_{1-x}Pr_xO_{3-\delta}$ (x=0.1, 0.15, 0.2) powder that made by solid-state reaction was compacted into 1-inch disk, sintered at 1450°C for 4 hours, polished with 800-grit SiC paper. The thin pellet was sealed at the end of an alumina tube. Inserted the alumina tube with the sample into a quartz reactor.

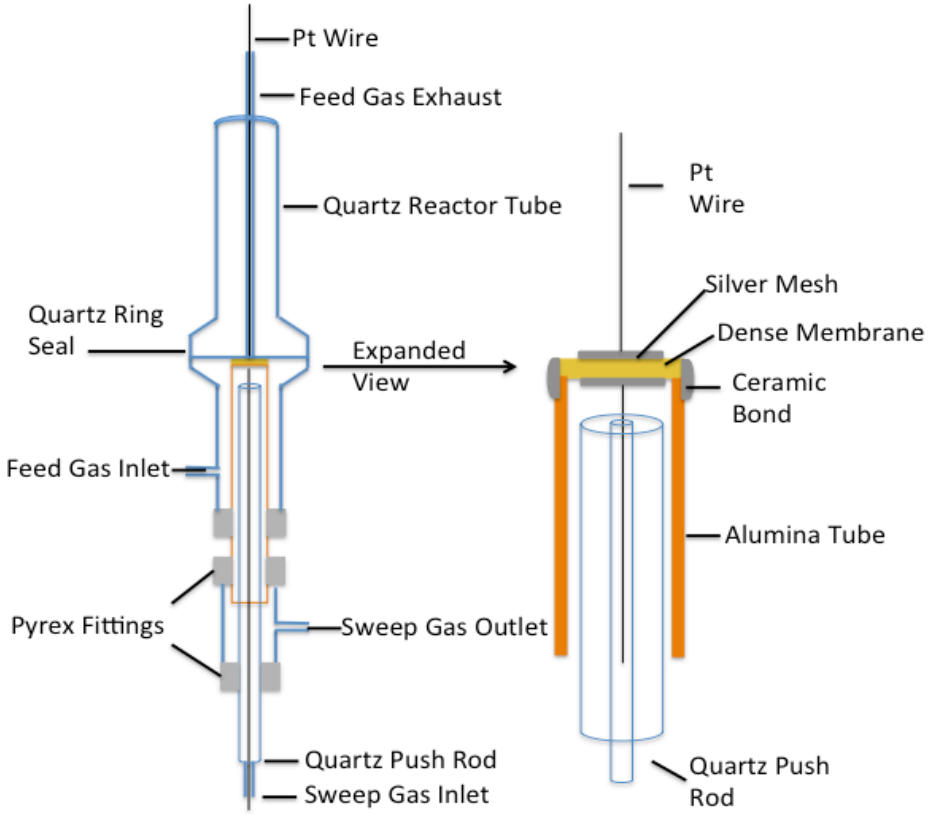

Figure 4-1 The schematic illustration of experimental setup for transference number measurement and permeation test

The apparatus, Figure 4-1, contains two different gas environments. Different concentration of hydrogen was supplied to the two sides of the sample. Multi-meter was used for measuring the open circuit potentials. Concentration cells were used to determine transference number of hydroxyl group and electrons from OCV measurements.

The OCV was measured under four conditions listed below:

1) 1, 100% H_2, Pt/$SrCe_{1-x}Pr_xO_{3-\delta}$/Pt, 5% H_2 +balance He, 2

2) 1, 50% H_2 +balance He, Pt/$SrCe_{1-x}Pr_xO_{3-\delta}$/Pt, 5% H_2 +balance He, 2

3) 1, 25% H_2 +balance He, Pt/$SrCe_{1-x}Pr_xO_{3-\delta}$/Pt, 5% H_2 +balance He, 2

4) 1, 12.5% H_2 +balance He, Pt/$SrCe_{1-x}Pr_xO_{3-\delta}$/Pt, 5% H_2 +balance He, 2

The electrolyte theoretical potential is

$$V_{oc} = \frac{RT}{2F}[-t_{ion} \ln\left(\frac{P_{H2}^2}{P_{H2}^1}\right) + t_O \ln\left(\frac{P_{H2O}^2}{P_{H2O}^1}\right)] \quad (4\text{-}1)$$

If the cell is in the dry hydrogen environment, the vapor pressure term can be neglected. The oxygen partial pressure in dry hydrogen atmosphere is around 10^{-24}-10^{-25} atm. The oxygen ion transference number can be neglected. Therefore, it is assumed that the ionic transference number equals to the proton transference number under dry hydrogen concentration cell. Based on this assumption, the theoretical potential can be calculated in equation (4-2).

$$E_{th} = -\frac{RT}{2F} \ln\left(\frac{P_{H2}^2}{P_{H2}^1}\right) \quad \text{Equation (4-2)}$$

Where F is the Faraday constant and n is the number of Faraday equivalents that flow through the cell. The experimental potential is smaller when this material has electron conductivity. Therefore, the ionic transference number can be obtained.

$$E_{exp} = t_{ion} \cdot E_{th} \quad \text{Equation (4-3)}$$

The ionic transference number is accurate when it is larger than 0.1. The electron transference number can be obtained by taking the ionic transference number from one.

4.2 Results and Analysis

In order to prove that doping Pr improved the electronic conductivity, transference number of each carrier was calculated by measuring OCV under various conditions. The dense disks used in the OCV measurements had 24mm diameter and 1.2mm

thickness. The cell was studied from 600 °C to 800 °C. Table 4-1 shows the measured OCV and electron transference number with different hydrogen chemical potential and temperature.

Table 4-1 OCV and electron transference number under different chemical potential gradient and temperature.

OCV and electron transfer-ence number		800°C				750°C				700°C				650°C				600°C			
		t_{elec}	V_{mea}	V_{th}		t_{elec}	V_{mea}	V_{th}		t_{elec}	V_{mea}	V_{th}		t_{elec}	V_{mea}	V_{th}		t_{elec}	V_{mea}	V_{th}	
Pr mol%	Case																				
10	1	0.448	76.5	138.5		0.364	84.0	132.1		0.243	95.1	125.6		0.198	95.6	119.1		0.074	104.4	112.7	
	2	0.338	70.5	106.5		0.256	75.5	101.5		0.187	78.5	96.5		0.188	74.4	91.6		0.124	75.9	86.6	
	3	0.187	60.5	74.4		0.153	60.1	70.9		0.111	60.0	67.5		0.017	62.9	64.0		0.126	52.9	60.5	
	4	0.072	39.3	42.4		0.081	37.1	40.4		0.034	37.1	38.4		0.004	36.3	36.4		0.156	29.1	34.5	
15	1	0.633	50.9	138.5		0.537	61.1	132.1		0.525	59.7	125.6		0.496	60.1	119.1		0.417	65.7	112.7	
	2	0.575	45.2	106.5		0.492	51.6	101.5		0.413	56.7	96.5		0.427	52.5	91.6		0.296	61.0	86.6	
	3	0.483	38.5	74.4		0.357	45.6	70.9		0.263	49.7	67.5		0.260	47.4	64.0		0.189	49.1	60.5	
	4	0.264	31.2	42.4		0.198	32.4	40.4		0.188	31.2	38.4		0.185	29.7	36.4		0.179	28.3	34.5	

20	1	112.7	50.0	0.556	119.1	48.3	0.595	125.6	47.4	0.623	132.1	47.7	0.639	138.5	45.0	0.675
	2	86.6	57.9	0.332	91.6	37.5	0.591	96.5	41.4	0.571	101.5	37.1	0.634	106.5	37.7	0.646
	3	60.5	46.0	0.240	64.0	27.5	0.570	67.5	31.5	0.533	70.9	32.4	0.543	74.4	30.7	0.587
	4	34.5	23.0	0.333	36.4	24.9	0.317	38.4	27.0	0.297	40.4	30.5	0.245	42.4	28.6	0.325

In Table 4-1, the ion transference number can be obtained through Equation (4-3). The sum of electron transference number and proton transference number is one based on the assumptions. Figure 4-2 shows that the electron transference number increases with increasing doping amount and temperature. This behavior is attributed to increased n-type electron conduction by the change of Pr oxidation state ($Pr^{+3} \rightarrow Pr^{+4} + e^-$). Greater hydrogen chemical potential gradients and temperature result in higher electron transference number (Figure 4-3). Larger amount of Pr dopant leads to greater electron conductivity. The electron transference number has more obvious dependence upon hydrogen chemical potential at higher temperature for 10mol% and 15mol% Pr-doped $SrCe_{1-x}Pr_xO_{3-\delta}$.

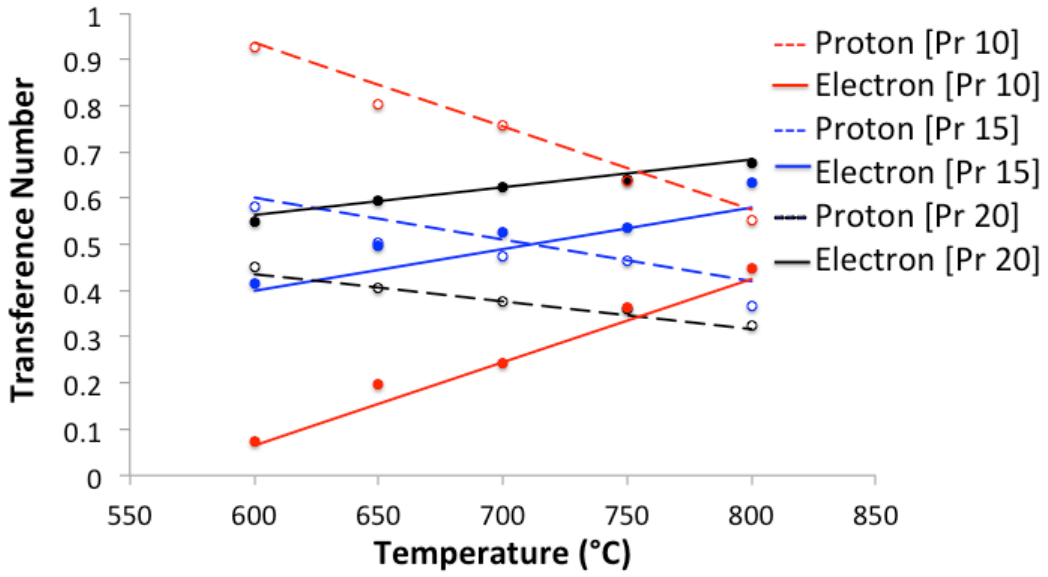

Figure 4-2 Transfer number of each species in 10 mol%, 15 mol % and 20 mol% Pr doped material tested under 100% H_2 to 5% H_2 with 95% balance air.

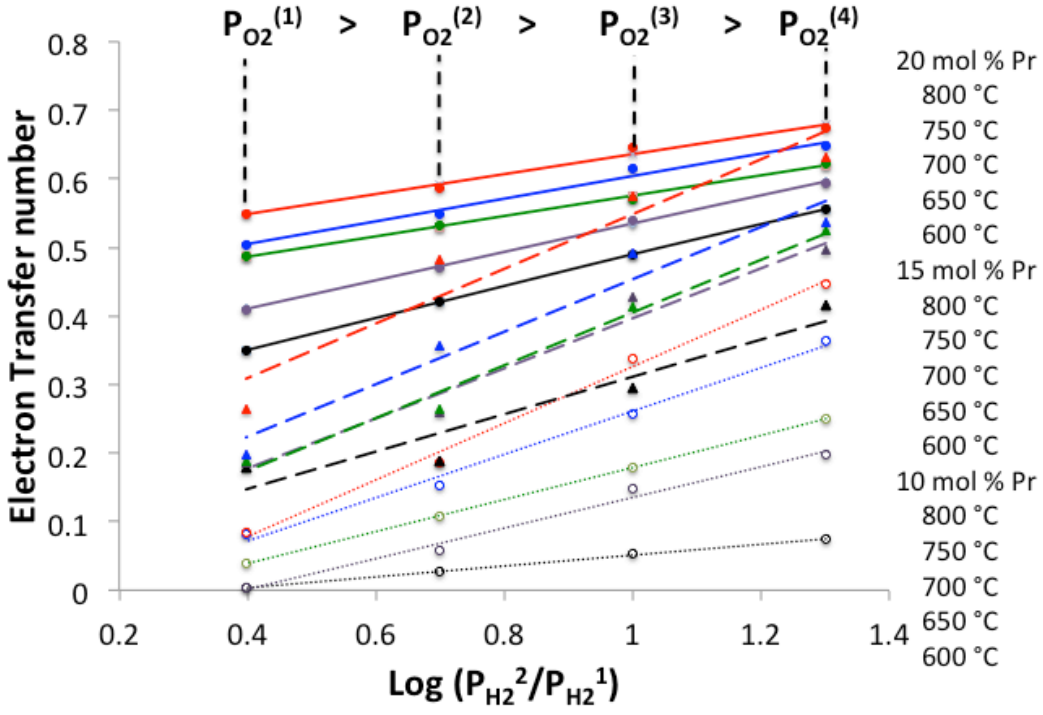

Figure 4-3 Electron transfer number of 10 mol%, 15 mol % and 20 mol% Pr doped material depend on hydrogen concentration gradient.

Proton and electron conductivities were calculated form total conductivity data and the transference number of each species for various composition and temperature. Figure 4-4 shows the proton and electron conductivity of each sample hydrogen/water vapor (3% H_2O) atmosphere. Compared to previous data [35], the electron conductivity of $SrCe_{1-x}Pr_xO_{3-\delta}$ (x=0.1, 0.15, 0.2) is higher than $SrCe_{1-x}Eu_xO_{3-\delta}$ (x=0.1, 0.15, 0.2) (Figure 4-5).

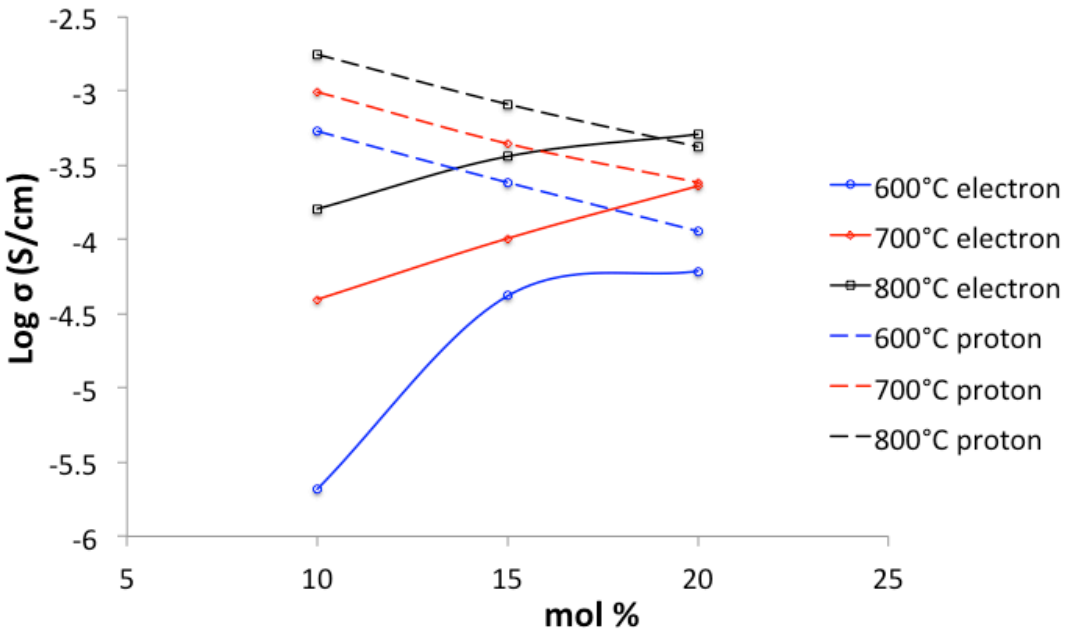

Figure 4-4 Proton and Electron conductivity of 10 mol%, 15 mol% and 20 mol% Pr doped material

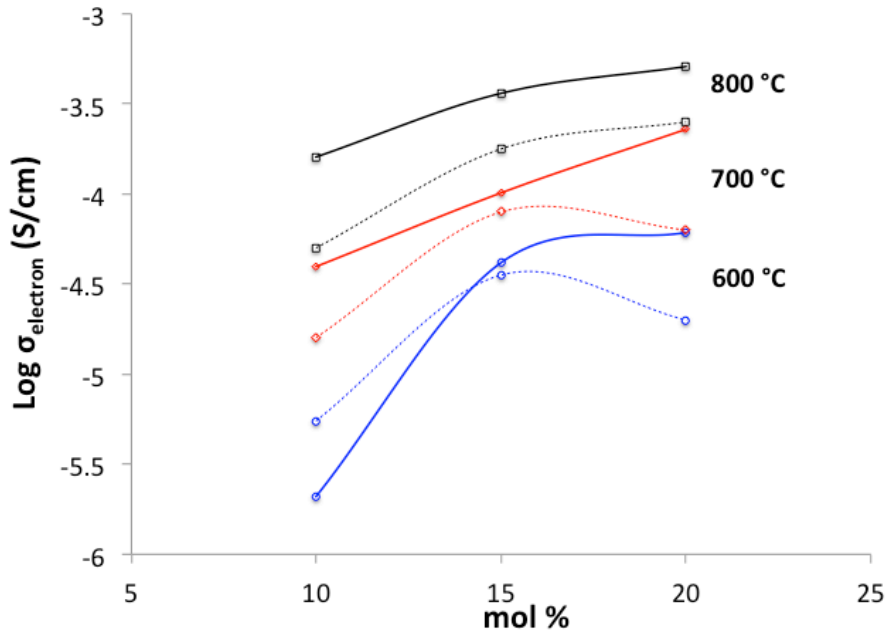

Figure 4-5 Comparison of Proton conductivity behaviors of $SrCe_{1-x}Pr_xO_{3-\delta}$ (x=0.1, 0.15, 0.2) [solid line] and $SrCe_{1-x}Eu_xO_{3-\delta}$ (x=0.1, 0.15, 0.2) [dash line] for different temperature under hydrogen/water vapor (3% H_2O) atmosphere.

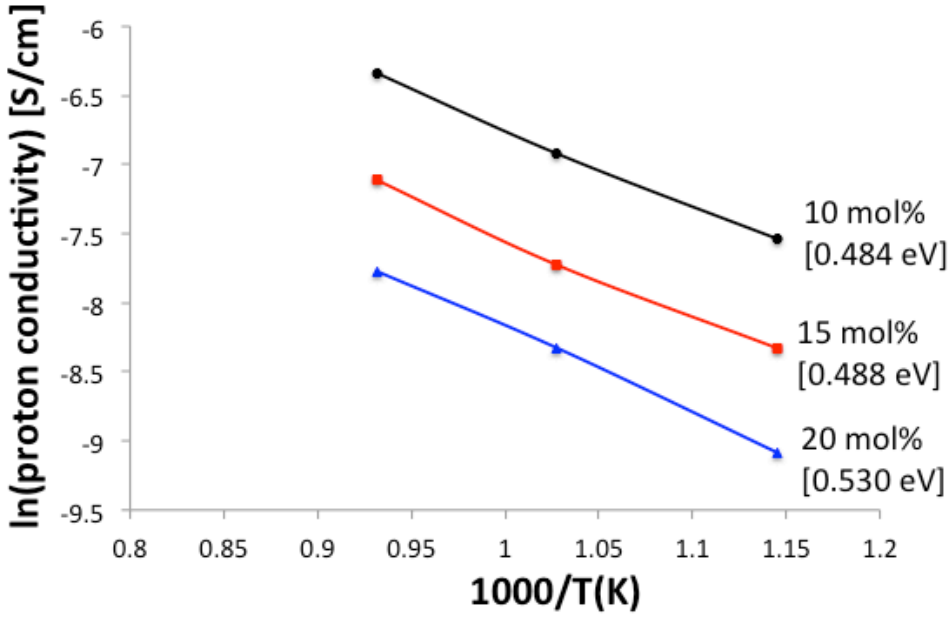

Figure 4-6 Proton conductivity of different Pr-doped material between 600°C and 800°C under hydrogen atmosphere

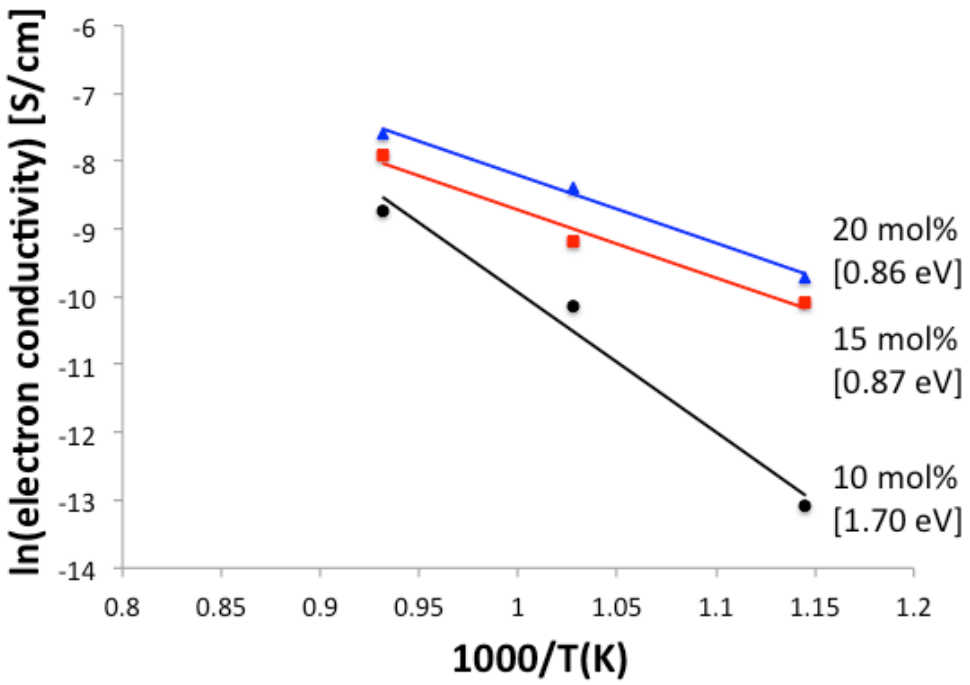

Figure 4-7 Electron conductivity of different Pr-doped material between 600°C and 800°C under hydrogen atmosphere

Figure 4-6 and 4-7 show that the both the electron and proton conductivities increase with temperature. Electron conductivities increase with increasing Pr concentration. However Proton conductivities decrease when doping more Pr into the material. The activation energies for electron conductivities are higher than proton conductivities. The activation energy for proton conductivity is approximately the same (0.48eV). However, 20 mol% Pr-doped material has higher activation energy (0.53eV) than other materials.

Based on the proton and electron conductivities, ambipolar conductivity was calculated through Euqation 4-4 and 4-5.

$$\sigma_{amb} = \frac{\sigma_{OH_O^{\cdot}}\sigma_{e^-}}{\sigma_{OH_O^{\cdot}}+\sigma_{e^-}} \qquad \text{Equation (4-4)}$$

$$\sigma_i = \sigma_{total} \times t_i \qquad \text{Equation (4-5)}$$

As it is shown in Figure 4-8, the ambipolar conductivity increases with temperature and Pr doping amount. The highest permeated hydrogen flux is proposed at 800 °C for 20mol % Pr doped material according to the ambipolar conductivity.

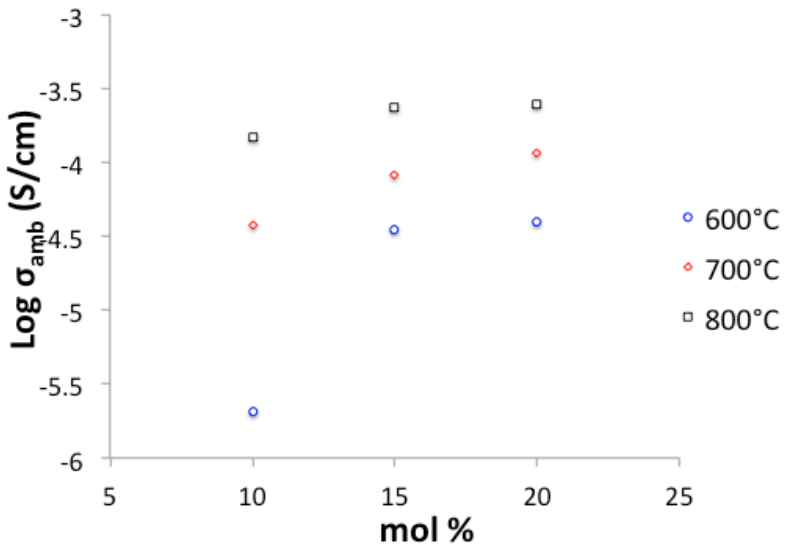

Figure 4-8 Ambipolar conductivity of 10 mol%, 15 mol% and 20 mol% Pr doped material

Chapter 5: Hydrogen Permeability of $SrCe_{1-x}Pr_xO_{3-\delta}$ (x=0.1, 0.2)

The hydrogen permeation fluxes through Pr-doped materials are determined by the ambipolar conductivities. The hydrogen permeation tests through 1.2mm thickness membranes were used to check the ambipolar conductivity results in chapter 4.

5.1 Hydrogen Permeation test

Hydrogen permeation tests were committed in the same reactor (Figure 4-1). The disks sintered by $SrCe_{1-x}Pr_xO_{3-\delta}$ (x=0.1, 0.15, 0.2) powder were sealed with ceramic bond to alumina tubes. The feed gas flows were 70sccm H_2/He mixtures. The sweep side flow was a constant 70sccm of Nitrogen. The sweep gas was analyzed with Q100MS Dycor Quadlink Mass spectrometer. The permeated hydrogen fluxes through materials $SrCe_{0.9}Pr_{0.1}O_{3-\delta}$ and $SrCe_{0.8}Pr_{0.2}O_{3-\delta}$ were measured from 650 °C to 850 °C. Measuring the helium tracer in the permeated stream checked leakage of gas through the membrane or the seal.

5.2 Results and Analysis

The hydrogen permeability through the 24mm diameter and 1.2mm thickness membrane was investigated. Figure 5-1 shows that the permeated hydrogen fluxes for 10 mol% Pr-doped $SrCeO_{3-\delta}$ increase with temperature for both dry hydrogen and hydrogen/water vapor condition. The permeated hydrogen fluxes are lower under hydrogen/water vapor condition for the reason that partial pressure of oxygen is higher when water vapor exists. The oxygen ion transference decreases the proton transference number. The permeated hydrogen fluxes increase linearly with temperature under hydrogen/water vapor condition.

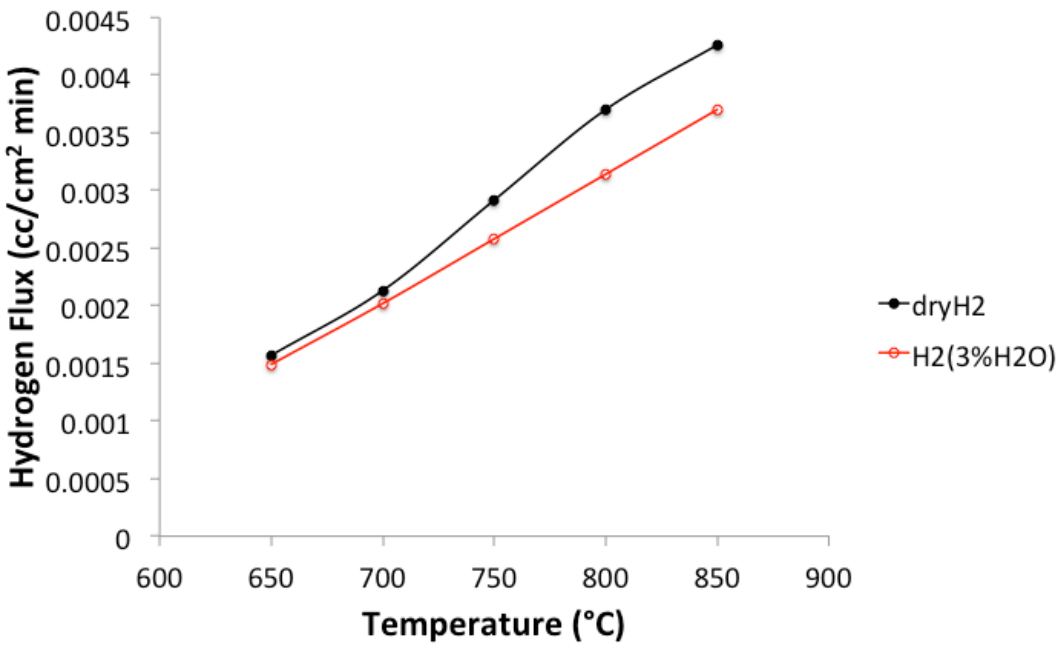

Figure 5-1 Hydrogen flux as a function of temperature for 10 mol% Pr-doped $SrCeO_{3-\delta}$: closed symbols=100% H_2; dry and open symbols: P_{H2}=0.97atm, P_{H2O}=0.03atm.

Figure 5-2 shows that hydrogen Flux for 10 mol% Pr-doped $SrCeO_{3-\delta}$ increases with increasing applied hydrogen chemical potential gradients at 850 °C. The existent of water vapor decrease the permeated hydrogen flux as it is increasing the partial pressure of oxygen. The hydrogen permeation through the disk was measured under various temperature and gas atmosphere (Figure 5-3 and Figure 5-4). The maximum permeated hydrogen flux was 0.0043 cc/cm^2 min at 850 °C for 10 mol% Pr-doped $SrCeO_{3-\delta}$ under dry hydrogen atmosphere.

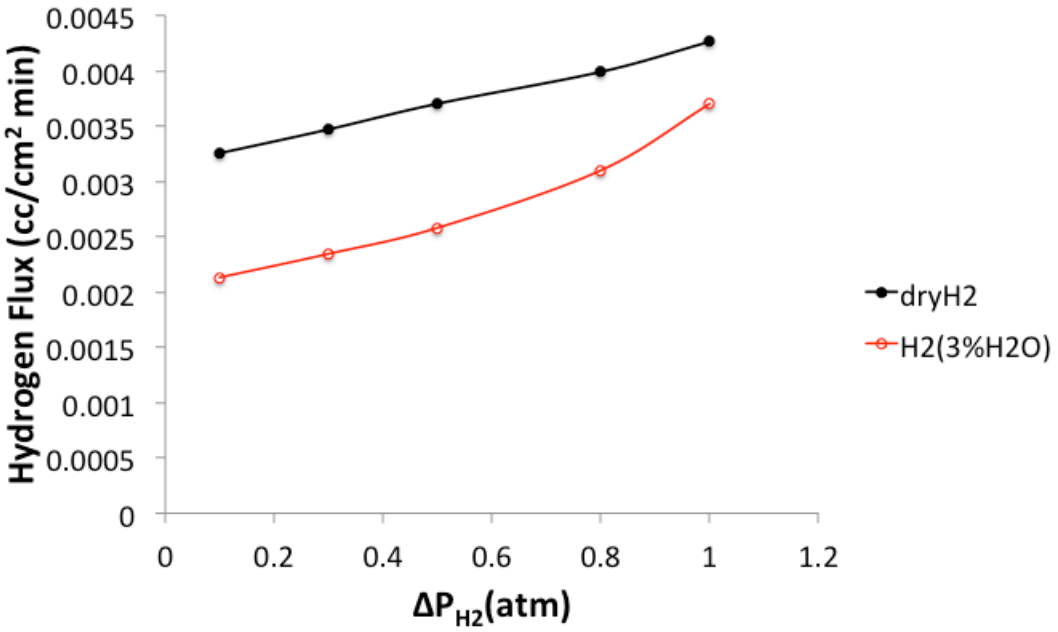

Figure 5-2 Hydrogen Flux as a function of applied hydrogen chemical potential gradients at 850 °C

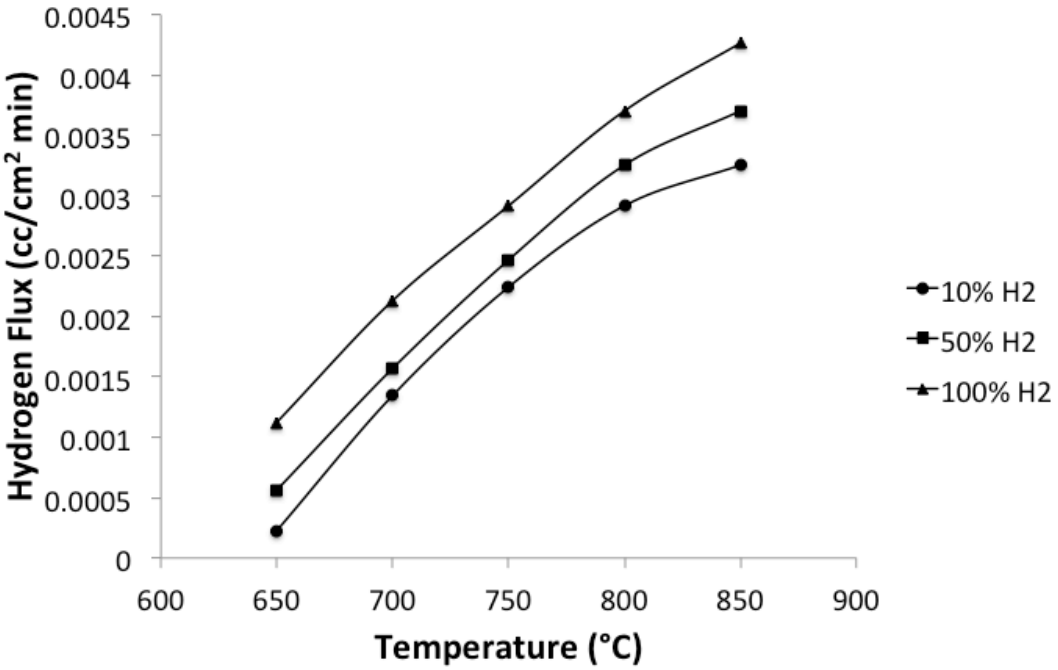

Figure 5-3 Hydrogen Flux of $SrCe_{0.9}Pr_{0.1}O_{3-\delta}$ as a function of temperature under dry condition

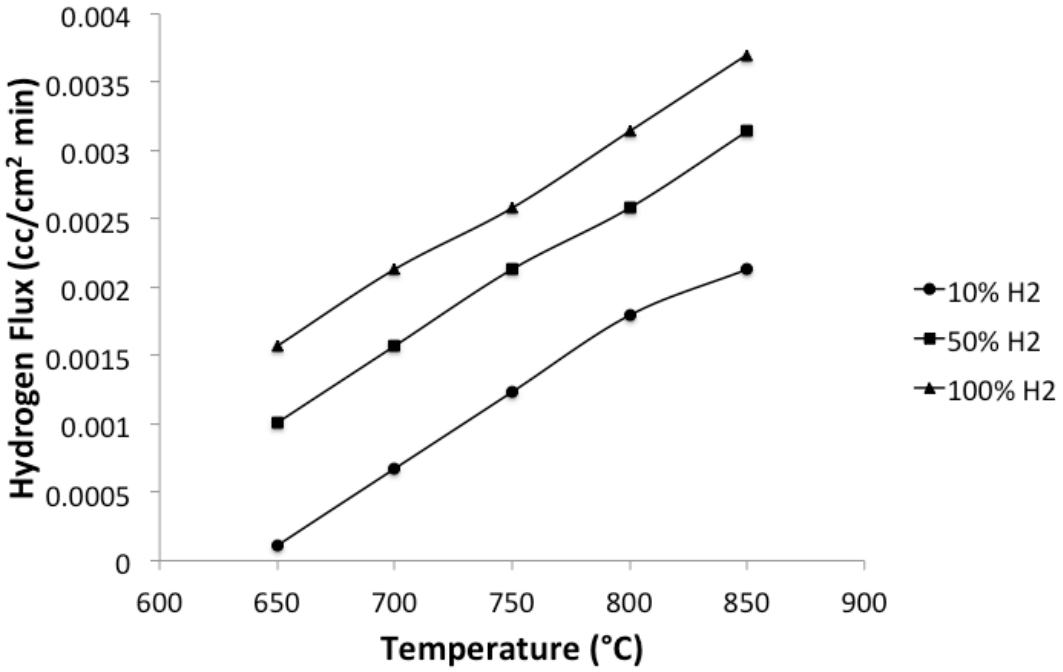

Figure 5-4 Hydrogen Flux of $SrCe_{0.9}Pr_{0.1}O_{3-\delta}$ as a function of temperature under P_{H2O}=0.03 atm

Figure 5-5 shows the hydrogen fluxes as a function of temperature for 20 mol% Pr-doped $SrCeO_{3-\delta}$ under dry hydrogen and hydrogen/water vapor conditions. There is a permeation peak observed at 800 °C. The water vapor has effect in decreasing the hydrogen permeation. However, the maximum of hydrogen permeation under hydrogen/water vapor condition is also at 800 °C. The maximum hydrogen permeation per unit area is 0.12cc/cm^2 min for 20 mol% Pr-doped $SrCeO_{3-\delta}$. Figure 5-6 shows that hydrogen Flux for 20 mol% Pr-doped $SrCeO_{3-\delta}$ increases with increasing applied hydrogen chemical potential gradients at 850 °C. The existent of water vapor decrease the permeated hydrogen flux as it is increasing the partial pressure of oxygen.

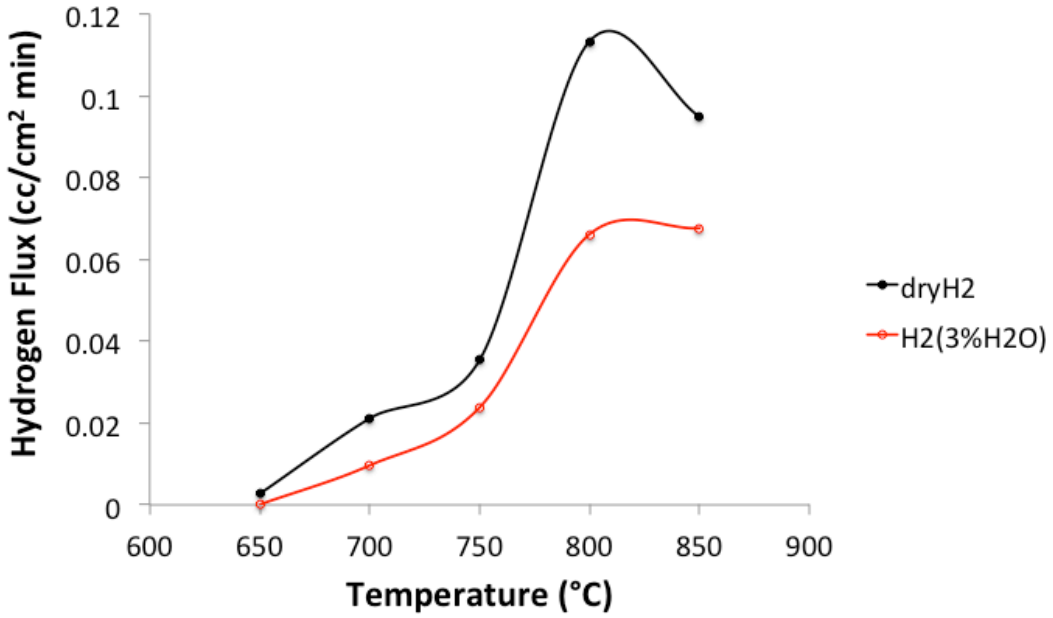

Figure 5-5 Hydrogen flux as a function of temperature for 20 mol% Pr-doped $SrCeO_{3-\delta}$: closed symbols=100% H_2; dry and open symbols: P_{H2}=0.97atm, P_{H2O}=0.03atm.

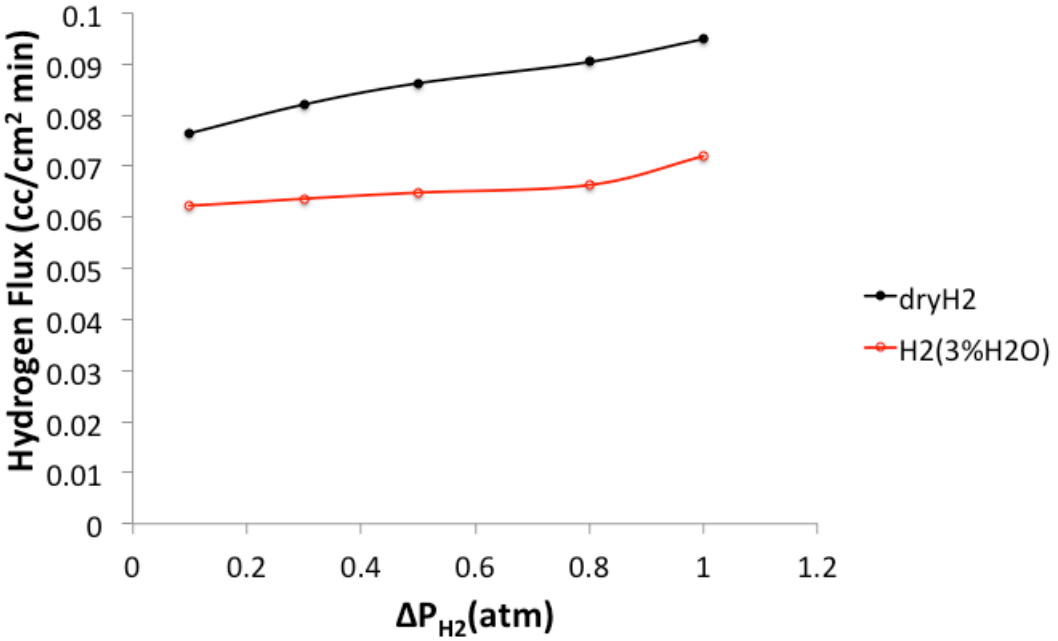

Figure 5-6 Hydrogen Flux as a function of applied hydrogen chemical potential gradients at 850 °C

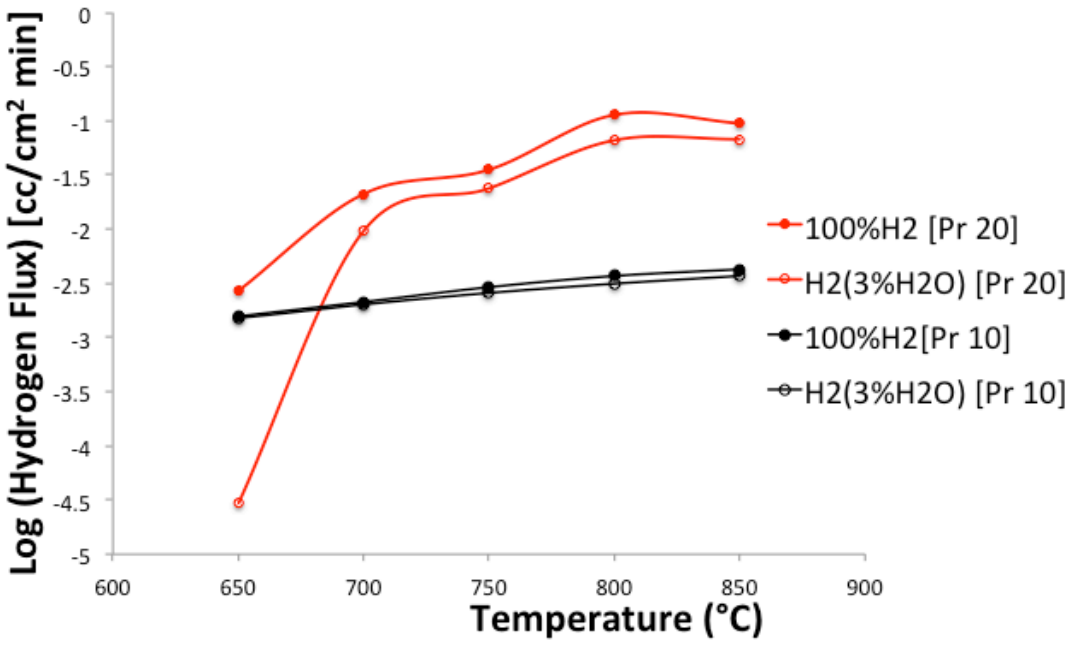

Figure 5-7 Comparison of $SrCe_{0.9}Pr_{0.1}O_{3-\delta}$ and $SrCe_{0.8}Pr_{0.2}O_{3-\delta}$ hydrogen permeation

The comparison of the hydrogen permeation for different composition at various temperature shows that the highest permeation occurs when the proton conductivity equals the electron conductivity that match the results of OCV test. It is concluded that doping Pr into $SrCeO_{3-\delta}$ highly increased the electron conductivity. Therefore, Pr-doped material is a promising substitution of the widely used Eu-doped membrane material.

To validate the results, the hydrogen permeation fluxes were calculated from the ambipolar conductivity and compared with the fluxes tested through experiment. The assumption that the bulk diffusion is rate limiting was made in order to apply Wagner equation. The permeated hydrogen fluxes were calculated under the first condition [100% H_2, Pt/membrane/Pt, 5%H_2] for 1.2mm membrane. Equation (1-4) can be simplified to Equation (5-1) under the negligible oxygen conduction condition.

$$J_{OH_O^{\cdot}} = -\frac{1}{L}\left[\frac{RT}{2F^2}\int_{P'_{H2}}^{P''_{H2}} \sigma_{amb}\, dlnP_{H_2}\right] \qquad \text{Equation (5-1)}$$

The ambipolar conductivity is a function of hydrogen and temperature. From Figure 3-41, the conductivity in hydrogen is higher than in nitrogen. The conductivity is even smaller under air condition. As the lack of data for relationship between ambipolar conductivity and hydrogen gradient, the ambipolar conductivity measured under specific condition was treated as constant. Therefore, the Equation can be further simplified to Equation (5-2).

$$J_{OH_O^{\cdot}} = -\frac{1}{L}\left[\frac{RT}{2F^2}\sigma_{amb}\ln\left(\frac{P''_{H2}}{P'_{H2}}\right)\right] \qquad \text{Equation (5-1)}$$

Substitute the constant parameters and calculated the permeated fluxes in Table 5-1.

Table 5-1 Calculated hydrogen permeation flux under [100% H_2, Pt/membrane/Pt, 5%H_2] between 600°C and 800°C (L=1.2mm thick).

	T (K)	Total Conductivity (S/cm)	Transference Number of Electrons	Hydrogen Flux of 1.2mm membrane (mol/min cm^2)
10% Pr-doped	873.15	0.00053174	0.0039	2.01E-09
	973.15	0.00102565	0.0384	4.11E-08
	1073.15	0.00192221	0.0834	1.76E-07
20% Pr-doped	873.15	0.00017624	0.35	3.85E-08
	973.15	0.00047206	0.486	1.28E-07
	1073.15	0.00083349	0.548	2.76E-07

The calculated hydrogen fluxes were assumed to be ideal gas and change units through ideal gas law. Figure 5-8 shows the Permeated hydrogen flux of $SrCe_{0.9}Pr_{0.1}O_{3-\delta}$ and $SrCe_{0.8}Pr_{0.2}O_{3-\delta}$ membranes (1.2mm) based on calculation and its comparison to measurement results. The results Pr-doped materials are very close, especially at low temperature, thus validating the use of these ambipolar conductivity results to calculate hydrogen flux. The assumptions used in calculation steps result in the difference at high temperature. The ambipolar conductivity is dependent on partial pressure of hydrogen and temperature. The ambipolar conductivity was considered as a constant for simple calculation. The calculated values will be more close to the experiment when this variation is concluded.

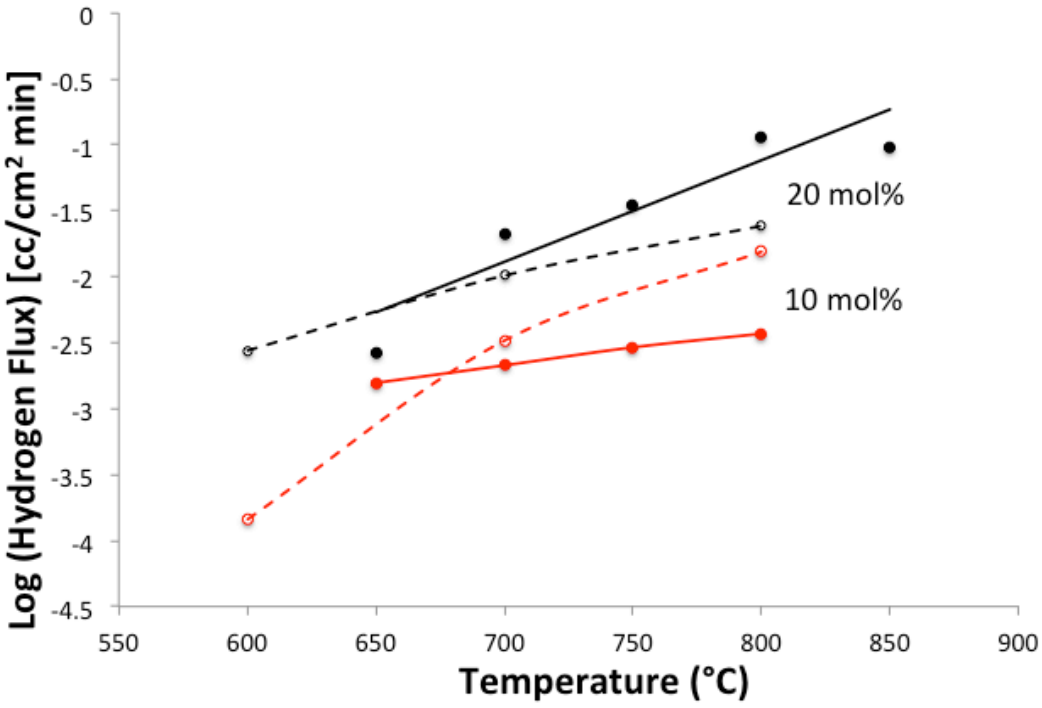

Figure 5-8 Permeated hydrogen flux of $SrCe_{0.9}Pr_{0.1}O_{3-\delta}$ and $SrCe_{0.8}Pr_{0.2}O_{3-\delta}$ membranes (1.2mm) based on calculation using Wagner equation (dash line) and experiment under pure hydrogen atmosphere on the feed side (solid line)

Chapter 6: Application of $SrCe_{0.9}Pr_{0.1}O_{3-\delta}$ in Tubular Membrane Reactors

Advanced membrane reactor is a mixed protonic-electronic conducting membrane coated on porous support material, which has the ability of separating the hydrogen gas from complicated gas mixture. $SrCe_{0.9}Eu_{0.1}O_{3-\delta}$ was used as dense membranes in the tubular reactors. In this chapter, $SrCe_{0.9}Eu_{0.1}O_{3-\delta}$ membrane reactors were successfully re-fabricated and the permeations of hydrogen were measured.
In order to improve hydrogen transfer efficiency, $SrCe_{0.9}Pr_{0.1}O_{3-\delta}$ membrane reactors were fabricated. But the fabrication of the $SrCe_{0.9}Pr_{0.1}O_{3-\delta}$ membrane reactors needs further improvement.

6.1 Introduction

Advanced Membrane Reactors were fabricated with tubular NiO-$SrCeO_3$ support coated with thin-film $SrCe_{0.9}Eu_{0.1}O_{3-\delta}$ inside by colloidal coating method [37]. This tubular membrane reactor can selectively transfer proton and electron that can be used in hydrogen separation and purification [38]. The advance membrane reactor with proton transfer membrane can be used for separating the hydrogen from the gas mixtures [39,44,50]. The in-situ extraction of the hydrogen from the mixer can improve the chemical yields by shifting the equilibrium balance towards the production according to Le Chatelier's principle [40,42]. In addition, the proton transfer membrane reactor can subsequently convert effluent syngas mixture to chemical feedstocks and liquid fuels by Fischer–Tropsch catalysis [43].

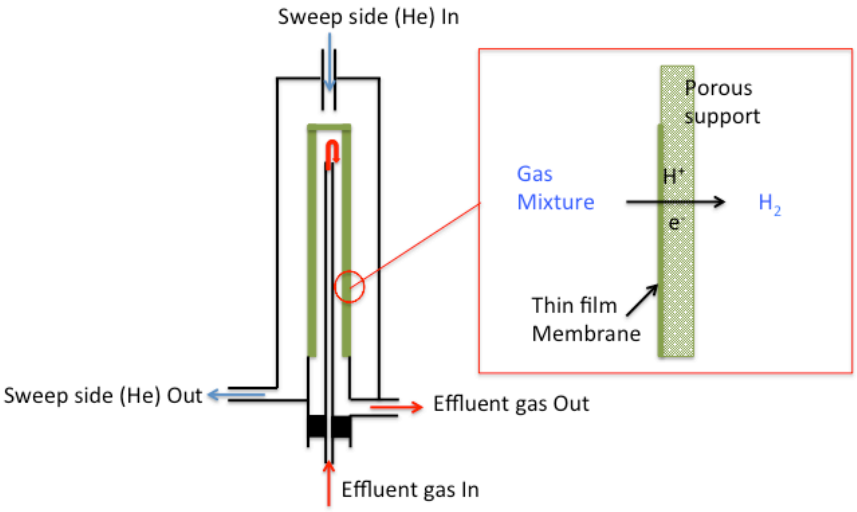

Figure 6-1 The schematic of the advanced membrane reactor used in effluent gas separation

In previous chapter, it is demonstrated that $SrCe_{0.9}Pr_{0.1}O_{3-\delta}$ has higher electron conductivity than $SrCe_{0.9}Eu_{0.1}O_{3-\delta}$. Therefore, $SrCe_{0.9}Pr_{0.1}O_{3-\delta}$ was used as the new dense membrane for hydrogen separation. The hydrogen flux will be increased by decreasing the membrane thickness because it reducing the bulk diffusion limitation.

6.2 Fabrication of Membrane reactor

The porous support was made of $SrCeO_3$ with pore former NiO (J. T. Baker). $SrCeO_3$ power that synthesized through conventional solid-state method previously was ball-milled with NiO (99%, Alfa Aesar) at the ratio of 30 wt% NiO to 70 wt% $SrCeO_3$. Toluene and ethanol (1:1) mixture was used as solvent and fish oil as dispersant in making slurry for tape casting. After ball mill the powder with fish oil and solvent for 24 hours, the binder Polyvinyl Butyral (PVB) and Butyl Benzyl Phthalate (BBP) was added and ball mill for 24 hours. The slurry was used for tape cast and the green tape was dried for at least 12 hours. The tape was cut into 8 inches long and 3.25 to 3.5

inches wide depend on the thickness of the tape. ¼ -in diameter steel rod was used to roll the tape and a cap was added to make a tube. The slurry before tape casting was used for further sealing the cap in order to prevent leakage. The tube made was soft for the reason that it contains certain amount of solvent. The tube was dried in air at room temperature for 24 hours before pre-sinter process. And sinter the tube at 1050 °C for 4 hours with a slow ramp rate.

The membrane material $SrCe_{0.9}Eu_{0.1}O_{3-\delta}$ (ESC) was synthesized by sol-gel method. $Ce(NO_3)_3 \bullet 6H_2O$ (99.5%, Alfa Aesar), $Sr(NO_3)_2$ (99.97%, Alfa Aesar) and $Eu(NO_3)_3 \bullet 6H_2O$ (99.9% Alfa Aesar) was dissolved with water in the desired stoichiometry ratio at room temperature. Citric acid and Ethylene was added in to the solution and totally dissolved at 80°C. The molar ratio of the nitrates to citric acid and ethylene glycol was 1:2:2. The solution was heated up to 350 °C slowly and evaporating till yellow sol-gel. Continue supplying heat until the gel turned to black solid. The black powder was grinded 24 hours and calcined at 1100 °C for 4 hours. XRD was used to determine the phase structure of the material synthesized. Ball-mill the product for 24 hours before use.

The thermal expansion rates of membrane and support are different which will cause membrane cracking at high temperature. Europium doped strontium cerate powder synthesized above was used to make a buffer layer for protecting the membrane from cracking. 30 wt% NiO and 70 wt% ESC powder was ball milled for 48 hours in Ethanol. ESL 441 (Electroscience) was added and mixed multiple times until solvent

evaporates and uniform paste remains. Dissolve the paste at the ratio ESC-NiO powder: Ethanol : ESL441 = 1:4:1. The colloidal solution is coated inside the tube 2 times and forms a thin buffer layer. Pre-sinter the tube at 1050 °C for 4 hours after coating the buffer layer.

ECS colloidal was made in similar process. The ECS powder is ball-milled in ethanol for 48 hours after calcination. ESL 441 was used in making the paste. Colloidal solution was obtained by dissolving the paste at the ratio ESC-NiO powder: Ethanol: ESL441 = 1:4:1. The colloidal was mixed in the ball-mill bottle without adding ball media for at least 2 hours before coating. Colloidal coating inside the tube formed thin membrane. The coated tube was dried for 24 hours and sinter at 1400 °C for 4 hours.

10% Praseodymium doped $SrCeO_3$ membrane materials was synthesized by sol-gel method using $Ce(NO_3)_3 \bullet 6H_2O$ (99.5%, Alfa Aesar), $Sr(NO_3)_2$ (99.97%, Alfa Aesar) and $Pr(NO_3)_3 \bullet 6H_2O$ (99.9% Alfa Aesar). The molar ratio of the nitrates to citric acid and ethylene glycol was 1:2:2. The remaining solid was ball-milled and calcined at 1100°C for 4 hours. XRD was measured to determine the phase structure. The Pr-doped powder synthesized through sol-gel method was made to paste and colloidal for coating the tubular membrane inside the support. The tube was sintered at 1450°C for 4 hours. SEM tests (Nanoscale Imaging, Spectroscopy, and Properties Laboratory, University of Maryland-College Park) were committed for showing the dense membrane surface and the thickness of the surface.

The 10ESC/NiO–$SrCeO_3$ tubular hydrogen membrane cell and 10PrSC/NiO-$SrCeO_3$ was placed in a quartz tube reactor in order to measure the leakage level and hydrogen permeation of the membrane. H_2 balanced with Ar was made to flow to the outer (feed) side while He was made to flow to the inner sweep side of the cell. The concentrations of permeated gases on the (sweep) side were measured using a Q100MS Dycor QuadLink mass-spectrometer (Ametek, Paoli, PA).

6.3 Results and Analysis

The support material $SrCeO_3$ was synthesized through conventional solid-state method. XRD patterns of $SrCeO_3$ shown in Figure 6-2 confirmed its purity with the identical peaks. The membrane material $SrCe_{0.9}Eu_{0.1}O_{3-\delta}$ was synthesized through sol-gel method. It is demonstrated that the calcination temperature 900 °C is not high enough for obtaining pure phase. Additional 1100 °C calcination make the majority of the material $SrCe_{0.9}Eu_{0.1}O_{3-\delta}$. However, the impurities may affect the performance. New batch of material is highly recommended. It was also demonstrated that the calcination temperature above 950 °C could lead to $SrCe_{0.9}Eu_{0.1}O_{3-\delta}$ pure material.

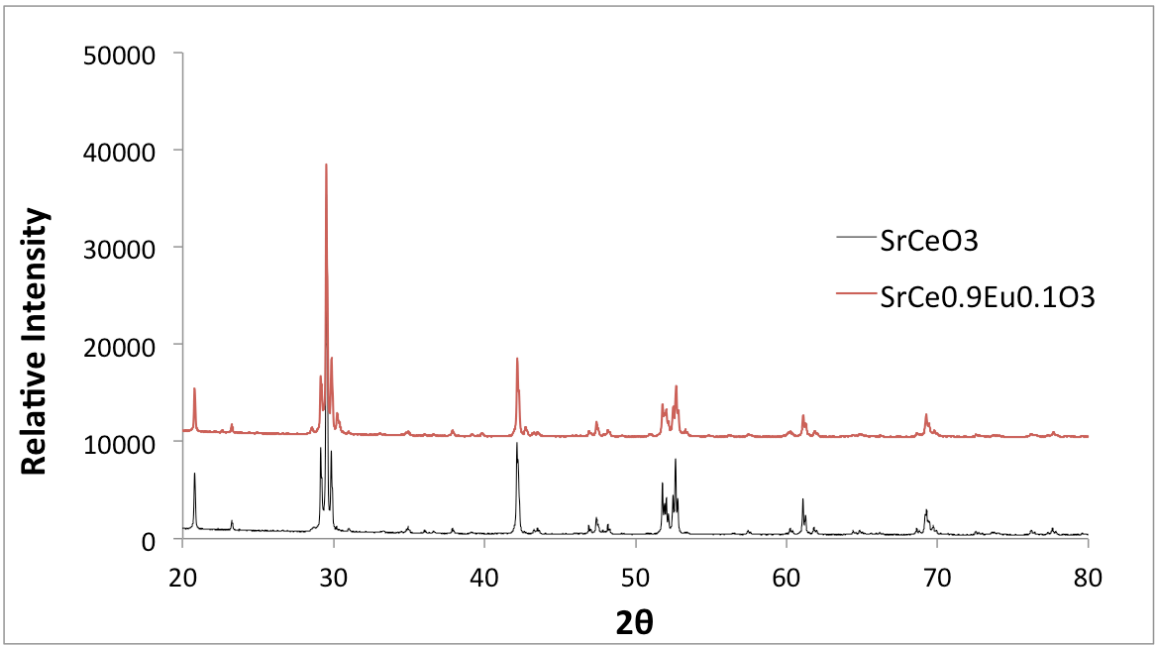

Figure 6-2 XRD results of solid-state synthesized $SrCeO_3$ and sol-gel method synthesized $SrCe_{0.9}Eu_{0.1}O_{3-\delta}$

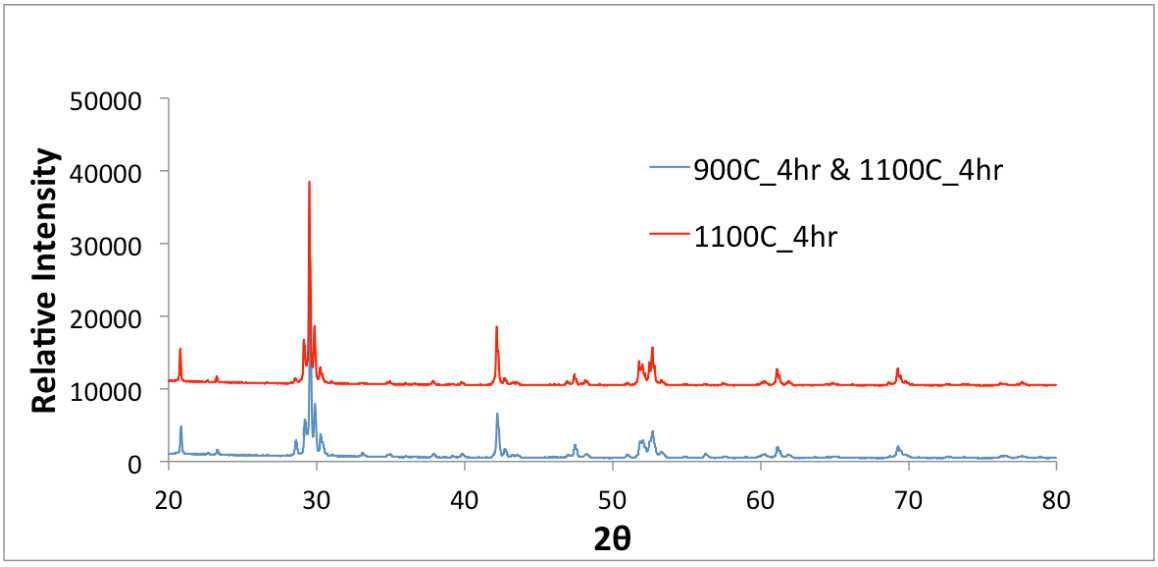

Figure 6-3 $SrCe_{0.9}Eu_{0.1}O_{3-\delta}$ Synthesized through different steps

As it is shown in Figure 6-3, same material can be obtained of the two procedures. However, the particle size will be different as the total calcination time is different. It

is suggested that one step calcination at 1100 °C for 4 hours is used for powder material preparation. These materials are used for support and membrane in fabricating the tubular membrane reactors. The shrink rate of the support and the membrane should be matched in order to obtain a dense membrane. The temperature that would lead to dense membrane was investigated in the following permeation tests. As it is shown in Figure 6-4, the membrane thickness that depends on the coating times is 39.7 μm. The dense membrane is obvious and the support is porous. NiO will be reduced around 500 °C can form larger pores for decreasing the diffusion limitation of the support.

The tube in this figure was sintered at 1450°C for 4 hours with 5 times colloidal coating inside the tube. However, the permeation test of the tube showed that tracer argon could permeate through the membrane even in room temperature. The reason is that the crystal size is too large and the gas can permeate through the large grain boundaries. It is obvious that the size is around 40 μm. The dense membrane is basically single layer. Decrease the temperature is one way to solve the over-sintered problem.

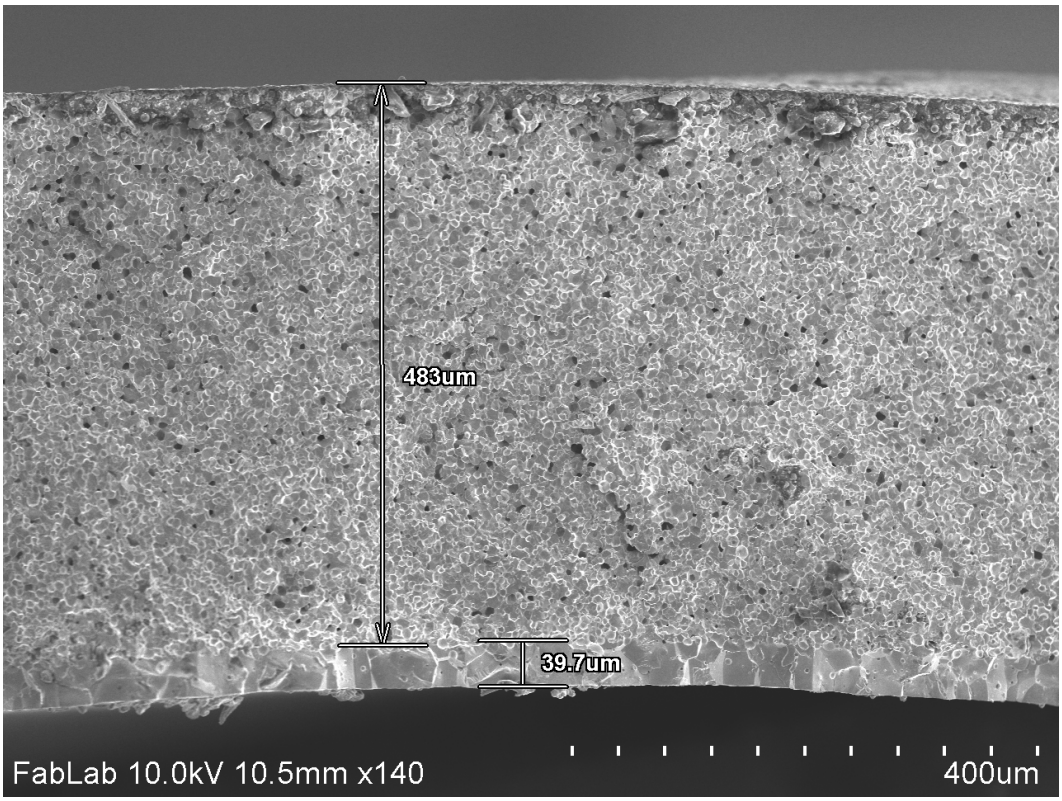

Figure 6-4 The SEM result of the cross-section that showing the membrane thickness

The sinter temperature was decreased to 1350 °C 4hrs. SEM results in Figure 6-5 and Figure 6-6 shows that the grain size is decreased and no obvious grain and be distinguished. The surface of the dense membrane is dense at average 5- μm grain size.

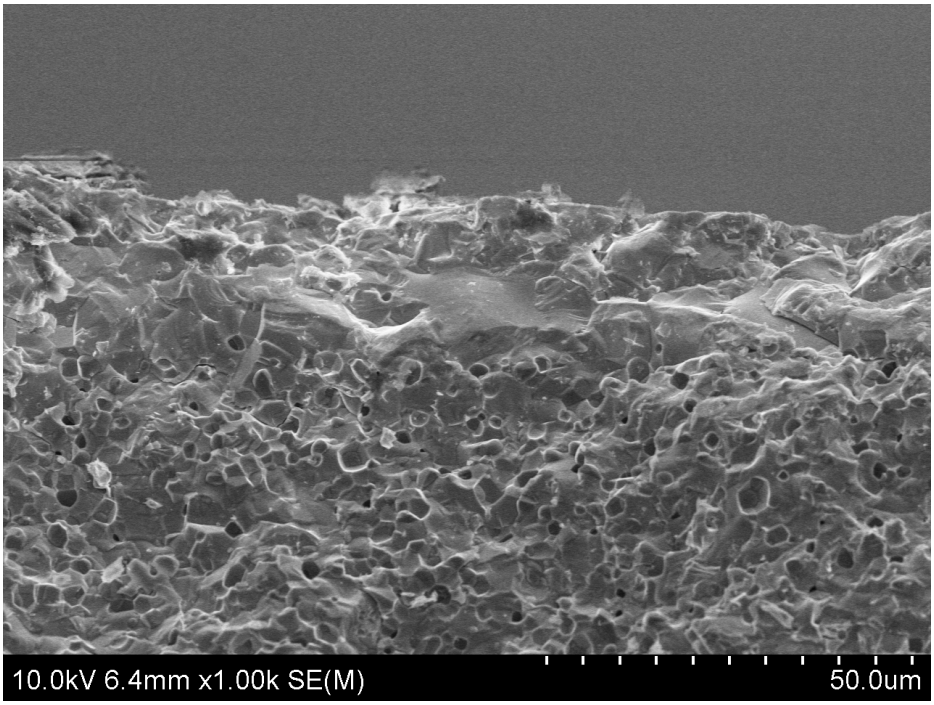

Figure 6-5 The cross-section of the tube sintered at 1350 °C 4hrs with 5-times colloidal coating

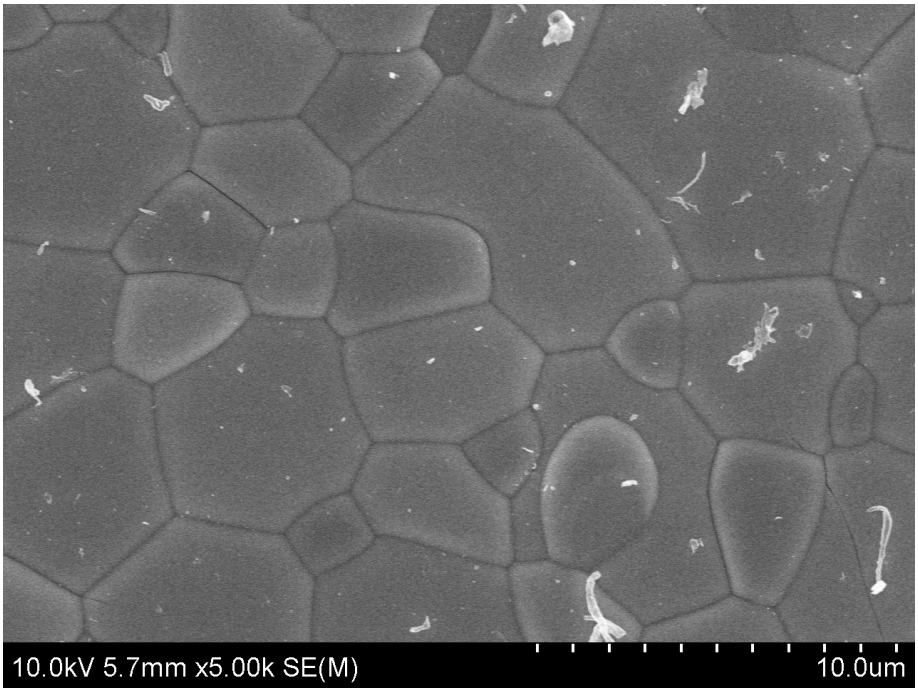

Figure 6-6 The surface image of the tube sintered at 1350 °C 4hrs with 5-times colloidal coating

There is tracer argon detected at the sweeping size of the tube above at the temperature above 500°C (Figure 6-9). Thermo expansion of the tube and membrane caused the membrane crack after NiO reduce. The thickness of the membrane was increase by coating the tube 10 times inside the tubular reactor and sintered at 1350 °C 4hrs.

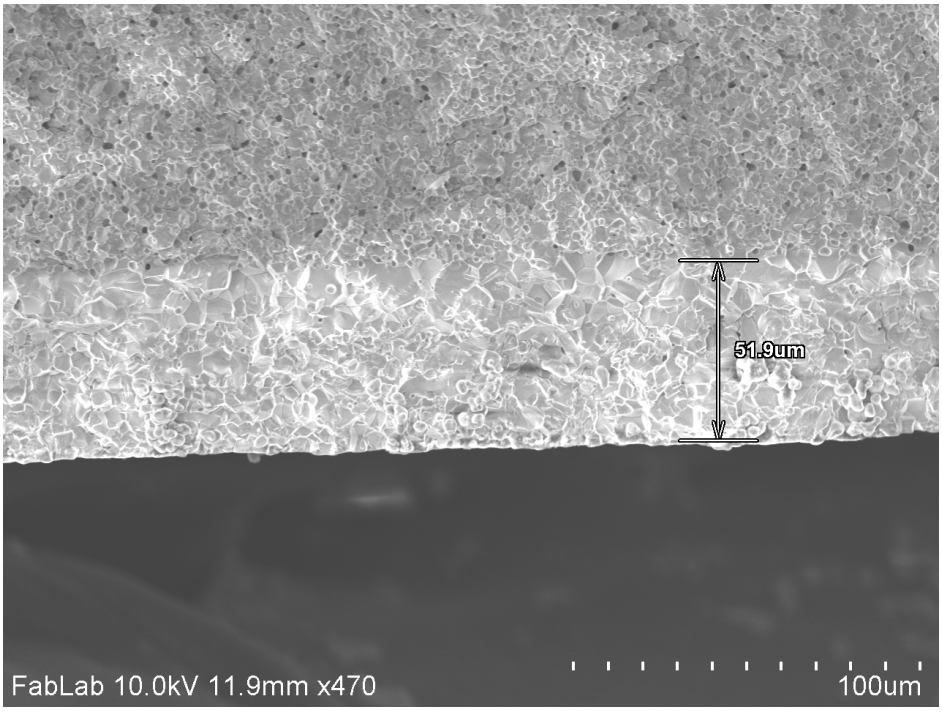

Figure 6-7 Dense membrane and thickness of the tube sintered at 1350 °C for 4hrs with 10-times colloidal coating

This tube that sintered at 1350 °C for 4hrs were coated 10 times. The thickness is obviously increased to 51.9 μm. The surface SEM image demonstrated that the membrane was dense. The average grain size is 5 μm with smallest size 2 μm to largest 10 μm. The permeation results tested was shown in Figure 6-10.

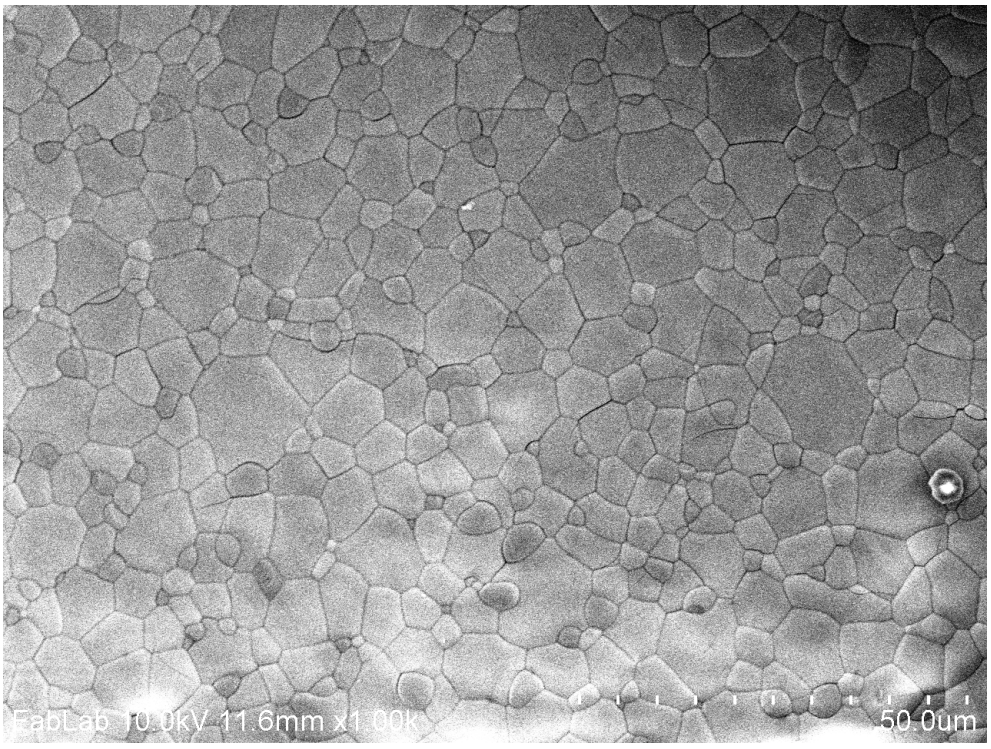

Figure 6-8 Surface image of dense membrane sintered at 1350 °C for 4hrs with 10-times colloidal coating

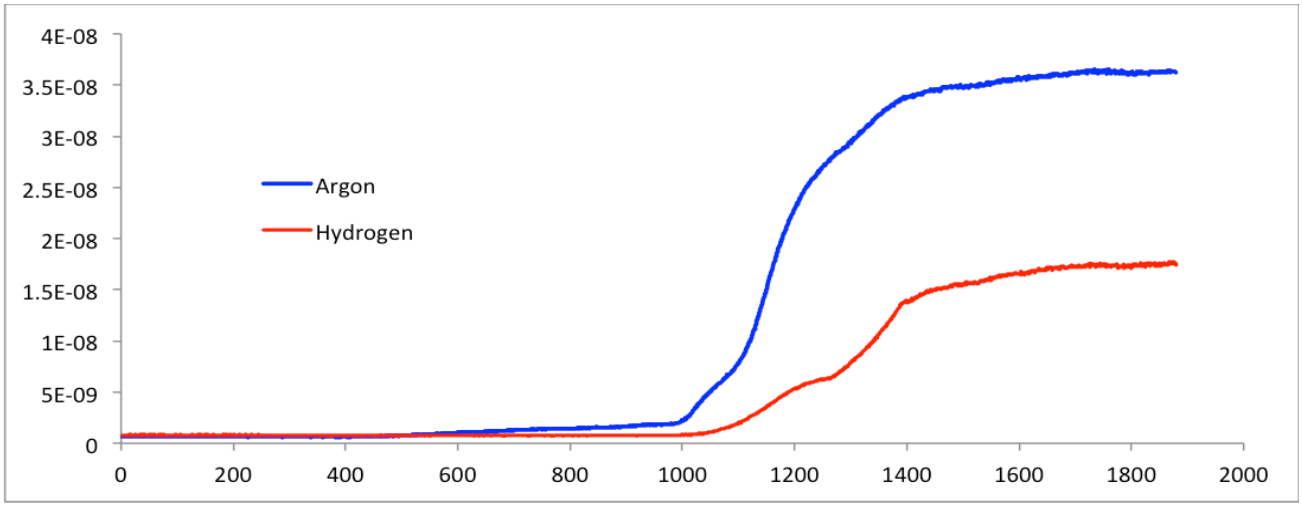

Figure 6-9 Hydrogen Permeation test of tube sintered at 1350 °C 4hrs with 5-times colloidal coating

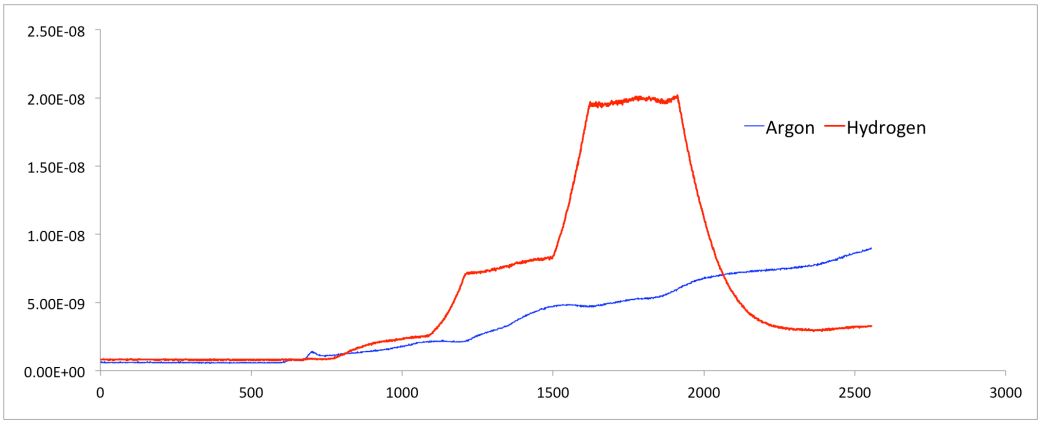

Figure 6-10 Hydrogen Permeation test of tube sintered at 1350 °C 4hrs with 10-times colloidal coating

The sweeping gas Helium was 40 mL/min and the gas supplied at the outside of tubular membrane reactors was 10mL/min hydrogen and 40 mL/min Argon. Various hydrogen concentrations was tested with five more tubular membrane reactors and the permeation of hydrogen can be calculated in table 6-1.

Table 6-1 Hydrogen permeation of the ESC membrane reactor

H_2 percentage in Feed gas	**700 °C**	**800 °C**	**900 °C**
12%	0.052 cc/min 0.00268 cc/min cm^2	0.211 cc/min 0.011 cc/min cm^2	1.012 cc/min 0.05 cc/min cm^2
24%	0.116 cc/min 0.005523 cc/min cm^2	0.450 cc/min 0.0214 cc/min cm^2	1.226 cc/min 0.06 cc/min cm^2
34%	0.170 cc/min 0.0088 cc/min cm^2	0.658 cc/min 0.034 cc/min cm^2	1.863 cc/min 0.097 cc/min cm^2

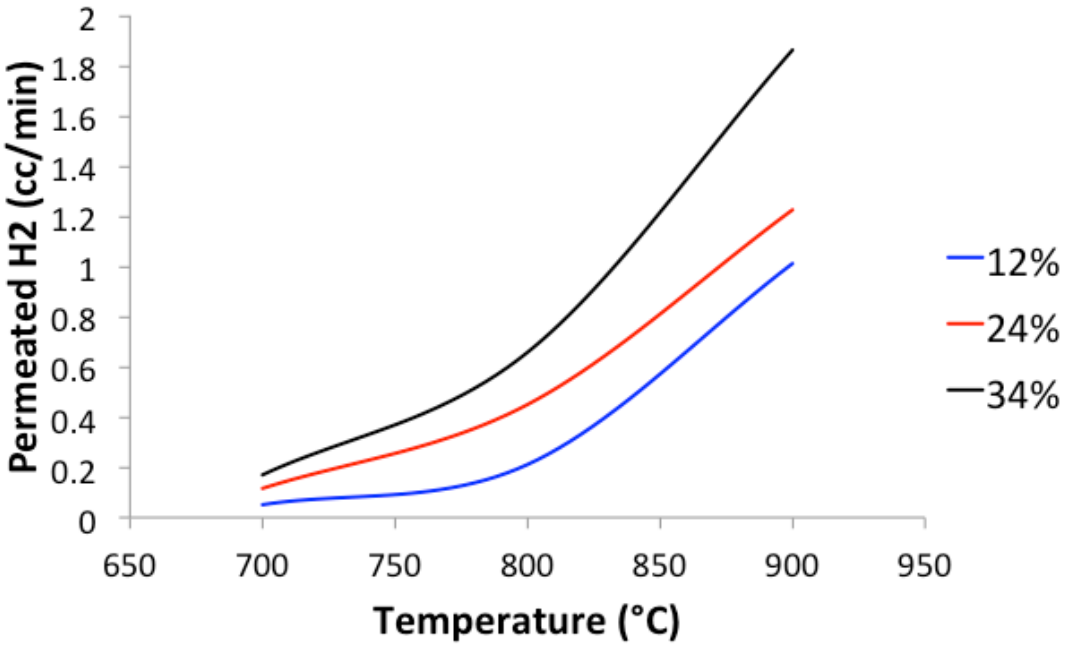

Figure 6-11 Hydrogen flux permeated at various hydrogen concentration from 700°C to 900°C

As it is shown in Figure 6-11, the hydrogen permeated increase with increasing temperature. High concentration of hydrogen leads to higher permeation. The highest flux obtained at 900°C 1.863 cc/min when hydrogen concentration supplied at the outside of the tubular membrane reactor was 34%. The lowest permeation 0.052 cc/min was at 700°C. Temperature is a main factor that influent the permeation of hydrogen flux. When the temperature is low at 700°C, the concentration has less influence of the flux. The concentration difference at high temperature was obvious larger than lower temperature. The permeation of hydrogen is relatively low for the reason that electron conductivity is limiting the hydrogen flux. In order to improve the hydrogen permeation flux, Pr-doped material is used for membrane reactors.

The $SrCe_{0.9}Pr_{0.1}O_{3-\delta}$ material was also synthesized through both conventional solid-state method and sol-gel method. Both of the methods can obtain pure $SrCe_{0.9}Pr_{0.1}O_{3-\delta}$ demonstrated in Figure 6-12.

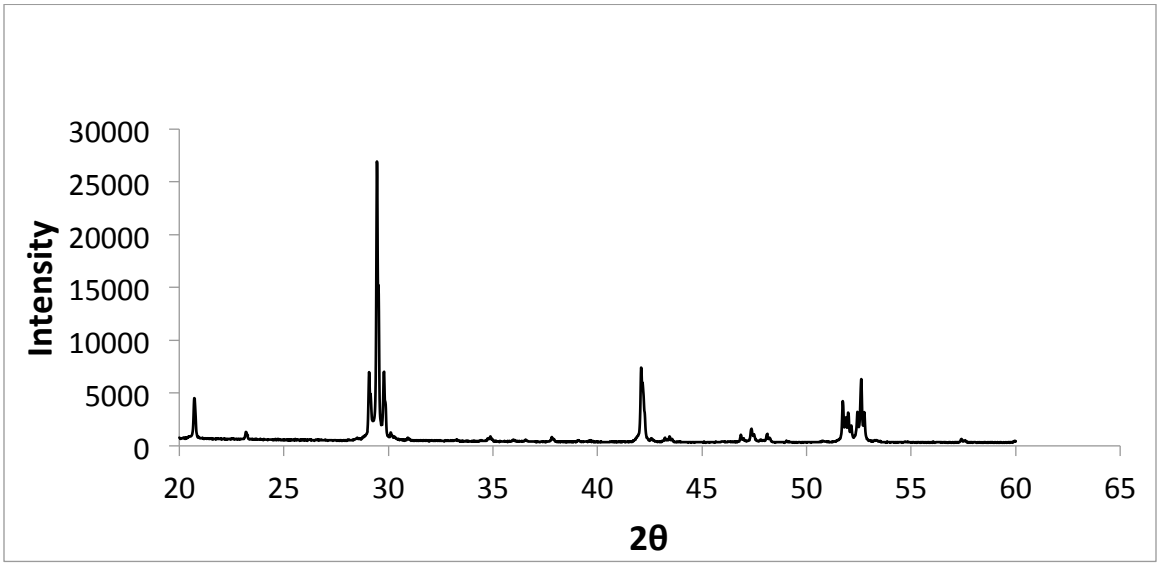

Figure 6-12 XRD pattern of $SrCe_{0.9}Pr_{0.1}O_{3-\delta}$ after Calcination 1100 °C 4hrs

The $SrCe_{0.9}Pr_{0.1}O_{3-\delta}$ powder was used for making the colloidal solution for coating. 3-times colloidal coating of the tubular support is shown in Figure 6-13 and 6-14. The tube was sintered at 1450 °C for 4hrs. Pr has a low melting point. The surface image can clearly show that the grain boundary melt while sintering. It is proposed that Pr evaporate at high temperature 1450 °C for 4hrs with 3-times colloidal coating. 10-times coating was applied in order to prevent evaporating with thicker membrane and sinter at lower temperature 1400 °C and 1350 °C for 4 hours. The hydrogen permeation tests of this kind of tubes are shown in Figure 6-15 and Figure 6-16.

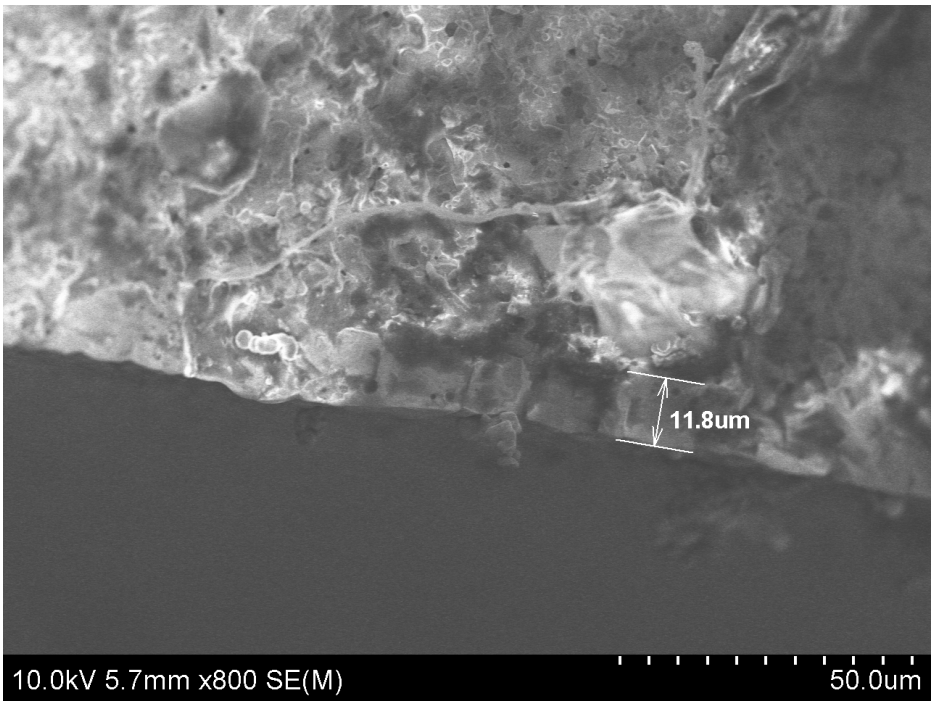

Figure 6-13 Dense membrane and thickness of the tube sintered at 1450 °C for 4hrs with 3-times colloidal coating

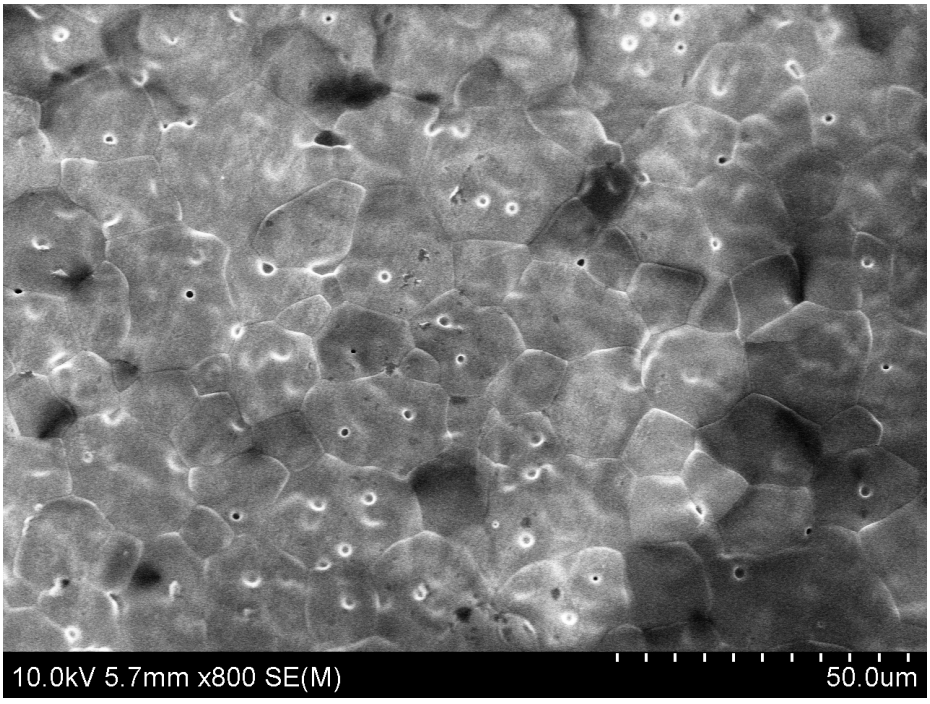

Figure 6-14 Surface image of the membrane sintered at 1450 °C for 4hrs with 3-times colloidal coating

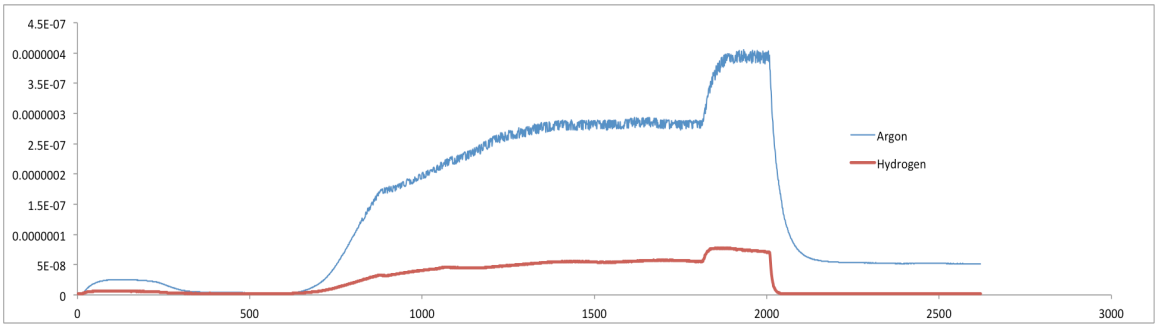

Figure 6-15 Hydrogen Permeation test of tube sintered at 1400 °C 4hrs with 10-times colloidal coating

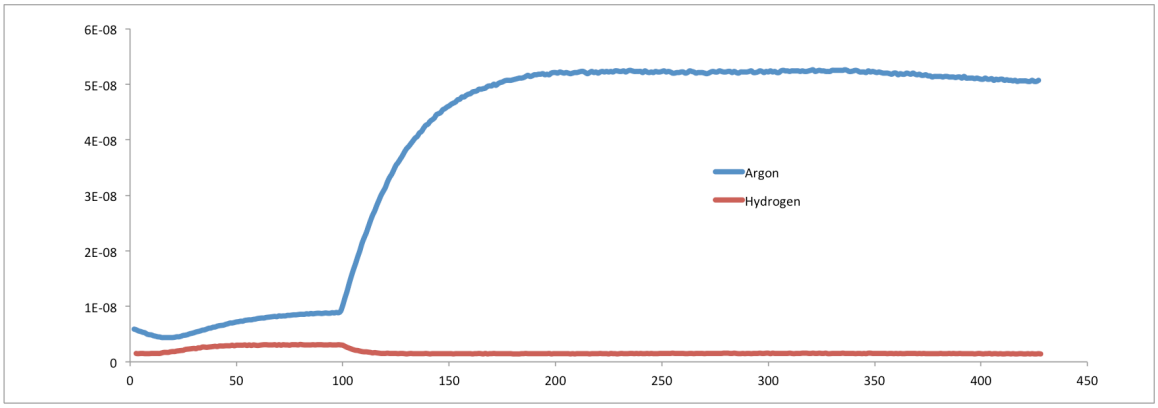

Figure 6-16 Hydrogen Permeation test of tube sintered at 1350 °C 4hrs with 10-times colloidal coating

It is obvious that the tubes still have leaking problems due to the mismatch of thermal expansion coefficient (TEC) of the cell components and further improvement is in process. The Praseodymium was likely evaporated at high temperature as small pinholes could be observed in the SEM. EDX is recommended to detect the remaining Praseodymium in the material. Also the sintering process will change to hold at 1400 °C for only one hour and stay at lower temperature for 6 to 8 hours.

Methods of fabricating the $SrCe_{0.9}Pr_{0.1}O_{3-\delta}$ membrane reactor still need to be explored in the future.

In order to estimate the hydrogen permeation through 30μm thin membranes, the theoretical fluxes were calculated through similar steps in Chapter 5 (Table 6-2).

Table 6-2 Calculated hydrogen permeation flux under [100% H_2, Pt/membrane/Pt, 5%H_2] between 600°C and 800°C (L=30μm thick).

	T (K)	Total Conductivity (S/cm)	Transference Number of Electrons	Hydrogen Flux of 30μm membrane (mol/min cm^2)
10% Pr-doped	873.15	0.00053174	0.0039	8.04E-08
	973.15	0.00102565	0.0384	1.64E-06
	1073.15	0.00192221	0.0834	7.02E-06
20% Pr-doped	873.15	0.00017624	0.35	1.54E-06
	973.15	0.00047206	0.486	5.12E-06
	1073.15	0.00083349	0.548	1.10E-05

The theoretical permeation of hydrogen (Figure 6-17) through thin $SrCe_{0.9}Pr_{0.1}O_{3-\delta}$ membrane in the membrane reactor is compared with $SrCe_{0.9}Eu_{0.1}O_{3-\delta}$ membrane. The flux of Pr-doped material is higher at high temperature but lower under 700 °C. However, the theoretical flux is higher at 800°C. The calculated hydrogen fluxes for 20mol% Pr-doped material is higher than 10mol% Pr-doped material and 10mol% Eu-doped material.

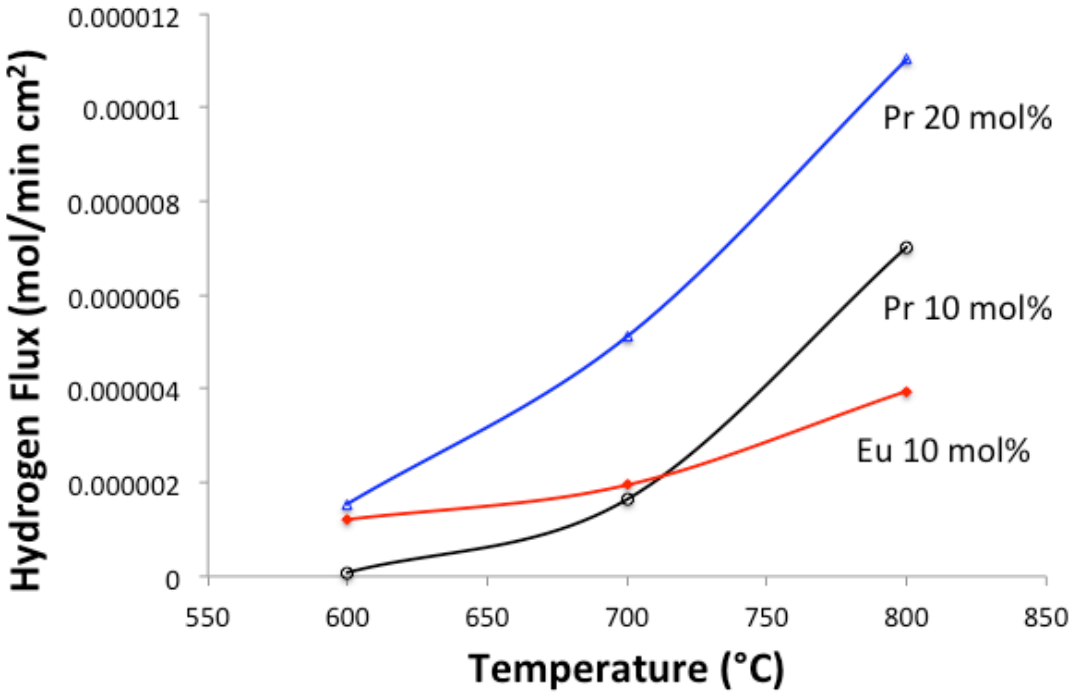

Figure 6-17 Theoretical Permeated Hydrogen Flux through 30μm membrane at case 1 calculated by Wagner Equation

Chapter 7: Modified Nafion® Membrane used in Electrochemical Ammonia Compression and Separation

7.1 Introductions and Background

Electrochemical hydrogen Compression has a great advantage over the traditional mechanical compression, which already be fully demonstrated by Rohland [45]. The principles support the electrochemical compression is based on solid polymer electrolyte technology [46-47]. Previous researchers [48-53] have explored the separation of hydrogen from the gas mixture through the proton exchange membrane cell. The hydrogen is supplied at the anode side at low concentration and the protons are transferred to cathode through the solid electrolyte membrane.

Based on the hydrogen compression principles, the proton membrane is modified to Ionic exchange membrane that transfer ammonia ion. Ammonia is the most trusted refrigerant in industrial refrigeration system. Electrochemical compression of ammonia is an effective method in ammonia compression.

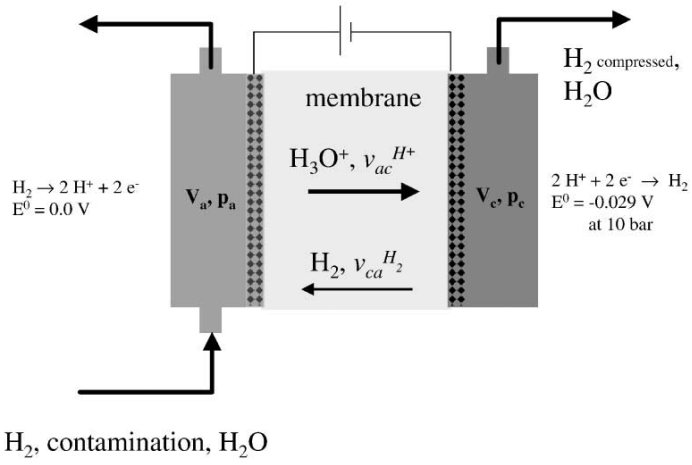

Figure 7-1. Principle of the electrochemical hydrogen compressor [54]

The single compression cell consists of two electrodes and functionalized membrane as the solid electrolyte that transfer proton in the direction of the external applied current. When the membrane is saturated with ammonia solution, the ammonia and hydrogen gas is supplied at anode side; the oxidized hydrogen is changed to proton and reacts with the ammonia ion. The principle of ammonia compression is believed to be the following:

$$2NH_4^+ + 2OH^- + 2H^+ + 2e^- \rightarrow 2NH_4^+ + 2H_2O \qquad \text{Equation (7-1)}$$

Membrane electrode assembly (MEA) contains a polymer membrane [55] can transfer protons from anode to cathode and also separate the gas phase of both sides. The water percentage it contains is supposed to remains at saturation status. The ammonia molecule will react with the proton generated at the surface of the electrode and transferred through the membrane as ammonia ion. Hydrogen and ammonia molecules are formed at the cathode by consuming the ions transferred via the polymer electrolyte.

In the actual test cell, two endplates are flanged at both anode and cathode sides that usually made of stainless steel that can resists high pressure and contain hydrogen inlet and outlet tubes connected to the storage tanks that controlled by an electronic pressure gauge and detected with pressure sensor meters. A specific gasket between the end plates and the gas diffusion layer is used to seal the anode and cathode flow field. Commercial membranes, Nafion®-based membranes, are hot pressed [56-59] with the carbon supported platinum or platinum-ruthenium catalyst electrodes with various loading (Figure 7-2). The hydrogen stream is led through a humidifier in order to avoid the dehydration of membrane.

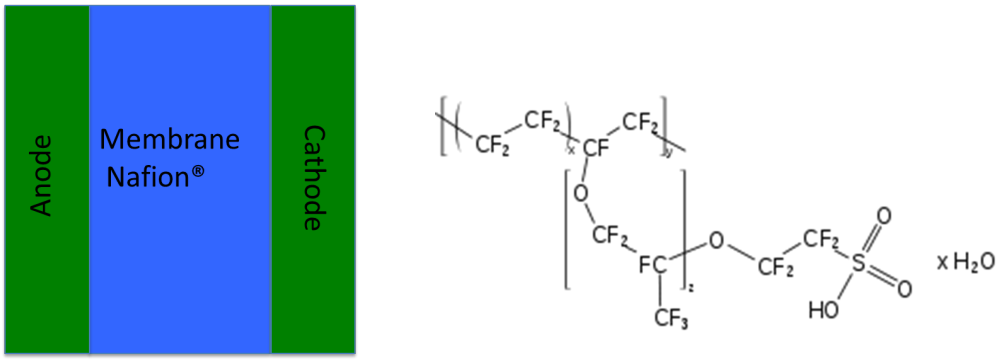

Figure 7-2. Scheme of Membrane Electrolyte Assembly (MEA) and the Commercial Nafion® Membrane Structure

Total cell voltage consists of the Nernst potential, the polarization voltage and the ohm resistance drop. The kinetics of the reduction is demonstrated to be slightly slower than the kinetics of oxidation supported by the Volmer-Tafel-mechanism. The pressure difference between the cathode and the anode affects the cell voltage according to the Nernst Equation:

$$E_n = E_0 + \frac{RT}{2F} \ln\left(\frac{p_c}{p_a}\right) \qquad \text{Equation (7-2)}$$

Where E_n is the Nernst potential caused by the concentration gradient and charge transfer; E_0 is the standard potential determined by the intrinsic reaction; R is the gas constant; T is the temperature of the reaction; p_c is the partial pressure of the cathode side; p_a is the partial pressure of the anode side.

As it is known that the high-pressure difference between the two sides of the membrane seems highly possible to cause ammonia permeation through the

membrane electrolyte. As the first Fick's law describes, the gas diffusion rate is proportional to the concentration gradient.

$$\frac{dm}{dt} = -D_m \times \frac{dc}{dx} \qquad \text{Equation (7-3)}$$

Where D_m is the diffusion coefficient; $\frac{dm}{dt}$ is the gas diffusion rate; $\frac{dc}{dx}$ is the concentration gradient through the membrane.

The diffusion of ammonia molecules decreases the pressure will difference between anode and cathode electrode. The diffusion flow seems possible to be compensated by the reduction of hydrogen at the cathode, which will reversely consume extra electric power to minimize the effect, meaning higher current required for the system.

7.2 Experiment

The Nafion® Membrane (Nafion 115, FuelCellStore) was modified by changing the acidic membrane to basic membrane. Rinsing the Nafion® Membrane in the ammonia solution (28% in H_2O, Sigma-Aldrich) for 24 hours in order to transform all of the function groups. Assemble MEA with the transformed membrane and platinum loaded gas diffusion layer (0.3mg/cm^2 catalyst loading, size 2.5cm x 2.5cm, FuelCellsEtc). Modified Nafion®-based membranes were hot pressed with the carbon supported platinum or platinum-ruthenium catalyst electrodes using manual bench top heated press (Carver 4386). In the test cell, two endplates are flanged at both anode and cathode sides that usually made of stainless steel that can resists high pressure and contain ammonia inlet and outlet tubes connected to the storage tanks that

controlled by an electronic pressure gauge and detected with pressure sensor meters. A specific gasket between the end plates and the gas diffusion layer is used to seal the anode and cathode flow field. The ammonia gas is led through an ammonia solution humidifier in order to avoid the dehydration of membrane. Set up the system as shown in figure 7-3.

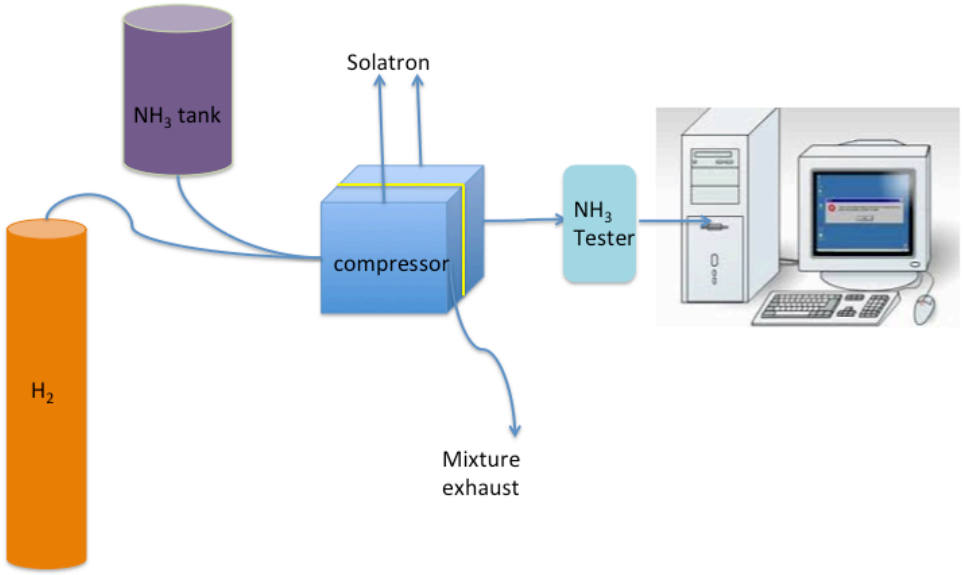

Figure 7-3. The schematic of the testing system

The Conductivity was measured by a solartron 1260 ES and a Gamery reference 3000. Temperature and relative humidity were controlled with Arbin fuel cell test station. Test stations can provide electrochemical parameters that represent the kinetics and thermodynamics properties of the modified membrane. The test stations can use Electrochemical Impedance Spectroscopy (EIS) method that provides sine signal AC amplitude to get the conductivity of the membrane. Arbin test station will be used as the controller of the entire gas phase inlet with various humidity and temperature. The

ammonia compressed can be detected via collecting the pressure data at the output tube.

7.3 Results and Data Analysis

It is demonstrated that the conductivity of the modified membrane increase with increasing temperature and relative humidity. The maximum conductivity of the modified membrane is 0.037 S/cm obtained at 70 °C of 50% relative humidity. It is shown that the membrane has the ability to transfer proton from anode to cathode. The function group density of the membrane is comparable with the commercialized the Nafion®-based membrane.

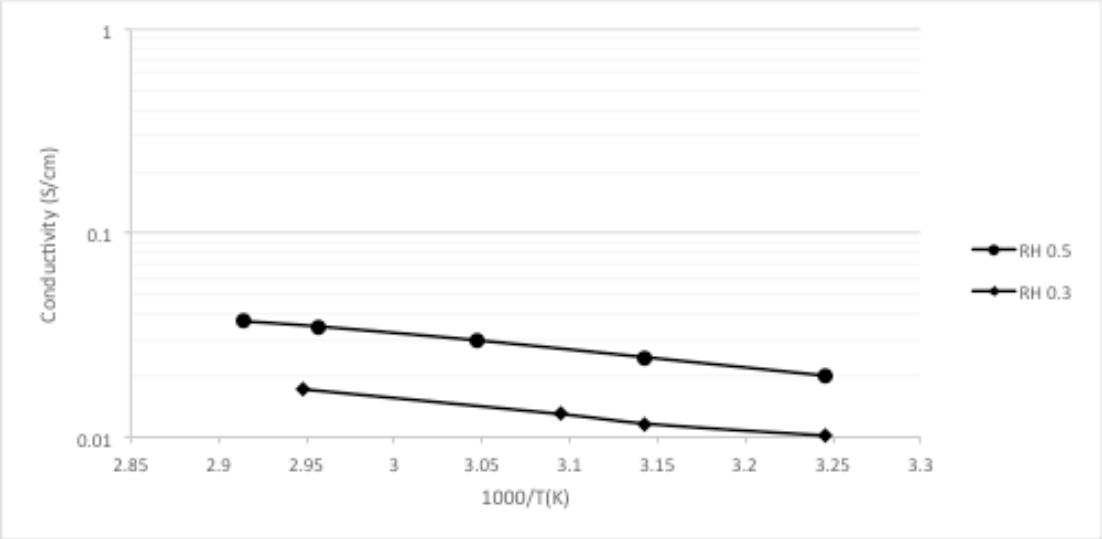

Figure 7-4. The conductivity of modified membrane under different temperature

The cycle voltammetry of the assembled cell with the modified membrane was tested with a Solartron 1260 ES. The graph Voltage versus Current demonstrates the existence of the electrochemical ammonia compression procedure. If the Voltage versus Current graph is a straight line, the membrane is pure ohm resistance with no

capacitor and inductor characteristic. As Figure 7-5 shown, the voltage versus current is not a straight line. The highest current is 0.14 A at the maximum Voltage.

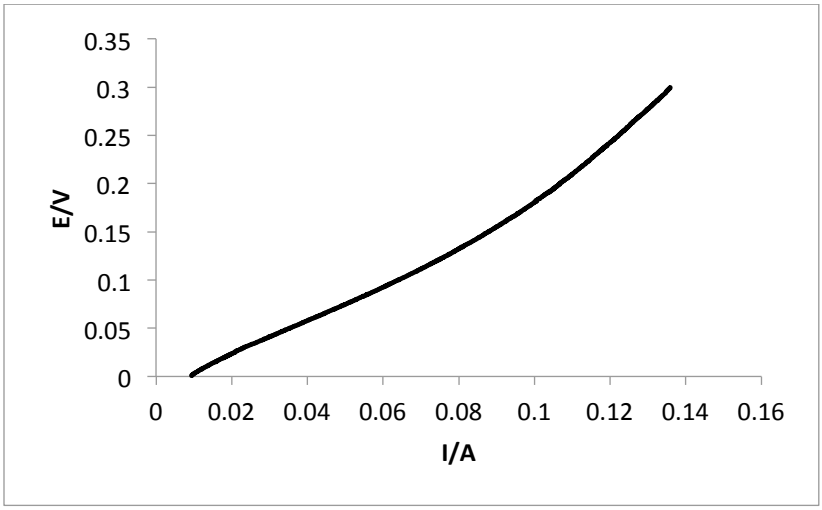

Figure 7-5. Polarization curve of the compressor (25 °C, flow rate ratio NH_3:H_2 4:3, 0.05 mg/cm^2 Pt loading of Anode, 0.1 mg/cm^2 Pt loading of Cathode, Modified Nafion® 115)

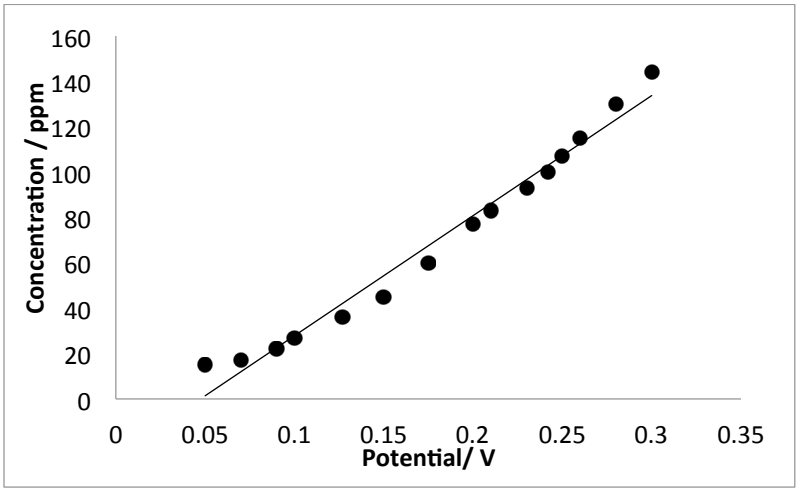

Figure 7-6. The Concentration of ammonia under different potential (25 °C, flow rate ratio NH_3:H_2 4:3, 0.05 mg/cm^2 Pt loading of Anode, 0.1 mg/cm^2 Pt loading of Cathode, Modified Nafion® 115)

The current is larger when the voltage is set higher. The charge transfer on the surface of the membrane can be measured by controlling the current. The partial pressure of the ammonia at the cathode side can be monitored by ammonia sensor. Its value varies with the cell potential supplied. As Figure 7-6 demonstrated, the concentration is higher when the voltage increases and reaches 140 ppm at 0.3V.

The total Flow rate of the inlet stream is 0.23L/min because of ammonia has the great preference of dissolving in water. The difference between the pure hydrogen and the ammonia-hydrogen mixture showed in Figure 7-7 and 7-8 demonstrated that the hydrogen compression is still existing when the pure hydrogen pumping in. The membrane can be acidized by the large amount of hydrogen. The maximum current obtained when NH_3: H_2 = 1:1 is 0.16, which is higher than NH_3: H_2 = 4:3 (0.14).

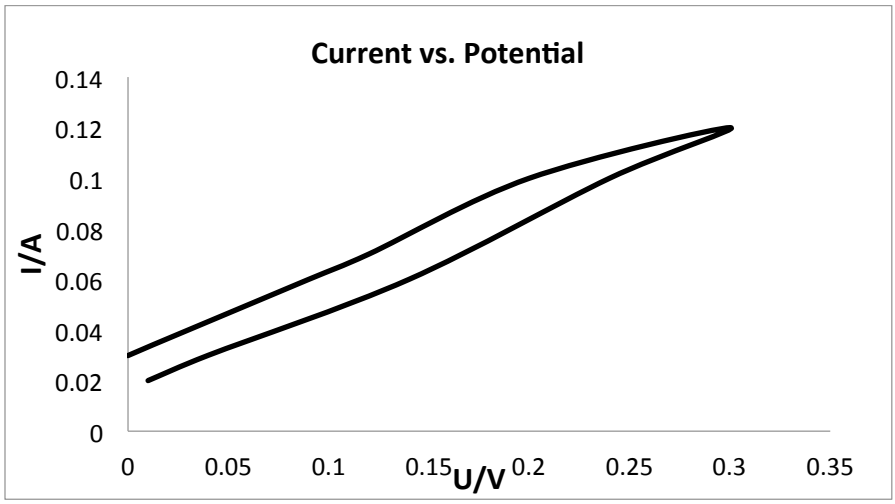

Figure 7-7. The polarization curve of the compressor under pure H_2 (3psi Flow rate 0.21L/min, GDE: Fuel Cells Etc® PtC 40% 0.3 mg/cm^2, 2.5cmx2.5cm Modified Nafion® 115, 28°C)

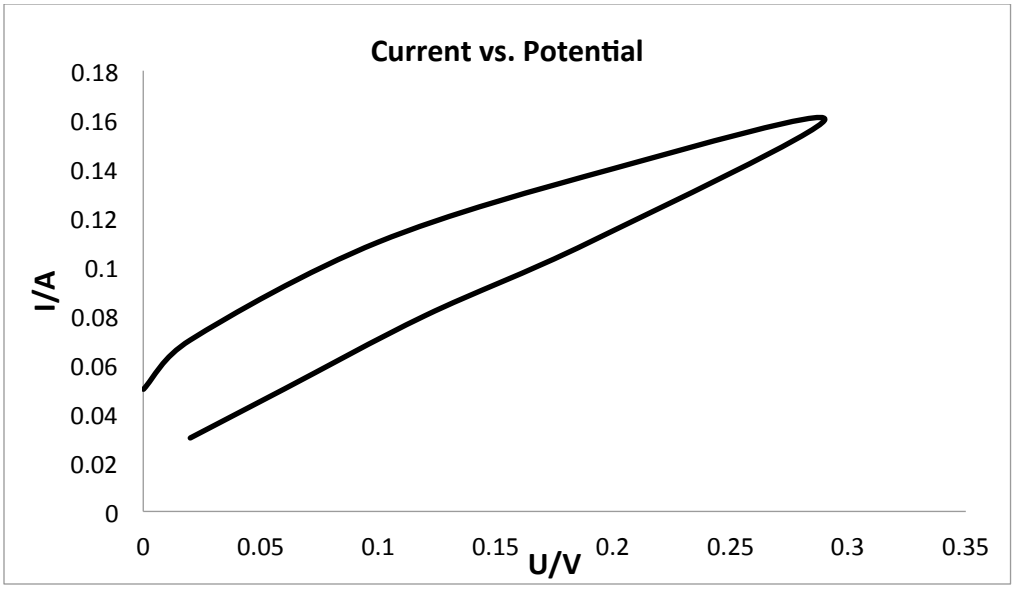

Figure 7-8. The polarization curve at NH_3: H_2 = 1:1 (3psi Flow rate 0.21L/min, 28 °C, GDE: Fuel Cells Etc® PtC 40% 0.3 mg/cm^2, 2.5cmx2.5cm Modified Nafion® 115, 28°C)

The cycle of the voltage change from 0 to 0.3V and change back to 0V (Figure 7-9). The concentration of ammonia is increasing with increasing voltage and decreasing with decreasing voltage. There is a time delay of testing resulting in the convex shape when voltage decreasing. The ammonia will diffuse through the membrane at a steady flow rate is hydrogen stopped and pure ammonia is supplied. The concentration is 34 ppm when stable.

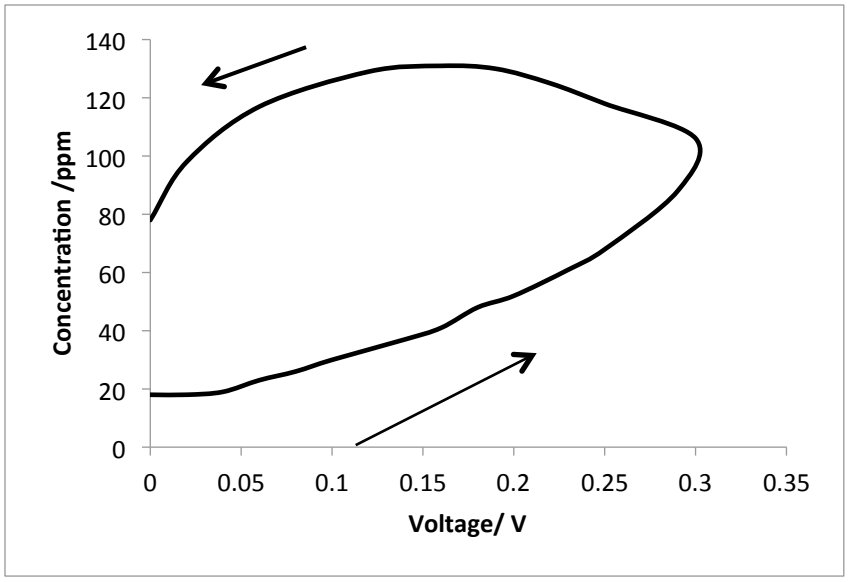

Figure 7-9. The Concentration change with Voltage (The arrow shows the direction of the cycle, H_2: NH_3=1:1.)

The hydrogen that goes through a bubbler introduces water in the system, which highly enhanced the conductivity. The current is 0.12 A at 0.2V (Figure 7-10). The current of supplying dry hydrogen is 0.1A at 0.2V.

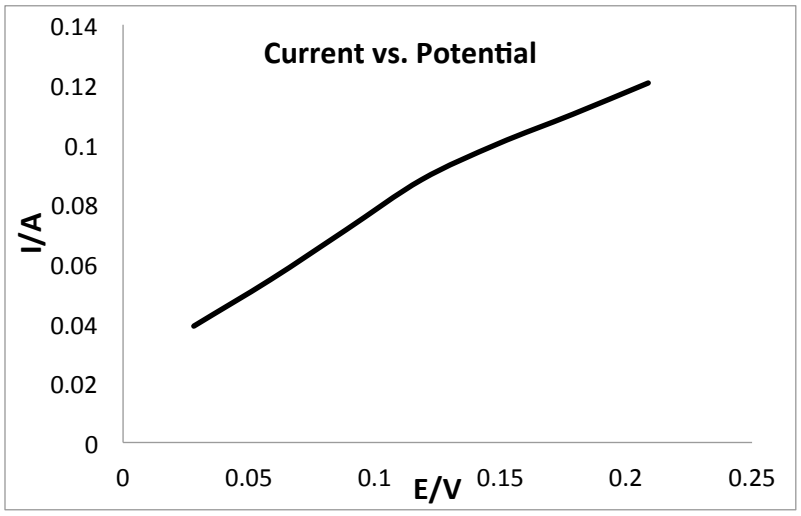

Figure 7-10. The polarization curve of the compressor with wet H_2 (3% H_2O, 3psi Flow rate 0.21L/min, NH_3: H_2 = 1:1,GDE: Fuel Cells Etc® PtC 40% 0.3 mg/cm^2, 2.5cmx2.5cm Modified Nafion® 115, 28°C)

As it is shown in Figure 7-11, the concentration is highly enhanced compared to dry hydrogen. The maximum concentration is 388ppm at 0.2V. The ammonia sensor range is not enough to measure the higher concentration.

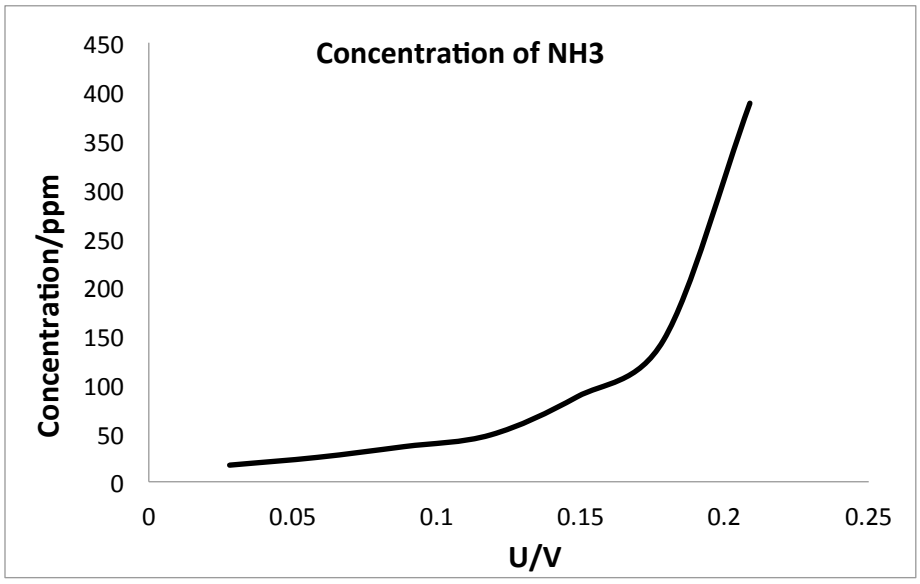

Figure 7-11. The concentration of ammonia at cathode when supplying wet H_2 (3% H_2O, 3psi Flow rate 0.21L/min, NH_3: H_2 = 1:1,GDE: Fuel Cells Etc® PtC 40% 0.3 mg/cm^2, 2.5cmx2.5cm Modified Nafion® 115, 28°C)

4.4 Conclusion

The conductivities of ammonium exchanged Nafion® 115 membranes were measured under 30% and 50% relative humidity. The maximum conductivity 0.035 S/cm is obtained at 50% relative humidity and 70 °C. Ammonia conductivity is approximately an order of magnitude lower than proton conductivity. Performance of a single cell ammonia pump was measured. The maximum current density of 30 mA/cm2 was obtained at 0.3 V. Test was run at 25 °C with low platinum loadings (0.05 mg/cm^2 Anode and 0.1 mg/cm^2 Cathode) and the volume feed ratio of ammonia

to hydrogen was 4 to 3. The higher catalysts may lead to the better performance that the current increasing from 0.13 to 0.16 A. The hydrogen supply dilutes the concentration of ammonia and prevents the ammonia diffusion at some degree by decreasing the concentration gradient of anode and cathode sides. Maybe the temperature difference from 25 to 28 causes a little bit increase. The current at 0V may due to the diffusion. The waiting time should be longer for the system stable to avoid the oscillating curve. The system need warm up at the beginning and a few cycles maybe needed for activation. The relationship of catalyst loading to the polarization curve needed to be investigated. The ability to pump ammonia electrochemically was confirmed in this single cell experiment.

Chapter 8: Conclusions and Future Work

8.1 Conclusions

The total conductivity of $SrCe_{1-x}Pr_xO_{3-\delta}$ (x=0.08, 0.1,0.15,0.2) was measured by impedance spectroscopy. The total conductivity of $SrCe_{0.9}Pr_{0.1}O_{3-\delta}$ is comparable to $SrCe_{0.9}Eu_{0.1}O_{3-\delta}$ at 10% dry hydrogen atmosphere. However, the electronic transference number of $SrCe_{0.9}Pr_{0.1}O_{3-\delta}$ is higher than $SrCe_{0.9}Eu_{0.1}O_{3-\delta}$ according to OCP measurement. Both of the proton and electron conductivity increase with increasing temperature. The proton conductivity equals to electron conductivity at 800 °C for 20 mol% Pr-doped $SrCeO_{3-\delta}$ under dry hydrogen atmosphere. The theoretical highest hydrogen permeation is supposed to occur at this temperature for 20% Pr doped material. The bulk-limiting hydrogen permeation flux is determined by ambipolar conductivity. The existence of water vapor decreases the hydrogen permeation fluxes because the water vapor increases the partial pressure of oxygen and decrease n-type electron conduction. The highest permeated hydrogen flux was 0.0043 cc/cm^2 min at 850 °C for 10 mol% Pr-doped $SrCeO_{3-\delta}$ under dry hydrogen atmosphere. However, the maximum hydrogen flux for 20 mol% Pr-doped $SrCeO_{3-\delta}$ under dry hydrogen atmosphere is 1.12 cc/cm^2 min at 800 °C.

The thin membrane reactor was fabricated in order to decrease the bulk-limiting effect. The hydrogen permeation was highly increased for $SrCe_{0.9}Eu_{0.1}O_{3-\delta}$ thin membrane reactors according to our previous research. The $SrCe_{0.9}Pr_{0.1}O_{3-\delta}$ is a better substitution as it has higher electron conductivity than $SrCe_{0.9}Eu_{0.1}O_{3-\delta}$. Pr-doped material was used as the thin membrane in the membrane reactors. However, the

fabrication process of getting dense $SrCe_{0.9}Pr_{0.1}O_{3-\delta}$ membrane on the porous support needs further improvement. Nano-dimensioned powders can also possibly reduce the membrane thickness and further increase the permeation.

The ammonium exchanged Nafion® 115 membranes were measured in a single cell ammonia pump. Although there is ammonia diffusion through the membrane due to the concentration gradient, the ability to pump ammonia electrochemically was confirmed in this single cell experiment.

References

1. Balachandran, U., et al. "Development of mixed-conducting oxides for gas separation." *Solid State Ionics* 108.1 (1998): 363-370.

2. Iwahara, Hiroyasu. "Proton conducting ceramics and their applications." *Solid State Ionics* 86 (1996): 9-15.

3. Tsuji, Toshihide, and Takuji Nagano. "Electrical conduction in SrCeO 3 doped with Eu 2 O 3." *Solid state ionics* 136 (2000): 179-182.

4. Heidari, Marzieh, et al. "Comparison of microstructure and hydrogen permeability of perovskite type ACe 0.9 Y 0.1 O 3-δ (A is Sr, Ba, La, and BaSr) membranes." *International Journal of Hydrogen Energy* 40.20 (2015): 6559-6565.

5. Iwahara, Hiroyasu. "Technological challenges in the application of proton conducting ceramics." Solid State Ionics 77 (1995): 289-298.

6. De Schutter, F., et al. "Proton conductivity in strontium cerates for hydrogen gas sensors in coal gasification systems." Solid State Ionics 57.1 (1992): 77-81.

7. Zhou, Wei, Ran Ran, and Zongping Shao. "Progress in understanding and development of Ba 0.5 Sr 0.5 Co 0.8 Fe 0.2 O 3− δ-based cathodes for intermediate-temperature solid-oxide fuel cells: a review." Journal of Power Sources 192.2 (2009): 231-246.

8. Shao, Zongping, and Sossina M. Haile. "A high-performance cathode for the next generation of solid-oxide fuel cells." Nature 431.7005 (2004): 170-173.

9. Mather, Glenn C., and M. Saiful Islam. "Defect and dopant properties of the SrCeO3-based proton conductor." Chemistry of materials 17.7 (2005): 1736-1744.

10. Iwahara, H., et al. "Protonic conduction in calcium, strontium and barium zirconates." Solid State Ionics 61.1 (1993): 65-69.

11. Kosacki, I., et al. "Electrical properties of SrCe 0.95 Yb 0.05 O 3 in hydrogen containing atmospheres." Solid State Ionics 59.3 (1993): 287-296.

12. Beskow, Gunnar. "VM Goldschmidt: Geochemische Verteilungsgesetze der Elemente." GFF 46.6-7 (1924): 738-743.

13. Uchida, H., et al. "Formation of protons in SrCeO 3-based proton conducting oxides. Part II. Evaluation of proton concentration and mobility in Yb-doped SrCeO 3." Solid State Ionics 36.1 (1989): 89-95.

14. Yajima, T., et al. "Protonic conduction in SrZrO 3-based oxides." Solid State Ionics 51.1 (1992): 101-107.

15. Sunarso, J., et al. "Mixed ionic–electronic conducting (MIEC) ceramic-based membranes for oxygen separation." Journal of Membrane Science 320.1 (2008): 13-41.

16.Oh, Tak-keun, Heesung Yoon, and E. D. Wachsman. "Effect of Eu dopant concentration in SrCe 1− x Eu x O 3− δ on ambipolar conductivity." *Solid State Ionics* 180.23 (2009): 1233-1239.

17. Rhodes, J. M., et al. "Solid State Ionics Devices II-Ceramic Sensors." The Electrochemical Society Proceedings Series, Pennington, NJ. 2001.

18. Oh, T., et al. "Stability of SrCe0. 9Eu0. 1O3-δ under dry/wet hydrogen atmosphere." Ionics 15 (2009): 525-530.

19. Song, S-J., et al. "Defect structure and transport properties of Ni–SrCeO3− δ cermet for hydrogen separation membrane." Journal of the Electrochemical Society 152.11 (2005): J125-J129.

20. Song, S-J., et al. "Hydrogen permeability of SrCe 1− x M x O 3− δ (x= 0.05, M= Eu, Sm)." Solid State Ionics 167.1 (2004): 99-105.

21. Song, S-J., et al. "Numerical modeling of hydrogen permeation in chemical potential gradients." Solid State Ionics 164.1 (2003): 107-116.

22. Iwahara, Hiroyasu, et al. "Prospect of hydrogen technology using proton-conducting ceramics." Solid State Ionics 168.3 (2004): 299-310.

23. Araki, Sadao, et al. "Synthesis and characterization of mixed ionic–electronic conducting Ca 0.8 Sr 0.2 Ti 0.7 Fe 0.3 O 3− α thin film." Solid State Ionics178.33 (2008): 1740-1745.

24. Uemiya, Shigeyuki, et al. "Steam reforming of methane in a hydrogen-permeable membrane reactor." Applied catalysis 67.1 (1990): 223-230.

25. Hamakawa, S., Ti Hibino, and H. Iwahara. "Electrochemical Hydrogen Permeation in a Proton-Hole Mixed Conductor and Its Application to a Membrane Reactor." Journal of the Electrochemical Society 141.7 (1994): 1720-1725.

26. Hamakawa, Satoshi, et al. "Synthesis and hydrogen permeation properties of membranes based on dense SrCe 0.95 Yb 0.05 O 3− α thin films." Solid State Ionics 148.1 (2002): 71-81.

27. Li, Jianlin, Heesung Yoon, and Eric D. Wachsman. "Carbon dioxide reforming of methane in a SrCe 0.7 Zr 0.2 Eu 0.1 O 3− δ proton conducting membrane reactor." International Journal of Hydrogen Energy 37.24 (2012): 19125-19132.

28. Uchida, H., et al. "Formation of protons in SrCeO 3-based proton conducting oxides. Part II. Evaluation of proton concentration and mobility in Yb-doped SrCeO 3." Solid State Ionics 36.1 (1989): 89-95.

29. Yajima, T., et al. "Protonic conduction in SrZrO 3-based oxides." Solid State Ionics 51.1 (1992): 101-107.

30. Mather, Glenn C., and M. Saiful Islam. "Defect and dopant properties of the SrCeO3-based proton conductor." Chemistry of materials 17.7 (2005): 1736-1744.

31. Kolodiazhnyi, T., and A. Petric. "The applicability of Sr-deficient n-type SrTiO3 for SOFC anodes." Journal of electroceramics 15.1 (2005): 5-11.

32. Primdahl, S., et al. "Sr-doped LaCrO3 anode for solid oxide fuel cells."Journal of the Electrochemical Society 148.1 (2001): A74-A81.

33. Magrasó, Anna, et al. "Structure, chemical stability and mixed proton–electron conductivity in BaZr 0.9− x Pr x Gd 0.1 O 3− δ." Journal of Power Sources 196.22 (2011): 9141-9147.

34. Barsoukov, Evgenij, and J. Ross Macdonald, eds. *Impedance spectroscopy: theory, experiment, and applications*. John Wiley & Sons, 2005.

35. Oh, Tak-keun, Heesung Yoon, and E. D. Wachsman. "Effect of Eu dopant concentration in SrCe 1− x Eu x O 3− δ on ambipolar conductivity." Solid State Ionics 180.23 (2009): 1233-1239.

36. Guan, J., et al. "Transport properties of BaCe 0.95 Y 0.05 O 3− α mixed conductors for hydrogen separation." Solid State Ionics 100.1 (1997): 45-52.

37. Yoon, Heesung, et al. "Fabrication of Thin-Film SrCe0. 9Eu0. 1O3− δ Hydrogen Separation Membranes on Ni–SrCeO3 Porous Tubular Supports."*Journal of the American Ceramic Society* 92.8 (2009): 1849-1852.

38. Li, Jianlin, et al. "High temperature SrCe 0.9 Eu 0.1 O 3− δ proton conducting membrane reactor for H 2 production using the water–gas shift reaction."*Applied Catalysis B: Environmental* 92.3 (2009): 234-239.

39. Ahmed, I. I., N. Nipattummakul, and A. K. Gupta. "Characteristics of syngas from co-gasification of polyethylene and woodchips." *Applied energy* 88.1 (2011): 165-174.

40. Li, Jianlin, Heesung Yoon, and E. D. Wachsman. "Hydrogen permeation through thin supported SrCe 0.7 Zr 0.2 Eu 0.1 O 3− δ membranes; dependence of flux on defect equilibria and operating conditions." *Journal of Membrane Science* 381.1 (2011): 126-131.

41. Oh, Takkeun, et al. "Hydrogen permeation through thin supported SrZr 0.2 Ce 0.8− x Eu x O 3− δ membranes." *Journal of Membrane Science* 345.1 (2009): 1-4.

42. Li, Jianlin, et al. "SrCe 0.7 Zr 0.2 Eu 0.1 O 3-based hydrogen transport water gas shift reactor." *International Journal of Hydrogen Energy* 37.21 (2012): 16006-16012.

43. Marnellos, George, et al. "The use of proton conducting solid electrolytes for improved performance of hydro-and dehydrogenation reactors." *Solid state ionics* 97.1 (1997): 375-383.

44. Li, Jianlin, Heesung Yoon, and Eric D. Wachsman. "Carbon dioxide reforming of methane in a SrCe 0.7 Zr 0.2 Eu 0.1 O 3− δ proton conducting membrane reactor." *International Journal of Hydrogen Energy* 37.24 (2012): 19125-19132.

45. Rohland, B., et al. "Electrochemical hydrogen compressor." *Electrochimica acta* 43.24 (1998): 3841-3846.

46. Grigoriev, S. A., et al. "Description and characterization of an electrochemical hydrogen compressor/concentrator based on solid polymer electrolyte technology." *International Journal of Hydrogen Energy* 36.6 (2011): 4148-4155.

47. Morozov, A. V., et al. "Hydrogen electro-transport in the solid polymer electrolyte cell." *Russ J Phys Chem A* 64 (1990): 3075-3080.

48. Sekiguchi, N., K. Himi, and M. Kadosaki. "Toyama Industrial Technology Center Research Report." *No* 16 (2002): 11-36.

49. Doucet, R., C. L. Gardner, and M. Ternan. "Separation of hydrogen from hydrogen/ethylene mixtures using PEM fuel cell technology." *International Journal of Hydrogen Energy* 34.2 (2009): 998-1007.

50. Ibeh, Blessing, Chris Gardner, and Marten Ternan. "Separation of hydrogen from a hydrogen/methane mixture using a PEM fuel cell." *International journal of hydrogen energy* 32.7 (2007): 908-914.

51. Onda, Kazuo, et al. "Treatment of low concentration hydrogen by electrochemical pump or proton exchange membrane fuel cell." *Journal of Power Sources* 188.1 (2009): 1-7.

52. Gardner, C. L., and M. Ternan. "Electrochemical separation of hydrogen from reformate using PEM fuel cell technology." *Journal of Power Sources* 171.2 (2007): 835-841.

53. Eberle, Klaus, et al. "Device and method for combined purification and compression of hydrogen containing CO and the use thereof in fuel cell assemblies." U.S. Patent No. 6,361,896. 26 Mar. 2002.

54. Ströbel, R., et al. "The compression of hydrogen in an electrochemical cell based on a PE fuel cell design." *Journal of power sources* 105.2 (2002): 208-215.

55. Eguchi, Taku, Kaoru Fukuda, and Makoto Tsuji. "Polymer electrolyte fuel cell." U.S. Patent No. 7,687,187. 30 Mar. 2010.

56. Koschany, Arthur, Christian Lucas, and Thomas Schwesinger. "Gas diffusion electrode for polymer electrolyte membrane fuel cells." U.S. Patent No. 5,998,057. 7 Dec. 1999.

57. Frost, Jonathan C., et al. "Manufacture of electrodes." U.S. Patent No. 5,871,860. 16 Feb. 1999.

58. Aoyama, Yuko, et al. "Solid polymer type fuel cell and method for manufacturing the same." U.S. Patent No. 5,474,857. 12 Dec. 1995.

59. Eda, Nobuo, et al. "Miniaturized fuel cell assembly." U.S. Patent No. 6,057,051. 2 May 2000.